HAL
open science

Descriptive and Explanatory Tools for Human Movement and State Estimation in Humanoid Robotics

François Bailly

To cite this version:

François Bailly. Descriptive and Explanatory Tools for Human Movement and State Estimation in Humanoid Robotics. Automatic. Université Toulouse 3 Paul Sabatier (UT3 Paul Sabatier), 2018. English. NNT : . tel-01927768v1

HAL Id: tel-01927768

https://laas.hal.science/tel-01927768v1

Submitted on 20 Nov 2018 (v1), last revised 7 Oct 2019 (v3)

HAL is a multi-disciplinary open access archive for the deposit and dissemination of scientific research documents, whether they are published or not. The documents may come from teaching and research institutions in France or abroad, or from public or private research centers.

L'archive ouverte pluridisciplinaire **HAL**, est destinée au dépôt et à la diffusion de documents scientifiques de niveau recherche, publiés ou non, émanant des établissements d'enseignement et de recherche français ou étrangers, des laboratoires publics ou privés.

THÈSE

En vue de l'obtention du

DOCTORAT DE L'UNIVERSITÉ FÉDÉRALE TOULOUSE MIDI-PYRÉNÉES

Délivré par :
l'Université Toulouse 3 Paul Sabatier (UT3 Paul Sabatier)

Présentée et soutenue le *10 octobre 2018* **par :**

François BAILLY

Descriptive and Explanatory Tools for Human Movement and State Estimation in Humanoid Robotics

---

JURY

Laurence CHÈZE	Professeure des Universités	Rapporteur
Auke IJSPEERT	Professor	Rapporteur
Jean-Paul LAUMOND	Directeur de Recherche	Examinateur
Emmanuel GUIGON	Chargé de Recherche	Examinateur
Philippe SOUÈRES	Directeur de Recherche	Directeur de Thèse
Bruno WATIER	Maître de Conférence	Co-directeur de Thèse

École doctorale et spécialité :
EDSYS : Robotique 4200046
Unité de Recherche :
Laboratoire d'Analyse et d'Architecture des Systèmes, LAAS-CNRS
Directeur(s) de Thèse :
Philippe SOUÈRES et *Bruno WATIER*
Rapporteurs :
Laurence CHÈZE et *Auke IJSPEERT*

Remerciements

J'adresse ces remerciements à mes encadrants, Philippe Souères et Bruno Watier, pour m'avoir offert l'opportunité de travailler sur les différentes questions abordées dans ce document. En particulier, je suis reconnaissant à Bruno d'avoir motivé la partie biomécanique du travail présenté, contribuant à son aspect pluridisciplinaire qui m'est cher. Ensuite, je veux chaleureusement remercier Philippe pour avoir su, il y a trois ans, me proposer un projet de thèse original que nous avons affiné au cours de nombreux échanges passionnants. Ils ont aiguisé ma curiosité, ma rigueur et mon goût pour la recherche et ils constituent le terreau des résultats qui ont vu le jour lors de cette thèse.

Je tiens à remercier Laurence Chèze et Auke Ijspeert pour leurs relectures attentives et les rapports motivés qu'ils ont fournis sur ce document. Je remercie également tous les membres du jury d'avoir fait le déplacement pour assister à la présentation du travail de cette thèse.

Le travail présenté ici n'aurait jamais vu le jour sans le soutien scientifique, technique et humain de l'équipe GEPETTO. Je souhaite remercier chacun de ses membres, des temporaires aux permanents, collègues et amis, qui constituent un ensemble riche au sein duquel il est très agréable d'évoluer et d'échanger. Parmi eux, j'ai eu la chance de collaborer plus étroitement avec Galo Maldonado et Justin Carpentier, que je tiens à remercier pour le temps passé à travailler ensemble.

Finalement, je remercie ma famille et mes amis d'avoir fourni des avis extérieurs pertinents sur ce travail et d'enrichir mon quotidien de leur présence.

Contents

Glossary **1**

Preamble **3**

I Elements and methods in biomechanics and robotics **9**

1 Methods in biomechanics **13**

1.1 Introduction 14
1.2 Anatomical terminology 14
1.3 Anatomical coordinate systems in humans 15
1.4 Anthropometric tables 16
1.5 Capturing and processing motion 18
1.5.1 Generalities 18
1.5.2 Inside the Gepetto team 19
1.6 Computing the physics of the motion 20
1.6.1 Center of mass 20
1.6.2 Linear and angular momenta 21
1.6.3 About inverse kinematics and inverse dynamics 22
1.7 Limitations 23

2 Elements of robotics **27**

2.1 Introduction 28
2.2 Brief reminder of automatic control 28
2.3 State representation in polyarticulated mobile robotics 30
2.3.1 Kinematic modeling 30
2.3.2 Dynamic modeling 30
2.4 State observation in mobile robotics 31
2.4.1 Internal state observation 31
2.4.2 External state observation 32
2.5 The task function approach 32
2.6 Control strategies in polyarticulated robotics 33
2.6.1 Inverse kinematics control 33
2.6.2 Inverse dynamics control 34

II Descriptive and explanatory tools for human movement 37

3 A mechanical descriptor of human locomotion
***And its application to multi-contact walking in humanoids* 41**
3.1 Introduction . . . 41
3.1.1 Motivations . . . 41
3.1.2 Outline and contributions of the work . . . 42
3.2 Mathematical background . . . 44
3.3 Experimental identification of $d_{\mathbf{c}-\Delta}$ . . . 44
3.3.1 Participants . . . 45
3.3.2 Experimental protocol . . . 45
3.3.3 Data acquisition . . . 47
3.3.4 Statistics . . . 47
3.3.5 Experimental results . . . 48
3.3.6 Discussion . . . 49
3.3.7 Conclusion . . . 49
3.4 Humanoid robot trajectory generation . . . 50
3.4.1 General overview of the motion generation pipeline . . . 52
3.4.2 Centroidal optimal control formulation . . . 52
3.4.3 Simulation results . . . 53
3.4.4 Discussion . . . 53
3.5 Conclusion & perspectives . . . 54

4 On the coordination of highly dynamic human movements
***An extension of the Uncontrolled Manifold approach applied to precision jump in parkour* 57**
4.1 Notions of motor control . . . 58
4.1.1 Motor redundancy . . . 58
4.1.2 Hierarchies of motor tasks . . . 59
4.1.3 The Uncontrolled Manifold approach . . . 59
4.1.4 Contribution to the field . . . 61
4.2 Extending the uncontrolled manifold approach . . . 61
4.2.1 Mathematical formulation of the UCM approach . . . 61
4.2.2 Extending the UCM approach to dynamic tasks . . . 62
4.2.3 An application to linear and angular momenta derivative tasks 65
4.3 Application to Take-off and Landing Motions in Parkour . . . 65
4.3.1 Precision jump and landing in parkour . . . 66
4.3.2 Experimental materials and methods . . . 66
4.3.3 Hypothesized task functions . . . 68
4.4 Results . . . 70
4.4.1 Take-off . . . 70
4.4.2 Landing . . . 71
4.5 Discussion . . . 73
4.5.1 Landing . . . 74

4.6 Conclusion and Perspectives 75

III From centroidal state estimation in engineering to state observation in animals 79

5 State estimation for systems in contact
***Recursive estimation of the center of mass position and angular momentum variation of the human body* 85**
5.1 Introduction 85
5.1.1 State of the art 86
5.1.2 Contribution 86
5.2 Methods 87
5.2.1 Estimated variables coupling 87
5.2.2 Measurements 88
5.2.3 Multi-source estimation of the CoM position 88
5.2.4 Multi-source estimation of the angular momentum variation quantity 90
5.2.5 Recursive estimation of the CoM position and the angular momentum variation 92
5.3 Experimental validation of the estimation framework 93
5.3.1 Generation of ground truth and noisy measures in simulation 93
5.3.2 Application to human data 96
5.4 Discussion 98

6 State estimation for systems in contact
***Using Differential Dynamic Programming for optimal centroidal state estimation* 101**
6.1 Introduction 101
6.2 State of the system and motivations 102
6.3 System's state observation 103
6.4 Estimating the state 104
6.4.1 State transition and observation equations 104
6.4.2 Problem formulation 104
6.4.3 The DDP algorithm 108
6.5 Illustration 109
6.6 Perspectives 110

7 Should mobile robots have a head ?
***A rationale based on behavior, automatic control and signal processing* 115**
7.1 Introduction 116
7.2 The Head in animals 119
7.3 A Head for state observation in robotics 121

7.3.1 State space representation and control of a multi-joint mobile robot. 121
7.3.2 The observation problem. 122
7.3.3 Head morphology and exteroceptive sensors. 124
7.4 A Head for signal processing and cognition 124
7.4.1 Centralizing exteroceptive perception and its processing. . . . 124
7.4.2 Shortening of the brain-ESO transmission channel. 125
7.4.3 Stiffening the exteroceptive kinematics. 125
7.4.4 Head mobility for enhanced perception 125
7.5 The role of the head in locomotion and manipulation 126
7.5.1 The head at the front-end of the movement for locomotion. . 126
7.5.2 One Head for supervising manipulation 127
7.6 Conclusion 127

Conclusion and perspectives **131**

A Calculation details of the UCM extension applied to kinematic and dynamic task functions **135**

B Application of the UCM extension to the derivative of the centroidal momenta task functions **137**

Bibliography **139**

List of Figures

1 Vitruvian man, pen and ink with wash over metalpoint on paper, *Leonardo Da Vinci, circa 1490.* 2

2 Five deer heads in the Nave region of Lascaux cave that might represent a single deer at different stages of its motion [Azéma 2012]. Reproduction of a Paleolithic drawing in the Lascaux cave, Musée d'Aquitaine, France. This is one of the first known illustration of animals in motion, where artists seemed to have captured the notion of displacement that is an elementary component of motion. 4

1.1 Chronophotograph of a flying pelican. *Étienne-Jules Marey, 1882.* . 13

1.2 Anatomical posture, *from [Whittle 2007].* 15

1.3 Locations of anatomical landmarks selected by [McConville 1980, Young 1983] and orientations of coordinate systems attached to these landmarks. *From [Dumas 2007].* 16

1.4 Example of anthropometric table. *From [Dumas 2007].* 19

1.5 Volunteer participant equipped with infrared markers fixed onto anatomical landmarks. *Courtesy of G. Maldonado.* 20

1.6 (a). 3D plots of the CoMs of each segment (in dashed red) and of the global CoM (in blue) during a walking movement on horizontal ground. (b). Emphasis on the global CoM during the same motion. . 21

2.1 Technical parts representing the three cornerstones of robotics: perception, decision and action. Head of the humanoid robot HRP-2 at LAAS-CNRS carrying multiple sensors for multimodal perception *(left).* Motherboard that holds and allows communication between the central processing unit and the memory, and that provides connectors for other peripherals such as sensors and motors *(middle).* Brushless DC electric motor, the most prevalent example of actuator in mobile robotics *(right).* 27

2.2 Schematic modeling of an open-loop dynamic system. 29

3.1 Overview of the experimental setup during a recording session. A participant is asked to achieve a challenging locomotion task while using the handlebar to help himself. 43

3.2 Scheme of the experimental setup with the range of distances considered. The scenario is composed of four tilted and adjustable wooden blocks. Each wooden block is topped with an adherent layer to prevent subjects from slipping. 45

3.3 Illustration of the different measurement involved in the experiment. $\mathbf{f_{fp}}$ is the force recorded from the force platform, $\mathbf{f_h}$ is the force recorded from the handlebar, $\mathbf{m}$ is the global moment expressed at the center of the force platform. Δ is the central axis of the external contact wrench. The dashed curved line is the path of $\mathbf{c}$ in time. $d_{\mathbf{c}-\Delta}$ is highlighted in the magnified portion of the image. 46

3.4 Normalized walking cycle in condition A (walking on flat ground). A: $d_{\mathbf{c}-\Delta}$ in mm as mean ± std, for the 15 participants. B: Height (z component) of the right and left toe markers for one participant. . . 48

3.5 Snapshots of the 15-cm steps climbing motion with handrail by the HRP-2 robot in simulation. 50

3.6 Traces representing the distance $d_{\mathbf{c}-\Delta}$ in the two cases of study: with and without regularization of $d_{\mathbf{c}-\Delta}$. 51

3.7 Traces representing the control input (acceleration of the CoM and the angular momentum variations expressed at the CoM) that drives the centroidal dynamics in the two cases of study: with and without regularization of $d_{\mathbf{c}-\Delta}$. 51

3.8 Traces representing trajectories of the state of the centroidal dynamics in the two cases of study: with and without regularization of $d_{\mathbf{c}-\Delta}$. 51

4.1 The word parkour derives from the classic obstacle course method of military training proposed by Georges Hébert (*Parcours du Combattant* in French). Here are displayed the five steps of the jump from Hébert's *Méthode Naturelle*. 57

4.2 What does it take not to fall from this wobbly structure, while keeping bowls balanced on your head? At least, three tasks are executed in parallel: keeping the body balanced on the unstable setup, maintaining the balance of the stack of bowls by controlling the head, all this while modifying the body configuration to grab another bowl. *Craig Nagy, Wikimedia Commons, CC BY-SA 2.0.* . 60

4.3 Experimental setup and motion analysis for the parkour precision technique. (a) The highest and the lowest two skeletons illustrate the beginning and the end of the take-off and of the landing motion, respectively. (b) Vertical trajectory of the CoM during the whole motion. (c) Vertical reaction force profiles during the whole motion. *From [Maldonado 2018a].* 67

4.4 Mean (± confidence intervals) values of the indexes of task control (ITC) during the take-off motion for the LMD(y,z) and the AMD(y) task functions, at each selected phase (1, 40, 70 and 100%.) Below: corresponding snapshots of the reconstructed motion. *From [Maldonado 2018a].* 71

4.5 Mean (± confidence intervals) values of the indexes of task control (ITC) during the landing motion for the LMD(z), LMD(x,y) and the AMD(x,y,z) task functions, at each selected phase (4, 13, 20, 40 and 100%.) Below: corresponding snapshots of the reconstructed motion. *From [Maldonado 2018a].* 72

5.1 Illustration of the measurement apparatus. The several physical quantities involved in the estimation framework are displayed, as well as a simplified sketch of the estimation framework. 87
5.2 Schematic representation of the spectral accuracy of the different input signals involved in the estimation of $\mathbf{c}$ and $\dot{\mathcal{L}}_{\mathbf{c}}$. 91
5.3 Flow chart for the recursive complementary estimation framework. s is the Laplace variable. Dotted lines represent the update step of the algorithm. Complementary filtered components are summed up in order to output $\dot{\mathcal{L}}_{\mathbf{c}}^{\mathbf{est}}$ and $\mathbf{c}^{\mathbf{est}}$, estimates of $\dot{\mathcal{L}}_{\mathbf{c}}$ and $\mathbf{c}$ respectively. 92
5.4 Norm of the error integrated over the whole trajectory for the different estimates of $\mathbf{c}$ in simulation, as a function of estimation steps. 94
5.5 Different contributions to the estimates of $\mathbf{c}$ and $\dot{\mathcal{L}}_{\mathbf{c}}$ in simulation. First row: $\mathbf{c}^{\mathbf{force}}$ high-pass filtered, $\mathbf{c}^{\mathbf{mocap}}$ band-pass filtered. Second row: true $\mathbf{c}$, $\mathbf{c}^{\mathbf{mocap}}$, $\mathbf{c}^{\mathbf{axis}}$ low-pass filtered and $\mathbf{c}^{\mathbf{est}}$. Third row: Logarithm of the norm of the FFT of the error for the different estimates. Fourth row: $\dot{\mathcal{L}}_{\mathbf{c}}^{\mathbf{est}}$ and $\dot{\mathcal{L}}_{\mathbf{c}}$. 95
5.6 Different contributions to the estimates of $\mathbf{c}$ and $\dot{\mathcal{L}}_{\mathbf{c}}$ on human recorded data. First row: $\mathbf{c}^{\mathbf{force}}$ high-pass filtered, $\mathbf{c}^{\mathbf{mocap}}$ band-pass filtered and $\mathbf{c}^{\mathbf{axis}}$ low-pass filtered. Second row: $\mathbf{c}^{\mathbf{est}}$ and $\mathbf{c}^{\mathbf{mocap}}$. Third row: $\dot{\mathcal{L}}_{\mathbf{c}}^{\mathbf{est}}$. 97

6.1 (*Left*) Logarithm of the total cost to go as a function of iterations of the DDP. (*Right*) Logarithm of $\nabla_{\boldsymbol{\omega}_i} Q_i$ as a function of iterations of the DDP. 109
6.2 Three components of $\mathbf{c}$, $\mathbf{p}$ and $\dot{\mathbf{p}}$ 111
6.3 Three components of $\mathcal{L}_{\mathbf{c}}$ and $\dot{\mathcal{L}}_{\mathbf{c}}$ 112

7.1 *Kingfisher in the wind.* These pictures are extracted from a short video clip of the bird fishing. The kingfisher's head remains still, while its body, attached to a swaying blade of grass, moves and deforms in all directions. The red dot is fixed in the frame of the camera, showing the anchorage of the head with regard to an inertial frame, despite the external perturbation applied to the bird's body. . 116
7.2 Examples of anterior structures in different bilateral animals highlighting their heads, sensory and trophic systems. From left to right: Zygoptera, Sepiida, Felidae (*Panthera* lineage), Callitrichinae, Gekkota, Tetraodontidae, Culicidae, Casuarius. 117

7.3 Artist's impression of the fauna at the Ediacaran–Cambrian boundary. Different kinds of morphotypes are illustrated as well as their feeding behaviors. © Agathe Haevermans. 118
7.4 Three different multi-joint mobile robots at LAAS: the flying manipulator Aeroarm (left), the mobile manipulator Jido (center), and the humanoid robot Talos (right). The usual choices for their root frame placement are displayed. 121
7.5 Illustrations depicting the internal and external states of a simple polyarticulated robot. (a): Absolute parameterization of the system in the plane. (b): Between the three cases depicted, only the external state of the system is changed. (c): The external state is parametrized by fully positioning the first body. (d): The parameterization of the external state is distributed on the three bodies of the robot. 123

List of Tables

1.1 Definitions of anatomical landmarks of Fig. 1.3, from [McConville 1980]. 17

3.1 Distances between the central axis of the external contact wrench and **c**, and average locomotion speeds across conditions A, B, C, D and E. Data are expressed as mean ± SD. Superscript $\star$ (resp. †) stands for "Not significantly different from conditions C (resp. E)". . 46

4.1 ITC-based hierarchical organization of the task functions during the take-off motion. $*$ stands for AMD(y) ITC significantly different from LMD(y,z) ITC. 71

4.2 ITC pairwise comparisons using paired t-tests for the task factor during the landing phases. $p-$values are adjusted with the Bonferroni correction. 73

4.3 ITC pairwise comparisons using paired t-tests for the phase factor during the landing phases. $p-$values are adjusted with the Bonferroni correction. 73

4.4 ITC-based hierarchical organization of the task functions during the landing motion. $*$, † and ‡ stand for significantly different from LMD(x,y), AMD(x,y,z) and LMD(z), respectively. 73

Glossary

Δ	Central axis of the contact wrench
$\mathcal{L}_{\mathbf{c}}$	Angular momentum at the center of mass
$\mathbf{c}$	Center of mass
$\mathbf{p}$	Linear momentum
$d_{c-\Delta}$	Distance between the CoM and Δ
A-P	Antero-Posterior
AMD	Angular Momentum Derivative
CMOS	Complementary Metal Oxide Semiconductor
CNS	Central Nervous System
CoM	Center of Mass
CoP	Center of Pressure
DDP	Dynamic Differential Programming
DoF	Degree of Freedom
ECW	External Contact Wrench
EMG	Electromyography
ESO	Exteroceptive Sensory Organ
IMU	Inertial Measurement Unit
ITC	Index of Task Control
LMD	Linear Momentum Derivative
M-L	Medial-Lateral
MoCap	Motion Capture
SCS	Segment Coordinate System
STA	Soft Tissue Artifact
UCM	Uncontrolled Manifold
ZMP	Zero Moment Point

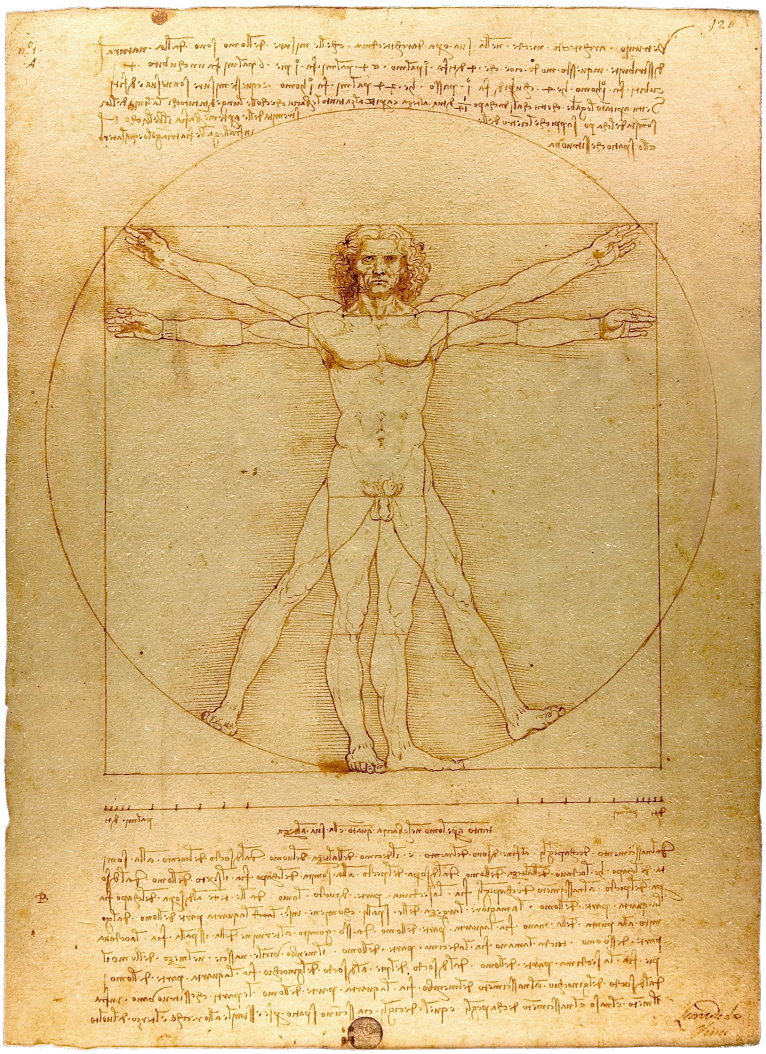

Figure 1: Vitruvian man, pen and ink with wash over metalpoint on paper, *Leonardo Da Vinci, circa 1490.*

Preamble

Measuring and portraying the human body is an old scientific and philosophical matter that goes back to Antiquity. One of the earliest and most remarkable example of the human will to describe its own body thanks to geometry appeared in Vitruve's treatise, *De Architectura*. Leonardo Da Vinci, later reproduced this description of ideal human proportions in his famous drawing, the *Vitruvian Man* (see Fig. 1). One of the artistic interests of this drawing lies in the mixture of mathematics and pictorial techniques from which it was derived. Beyond the anthropocentric beliefs that may have guided this work, several traits of human anatomy are aesthetically highlighted. First, its symmetry properties which considerably reduce the number of measurements required to describe the geometry of the whole body. Secondly, its stereotypical nature, which makes it possible to infer general rules of proportions from the inherent variability which characterizes biological species.[1]

Biomechanics and humanoid robotics are the continuation of this quest for introspection, except that their ambition is greater: not only measuring and portraying the properties of the body but also quantitatively describing its motion on the one hand, and on the other hand, utmost challenge, building machines capable of reproducing this motion! Motion has always been fascinating (see Fig. 2), probably because it contrasts with the stationarity of our environment.

What is motion?

In physics, the change in position of a body with respect to time and relatively to a reference point or observer is called a motion. As a direct consequence, the states of absolute motion and absolute rest do not hold because there exists no standard frame of reference in physics. In an inertial frame of reference however, on a sufficiently short time scale, most of our environment stays still (buildings, tree trunks, roads, etc.). Then, motion is the prerogative of bodies with non-zero net force acting upon them (a rolling stone, the foliage of a tree in the wind, an animal locomoting, etc.). Among these examples are two major families, that of undergone motion and that of active motion. Active motion occurs when the system is able to autonomously generate the forces that will enable its displacement, thus requiring actuating mechanisms. Animals, vehicles and robots are examples of systems which can actively generate interaction forces at their interface with the environment.

[1] These two features are further discussed in Chap. 1.

Figure 2: Five deer heads in the Nave region of Lascaux cave that might represent a single deer at different stages of its motion [Azéma 2012]. Reproduction of a Paleolithic drawing in the Lascaux cave, Musée d'Aquitaine, France. This is one of the first known illustration of animals in motion, where artists seemed to have captured the notion of displacement that is an elementary component of motion.

Characterizing the motion

The substantive subject of this thesis is the motion, and more particularly the bipedal locomotion of humans and humanoid robots. In order to characterize and understand locomotion in humans, its causes and consequences have to be investigated. Concerning the causes, what are the principles that govern the organization of motor orders in humans for elaborating a specific displacement strategy? The underlying motivation is to identify them for designing efficient control strategies in humanoid robotics. This can be done without direct access to the central nervous system, by measuring and studying the variance of kinematic and kinetic quantities. This is the topic of Chap. 4, where a mathematical framework is developed for studying the variance of kinetic quantities during jump in athletes. Indeed, the **control** operated in the motor space results in interactions in the physical space: joint angles, forces and torques which, for the observer, are the tangible consequences of motion, the **state** of the system.

As illustrated in Chap. 3, where a new mechanical descriptor of human locomotion is introduced, choosing the appropriate physical quantities to be computed for describing a physical phenomenon is always a pursuit of simplicity and expressiveness. One striking illustration of this statement in mechanics is the center of mass, the unique point which is the particle equivalent of a given object for computing its motion. Following this idea, researchers have introduced the notion of centroidal dynamics of a system in contact [Orin 2013], which combines the position of its center of mass with linear and angular momenta expressed at this point. As a result, the quantity of motion in translation and in rotation of the segments, as well as an idea of the posture of the body are condensed into nine variables. However,

one difficulty remains as the trajectory of the center of mass is not easy to measure directly. Therefore, once a state representation is chosen, comes the major problem of **observation**: how to process the measured data to retrieve the state?

Observing the motion

Observing the state of a system through an available set of measurements is an estimation problem. The difficulty of such a problem comes from the fact that the measurements carry noise which is not always separable from the informative data, and that the state of the system is not necessarily observable. The non-observability of the state can arise from a lack of appropriate sensors or from an improper placement of the sensors. To refocus on motion analysis, sensors in biomechanics and robotics provide kinematic and kinetic measurements, which provide useful information about the centroidal dynamics. To get rid of the noise, classical filtering techniques can be employed but they are likely to alter the signals. In Chap. 5, we present a recursive method, based on complementary filtering, to estimate the position of the center of mass and the angular momentum variation of the human body, two central quantities of human locomotion. Another idea to get rid of the measurements noise is to acknowledge the fact that it results in an unrealistic estimation of the motion dynamics. By exploiting the equations of motion, which dictate the temporal dynamics of the system, and by estimating a trajectory versus a single point, a so-called full-information estimation can be achieved. This work is presented in Chap. 6, where the dynamic differential programming algorithm is used to perform optimal centroidal state estimation for systems in contact.

Finally, observing their own motion is a necessary condition for animals to assess their position in time, and take actions accordingly. Therefore, it is relevant to investigate the means by which they have access to this motion information. We investigate this question in Chap. 7, where a multidisciplinary work is carried out, combining signal processing, automatic control and behavior. This study is focused on the similarities between the sensory apparatus of bilaterian animals and more specifically on the role played by their head for perception and state estimation.

Overview of the thesis

The content of this manuscript is divided into three parts. The first one gathers a selection of notions from biomechanics and robotics which are useful for introducing the contributions presented in the last two parts. The second part presents two original approaches devoted to the analysis of human motion. The first one is related to the mechanical description of human locomotion whereas the second one is about the coordination of dynamic movements by the central nervous system in humans. Finally, the third part is about state estimation in robotics and in living organisms. In this part, two technical contributions on the estimation of the centroidal state of systems in contact are followed by a multidisciplinary discussion about the role of the head for state estimation in animals.

Contributions

The work of this thesis resulted in the following contributions:

International Journals

- **François Bailly**, Justin Carpentier, Mehdi Benallegue, Philippe Souères and Bruno Watier. *Recursive estimation of the center of mass position and angular momentum variation of the human body.* Under review in Computer Methods in Biomechanics and Biomedical Engineering, 2018

- Galo Maldonado, **François Bailly** Bailly, Philippe Souères and Bruno Watier. *On the coordination of highly dynamic human movements: an extension of the Uncontrolled Manifold approach applied to precision jump in parkour.* Scientific reports, vol. 8, no. 1, page 12219, 2018

International Conferences with proceedings

- **François Bailly**, Vincent Bels, Bruno Watier and Philippe Souères. *Should robots have a head ?- A rationale based on behavior, automatic control and signal processing-.* In 7th International Conference on Biomimetic and Biohybrid Systems (Living Machines), 2018

- **François Bailly**, Justin Carpentier, Philippe Souères and Bruno Watier. *A mechanical descriptor of human locomotion and an application to multi-contact walking in humanoids.* In 7th IEEE International Conference on Biomedical Robotics and Biomechatronics (BioRob). IEEE, 2018

- Galo Maldonado, **François Bailly**, Philippe Souères and Bruno Watier. *Angular momentum regulation strategies for highly dynamic landing in Parkour.* Computer methods in biomechanics and biomedical engineering, vol. 20, no. sup1, pages 123–124, 2017

International Conferences without proceedings

- Galo Maldonado, **François Bailly**, Philippe Souères and Bruno Watier. *An interdisciplinary method based on performance variables to generate and analyze dynamic human motions.* In 8th World Congress of Biomechanics, Dublin, Ireland, 2018

- Galo Maldonado, **François Bailly**, Philippe Souères and Bruno Watier. *Identifying priority tasks during sport motions.* In 8th World Congress of Biomechanics, Dublin, Ireland, 2018

Part I

Elements and methods in biomechanics and robotics

This part of the thesis lays the technical and methodological foundations of the work presented in this manuscript which is related to both biomechanics and robotics. This part is divided in two chapters. In Chap. 1, the basics of human-related biomechanics are introduced. In Chap. 2, the main robotics tools that are used further in the manuscript are presented.

Chapter 1

Methods in biomechanics

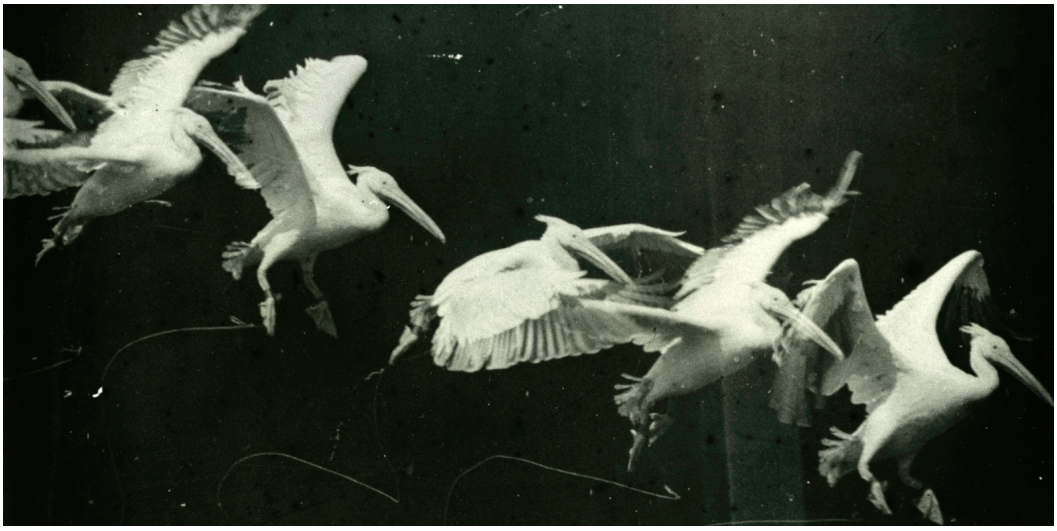

Figure 1.1: Chronophotograph of a flying pelican. *Étienne-Jules Marey, 1882.*

Contents

1.1 Introduction **14**

1.2 Anatomical terminology **14**

1.3 Anatomical coordinate systems in humans **15**

1.4 Anthropometric tables **16**

1.5 Capturing and processing motion **18**

1.5.1 Generalities 18

1.5.2 Inside the Gepetto team 19

1.6 Computing the physics of the motion **20**

1.6.1 Center of mass 20

1.6.2 Linear and angular momenta 21

1.6.3 About inverse kinematics and inverse dynamics 22

1.7 Limitations **23**

1.1 Introduction

Biomechanics is the study of the structure and function of the mechanics of biological systems, and more particularly, their movement. This grounding in mechanics implies that the notion of motion needs to be connected with the notion of forces. Indeed, as stated by Newton in 1687, the motion of a mass can be changed only if there exist forces applied to it. Thus, in order to obtain the data needed to describe and study motion in this framework, a threefold work has to be done. A kinematic part, which consists in recording the characteristics of the motion in space and time (range of motion, velocity of execution, accelerations, etc.), a so-called kinetic part, related to the recording of external forces and moments and, to connect these two parts, the knowledge of the mass distribution of the moving system is required. Historically, Étienne-Jules Marey (1830-1904) pioneered new technologies for motion analysis. Its chronophotographic gun was capable of recording up to 12 consecutive frames per second (See Fig. 1.1). In 1883, he designed the first dynamometric device in order to record vertical and horizontal force profiles during human locomotion. From that time on, the measure and estimation of kinematics, kinetics and mass data have been essential for the study of movement and posture, in particular in sport, ergonomics, rehabilitation and orthopedics.

Since the 80s, the development of Complementary Metal Oxide Semiconductor (CMOS) and infrared technologies has produced high-fidelity devices for measuring forces, on the one hand, and 3D kinematics on the other one. But before entering into technical details about human motion capture, let us recall in a first part some elementary pieces of anatomical terminology. Then, the full kinematic description of the human body, which is a polyarticulated system, requires to equip the body with a coordinate system that is presented in a second part. Thirdly, the notion of anthropometric tables, containing the mass data connecting kinematics and kinetics, is presented. Then, a deeper insight into the current technologies used in motion capture is provided. Finally, we discuss how to extract some key quantities from these data, that are used in both biomechanics and robotics.

1.2 Anatomical terminology

Standard anatomical terms of location have been developed to unambiguously describe the anatomy of animals, including humans. They are based on a set of planes and axes defined in relation to the body's standard position, commonly called "anatomical posture" (see Fig. 1.2). This anatomical posture helps avoid confusion in terminology when referring to the same organism in motion (i.e. in different postures). Six terms are used to describe the directions relative to the center of the body, that one can easily understand using the following examples:

- The navel is anterior
- The gluteus is posterior

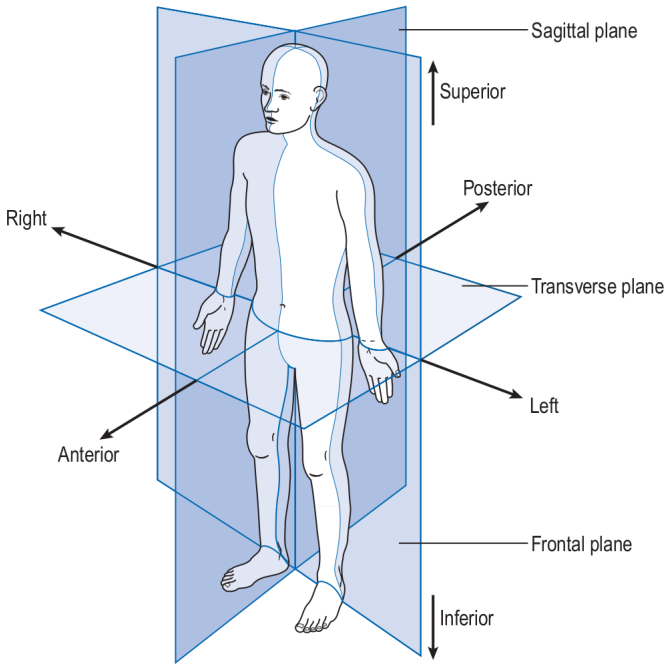

Figure 1.2: Anatomical posture, *from [Whittle 2007].*

- The head is superior
- The feet are lower
- Right and left are referenced with respect to the subject, not the observer

The movements of the various parts of the body are described by means of reference planes:

- The sagittal plane divides the body into the left and right parts
- The frontal plane divides the body into the anterior and posterior part
- The transverse plane divides the body into the superior and lower part

These three reference planes intersect at the Center of Mass (CoM) of the body.

1.3 Anatomical coordinate systems in humans

In biomechanics, the body is naturally divided into segments that correspond to limbs or groups of limbs. The tree structure of the human body (roboticists usually take the pelvis as the root) is well suited to a positioning of the parts from close to close. The bone structure naturally serves as the main reference frame attached to each limb (orientation, position) and the multiple joints with which humans are endowed are so many mechanical links to model. Each segment has to be positioned and to do so, it is attached with a Segment Coordinate System

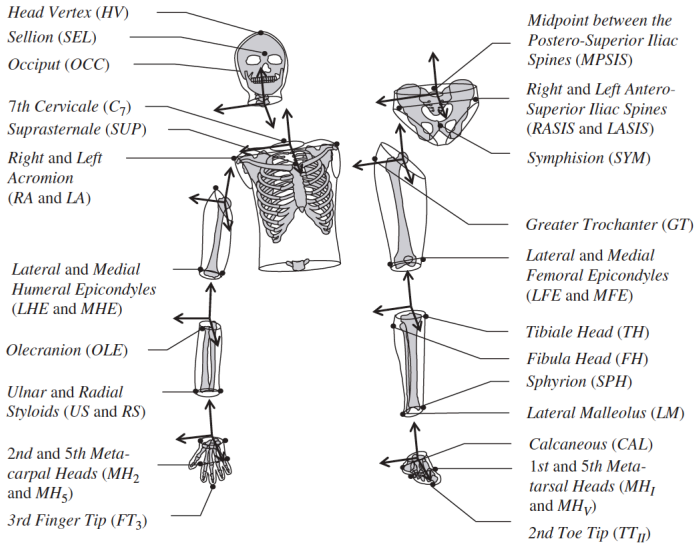

Figure 1.3: Locations of anatomical landmarks selected by [McConville 1980, Young 1983] and orientations of coordinate systems attached to these landmarks. *From [Dumas 2007].*

(SCS) whose orientation often reflects its main direction or a particular symmetry of the body at this location ([Wu 2002a, Wu 2005b]). Bone heads were chosen as appropriate anatomical landmarks in [McConville 1980] and [Young 1983] to retrieve the positioning of each SCS built from these landmarks (see illustration Fig. 1.3 and definition Tab. 1.1). Thanks to these coordinate systems, the position of the CoM of each segment, as well as its inertia matrix expressed in the SCS can be reconstructed using anthropometric tables (see Sec. 1.4). The advantages of choosing bone heads as anatomical landmarks are twofold: they can be found by palpation on a subject in order to equip it with infrared markers (see Sec. 1.5) and because of its rigidity, the bone structure limits undesirable movements of the markers commonly referred to as Soft Tissue Artifacts (STA) [Peters 2010] (see Sec. 1.7).

1.4 Anthropometric tables

The purpose of anthropometric tables is to establish the relationship between the human body size and its mass distribution properties. They rely on the fact that the body size and the moments of inertia are related to each other and that their correlations can be used to develop regression equations for predicting mass distribution characteristics. It is a non-invasive and fast method with regard to dissection and to 3D body scanning respectively.

In [McConville 1980], 31 adult males (mean age: 27.5 years, mean weight: 80.5kg, mean height: 1.77m) were studied versus 46 women (mean age: 31.2 years,

Anatomical landmark	Definition
Head Vertex (HV)	Top of head in the mid-sagittal plane
Sellion (SEL)	Greatest indentation of the nasal root depression in the mid-sagittal plane
Occiput (OCC)	Lowest point in the mid-sagittal plane of the occiput that can be palpated among the nuchal muscles
7th Cervicale (C7)	Superior tip of the spine of the 7th cervical vertebra
Suprasternale (SUP)	Lowest point in the notch in the upper edge of the breastbone
Right Acromion (RA)	Most lateral point on the lateral edge of the acromial process of scapula
Lateral Humeral Epicondyle (LHE)	Most lateral point on the lateral epicondyle of humerus
Medial Humeral Epicondyle (MHE)	Most medial point on the medial epicondyle of humerus
Olecranion (OLE)	Posterior point of olecranon
Ulnar Styloid (US)	Most distal point of ulna
Radial Styloid (RS)	Most distal point of radius
2nd Metacarpal Head (MH2)	Lateral prominent point on the lateral surface of second metacarpal
5th Metacarpal Head (MH5)	Medial prominent point on the medial surface of fifth metacarpal
3rd Finger Tip (FT3)	Tip of the third finger
Midpoint between the Postero-Superior Iliac Spines (MPSIS)	Midpoint between the most prominent points on the posterior superior spine of right and left ilium
Right Antero-Superior Iliac Spine (RASIS)	Most prominent point on the anterior superior spine of right ilium
Left Antero Superior Iliac Spine (LASIS)	Most prominent point on the anterior superior spine of left ilium
Symphision (SYM)	Lowest point on the superior border of the pubic symphisis
Greater Trochanter (GT)	Superior point on the greater trochanter
Lateral Femoral Epicondyle (LFE)	Most lateral point on the lateral epicondyle of femur
Medial Femoral Epicondyle (MFE)	Most medial point on the medial epicondyle of femur
Tibiale Head (TH)	Uppermost point on the medial superior border of tibia
Fibula Head (FH)	Superior point of the fibula
Sphyrion (SPH)	Most distal point on the medial side of tibia
Lateral Malleolus (LM)	Lateral bony protrusion of ankle
Calcaneous (CAL)	Posterior point of heel
1st Metatarsal Head (MHI)	Medial point on the head of first metatarsus
5th Metatarsal Head (MHV)	Lateral point on the head of fifth metatarsus
2nd Toe Tip (TTII)	Anterior point of second toe

Table 1.1: Definitions of anatomical landmarks of Fig. 1.3, from [McConville 1980].

mean weight: 63.9kg, mean height: 1.61m) in [Young 1983]. Both populations were selected to sample the weight/height distribution at best. Both studies took place on living subjects using the same stereo-photogrammetric technique based on the computation of segment volumes from the reconstruction of a 3D point cloud. This technique provided an accurate position of the global CoM, with an average error of 5.6% (relatively to the head vertex) compared to direct dissection measurements on 6 corpses in [McConville 1976]. The extensive body segment inertial parameters recorded in these studies were used by the authors to provide anthropometric tables. These tables were posteriorly adjusted in [Dumas 2007], where the inertial parameters were expressed directly in the conventional SCSs (versus anatomical axes) without restraining the position of the CoM and the orientation of the principal axes of inertia. In this work, authors used a segmentation into 15 segments: head and neck, torso, pelvis, arms, forearms, hands, thighs, legs and feet.

The state-of-the-art anthropometric tables which resulted from this study were used in the present thesis work, in the following way. Once the body segmentation is chosen, the locations of the centers of rotation of each joint are computed using anatomical landmark locations and regression equations. Then, the reference length of each segment is computed thanks to joints' centers of rotation. Knowing the SCS attached to the studied segment, a 3D-vector proportional to the reference length is computed from the origin of the SCS to the segment's CoM. Finally, a scaling factor for the mass of each segment defines how much it contributes to the computation of the whole-body CoM (see Sec. 1.6). All these proportional relationships are given by the anthropometric tables, according to the sex of the subject (see Fig. 1.4). Note they are only valid in the context of human morphologies similar to the one of the sampled population (see Sec. 1.7).

1.5 Capturing and processing motion

1.5.1 Generalities

The need for recording kinematic and kinetic data for a quantitative analysis of animal motion was previously introduced.

Kinematic data such as segments position and orientation, velocity, etc., are computed on the basis of anatomical landmarks, on which markers are fixed on the body. Their motion is tracked using cameras that record their 2D positions in the image plane. When more than one camera is available, and that their relative position is known (extrinsic parameters), the 3D coordinates of the landmarks can be computed. Computing the extrinsic parameters of such a Motion Capture (MoCap) system is called the calibration phase, and it is performed thanks to calibration objects whose geometry and dimensions are perfectly known. There exist active or passive markers, depending on the MoCap system. Active markers are equipped with infrared emitting diodes that are activated in a predefined sequence by a control unit, to correctly identify the markers. Passive markers are covered

Segment	Length definition	Origin of SCS	Gender	Length L (in mm)	Scaling factor for mass m (%)	Scaling factors for position of centre of mass			Scaling factors for tensor of inertia					
						X (%)	Y (%)	Z (%)	r_{xx} (%)	r_{yy} (%)	r_{zz} (%)	r_{xy} (%)	r_{xz} (%)	r_{yz} (%)
Head & Neck	*CJC* to *HV*	*CJC*	F	221	6.7	−7.0	59.7	0	32	27	34	6(i)	1	1(i)
			M	244	6.7	−6.2	55.5	0.1	31	25	33	9(i)	2(i)	3
Torso	*CJC* to *LJC*	*CJC*	F	429	30.4	−1.6	−43.6	−0.6	29	27	29	22	5	5(i)
			M	477	33.3	−3.6	−42.0	−0.2	27	25	28	18	2	4(i)
Arm	*SJC* to *EJC*	*SJC*	F	243	2.2	−7.3	−45.4	−2.8	33	17	33	3	5(i)	14
			M	271	2.4	1.7	−45.2	−2.6	31	14	32	6	5	2
Forearm	*EJC* to *WJC*	*EJC*	F	247	1.3	2.1	−41.1	1.9	26	14	25	10	4	13(i)
			M	283	1.7	1.0	−41.7	1.4	28	11	27	3	2	8(i)
Hand	*WJC* to midpoint between MH_2 and MH_5	*WJC*	F	71	0.5	7.7	−76.8	4.8	63	43	58	29	23	28(i)
			M	80	0.6	8.2	−83.9	7.4	61	38	56	22	15	20(i)
Pelvis	*LJC* to projection of *HJC* in sagittal plane	*LJC*	F	107	14.6	−0.9	−23.2	0.2	91	100	79	34(i)	1(i)	1(i)
			M	94	14.2	2.8	−28.0	−0.6	101	106	95	25(i)	12(i)	8(i)
Thigh	*HJC* to *KJC*	*HJC*	F	379	14.6	−7.7	−37.7	0.9	31	19	32	7	2(i)	7(i)
			M	432	12.3	−4.1	−42.9	3.3	29	15	30	7	2(i)	7(i)
Leg	*KJC* to *AJC*	*KJC*	F	388	4.5	−4.9	−40.4	3.1	28	10	28	2	1	6
			M	433	4.8	−4.8	−41.0	0.7	28	10	28	4(i)	2(i)	5
Foot	*AJC* to midpoint between MH_f and MH_V	*AJC*	F	165	1.0	27.0	−21.8	3.9	17	36	35	10(i)	6	4(i)
			M	183	1.2	38.2	−15.1	2.6	17	37	36	13	8(i)	0
Alternative length and origin														
Torso	C_7 to *SUP*	*SUP*	F	125	30.4	−41.1	−117.3	−1.9	98	93	98	76	16	19(i)
			M	139	33.3	−45.6	−112.1	−0.8	93	85	96	62	7	13(i)
Hand	*WJC* to FT_3	*WJC*	F	167	0.5	3.3	−32.7	2.1	27	18	25	12	10	12(i)
			M	189	0.6	3.5	−35.7	3.2	26	16	24	9	7	8(i)
Pelvis	Midpoint between *RASIS* to *LASIS*	Middle of *RASIS* and *LASIS*	F	238	14.6	−37.1	−5.0	0.1	41	45	36	15(i)	0	0
			M	224	14.2	−33.6	−14.9	−0.3	42	44	40	10(i)	5(i)	3(i)
Foot	*CAL* to TT_{II}	*CAL*	F	233	1.0	44.3	4.4	−2.5	12	25	25	7(i)	5	3(i)
			M	265	1.2	43.6	−2.5	−0.7	11	25	25	9	6(i)	0

Figure 1.4: Example of anthropometric table. *From [Dumas 2007].*

with reflective tape and are enlightened by infrared projectors to be made visible for infrared cameras (see Fig. 1.5). Coordinate data are calculated by the system with respect to a fixed reference frame in the laboratory. Data are then processed to obtain the desired kinematic variables.

Kinetic and kinematic data need to be synchronously recorded. To do so, force sensors are commonly connected to the MoCap system via a synchronization device. They often are 6-D sensors providing three orthogonal force components and three orthogonal moment components. They can be embedded into the floor or fixed on an external structure. When every contact of the body with its environment is measured with an appropriate force sensor, the external wrench of contact forces can be completely recorded. Then, one can perform a dynamic analysis of the body's motion and compute other variables such as internal joint torques and forces, joint power or joint mechanical energy [Winter 2009] (see Sec. 1.6). The forces produced by the muscles and transmitted through tendons, ligaments, and bones can also be estimated by modeling the musculoskeletal system [Delp 2007]. Moreover, activation patterns of the muscles can be measured through electromyography (EMG) sensors. Typically, these sensors are placed over the skin of the human body using surface EMGs.

1.5.2 Inside the Gepetto team

As part of its research at the frontier between robotics and biomechanics, the GEPETTO team at LAAS, works with the Centre de Ressources, d'Expertise et de Performance Sportives (CREPS) in Toulouse. As a result, researchers from both

institutions share a room which is equipped with a MoCap system and a set of force sensors (platforms, handles, etc.). The MoCap system is passive and made of 13 infrared T series VICON cameras, associated with a motion acquisition software (Nexus 1.8) that records markers' positions up to 400 Hz. The force sensors are two 6-axes AMTI force plates (90x180cm and 50x50cm) and two 6-axes SENSIX handles. The force sensors are synchronized to the MoCap system and recorded at a frequency of 2 kHz. All this equipment was used during this thesis work, to record and process human motions such as standard locomotion, locomotion on uneven terrain (see Chap. 3) or highly dynamic jumps in Parkour (see Chap. 4).

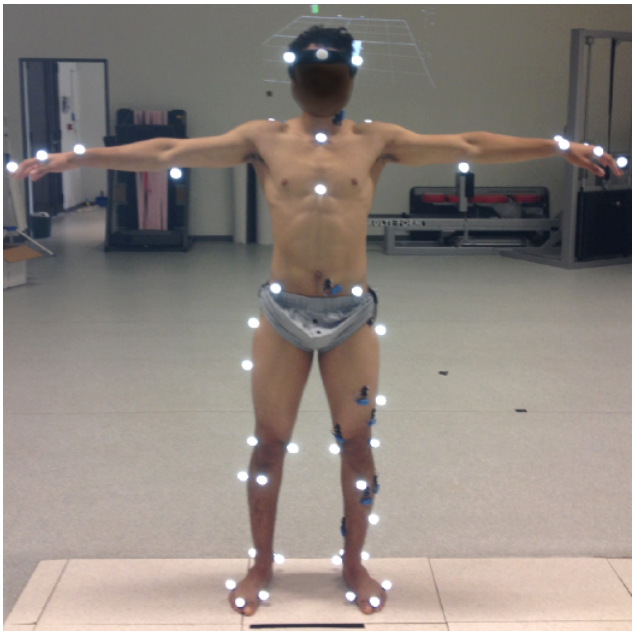

Figure 1.5: Volunteer participant equipped with infrared markers fixed onto anatomical landmarks. *Courtesy of G. Maldonado.*

1.6 Computing the physics of the motion

In this section, the different quantities that can be extracted from the kinematic and kinetic data are presented. They can be geometric (global CoM), kinematic (joints angles) or dynamic (linear and angular momenta, internal efforts).

1.6.1 Center of mass

Estimating the position of the CoM has been a scientific challenge for hundreds of years. Both whole body and local segments CoM are crucial to estimate because they are the points where gravitational and inertial forces apply. For instance, living subjects were used by [Weber 1836] to determine the CoM of a body by moving it on a platform until it balanced and then reversing the body and repeating the

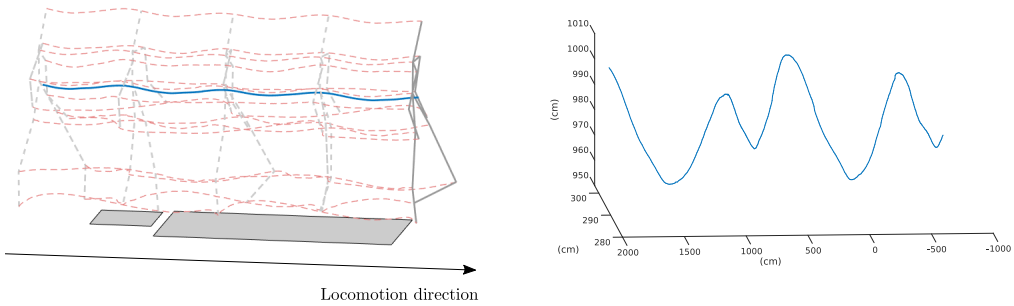

(a) (b)

Figure 1.6: (a). 3D plots of the CoMs of each segment (in dashed red) and of the global CoM (in blue) during a walking movement on horizontal ground. (b). Emphasis on the global CoM during the same motion.

procedure. The mean position between the two balance points was a more accurate approximation of the CoM than that obtained from earlier techniques. From that time on, several ingenious methods have been introduced but the most used today remains the one that uses kinematic data combined with anthropometric tables. [1]

By statistically knowing the mass contribution of each segment to the total mass of the body, one can reconstruct the global CoM of the subject. For instance, in Fig. 1.6a, the motion of a volunteer was recorded and the trajectories of each segment's CoM during standard walking on horizontal ground are displayed. In Fig. 1.6b, the trajectory of its global CoM is displayed, deduced from the weighted sum of each local CoM:

$$\mathbf{c} = \sum_{i=1}^{N} \alpha_i \mathbf{c_i}, \tag{1.1}$$

where $\mathbf{c}$ is the global CoM, $\mathbf{c_i}$ is the CoM of the ith segment, N is the total number of segments and ideally:

$$\alpha_i = \frac{m_i}{\sum_{i=1}^{N} m_i}.$$

In practice, α_i are given by anthropometric tables.

1.6.2 Linear and angular momenta

Among the central quantities that characterize the movement of a system, one cannot fail to mention the linear and angular momenta. Whereas the CoM is a

[1] For a more in-depth review of CoM estimation methods as well as for new methodologies introduced in this thesis work, see Chap. 5 and Chap. 6.

geometric quantity, the linear and angular momenta bring information about the forces that have been applied to the system. They complement the information of the CoM in the same way as kinetics enriches kinematic data. The linear momentum $\mathbf{p}$ of a polyarticulated system is:

$$\mathbf{p} = m\dot{\mathbf{c}}, \tag{1.2}$$

where m is the total mass of the system and $\dot{\mathbf{c}}$ is the velocity of its CoM. The angular momentum $\mathcal{L}_{\mathbf{c}}$ expressed at the CoM of the same system is computed as follows:

$$\mathcal{L}_{\mathbf{c}} = \sum_{i=1}^{N} (\mathbf{c_i} - \mathbf{c}) \times m_i \dot{\mathbf{c}}_i + \mathbf{I}_i \omega_i, \tag{1.3}$$

where $\mathbf{c_i}$, m_i, $\dot{\mathbf{c}}_i$ $\mathbf{I}_i$ and ω_i are the CoM, mass, CoM velocity, inertia matrix expressed at $\mathbf{c_i}$ and rotational velocity of the ith segment, respectively. The need for segmenting the polyarticulated system that is the human body into sub rigid bodies appears clearly in 1.3. This computation is also one of the reasons why the global CoM of the body alone is not enough for estimating the angular momentum from kinematic data. [2]

1.6.3 About inverse kinematics and inverse dynamics

Although the work presented in this thesis did not make a direct use of these methods, they deserve to be mentioned as they are widely used in biomechanics and constitute fundamental tools for the study of human movement. The following overview is neither detailed nor exhaustive, it is meant to give a taste of the currently most used methodologies.

In biomechanics, inverse kinematics computes the joint angles for a musculoskeletal model that best reproduce the motion of a subject. In Opensim for instance [Delp 2007], the input data are the 3D positions of reflective markers during the motion, and the best matching joint angles are estimated by solving a weighted least squares optimization problem with the goal of minimizing the marker errors. The marker error is defined as the distance between an experimental marker and the corresponding virtual marker. Each marker has an associated weighting value, specifying how confident the experimenter is about the chosen joint model or the quality of the experimental marker.

Inverse dynamics then uses joint angles, angular velocities, and angular accelerations of the model, together with the experimental ground reaction forces and moments, to retrieve internal forces and moments at each joint. This is done by recursively propagating reaction forces and applying Newton-Euler equations of motion through all the kinematic chain. Top-bottom and bottom-top approaches can be used for propagating the equations of motions, the last one

[2] Again, for an extensive review as well as new methodologies for estimating the angular momentum, see Chap. 5 and Chap. 6.

being preferentially used.

1.7 Limitations

The measure and the estimation of kinematics, kinetics and mass data are still active topics of research in biomechanics. This is partly due to the limitations of the different methodologies that researchers came up with, although they have proven to be sufficient in lots of applications. In the following, some of the limitations that biomechanical methods suffer from are non-exhaustively presented. They are part of the reasons which motivated the work of this thesis presented in Chaps. 5 and 6.

First, a word on anthropometric tables. They are one of the causes of the systematic and subject-specific errors that are made when analyzing human motion. To develop such tables, a sample of participants as to be taken from a specific population. This population has to be somewhat morphologically consistent, otherwise the regression equation would be inoperative. Even if some dedicated tables start to appear, their construction requires a considerable amount of work for sampling from the most diverse populations (obesity, malformations, pathologies, pregnant women, aging, children, etc.). As a consequence, most biomechanical studies are limited to subjects around 30 years old, without pathology. And even among this restricted population, the changes from a table to another impact the results of inverse dynamics [Rao 2006]. To remedy this problem, some recent studies have proposed personalized methods for determining the anthropometric parameters [Damavandi 2009, Hansen 2014].

Another systematic error that is committed comes from the STA that occurs during the recording of the motion. Usually, as a first approximation, the segments are modeled as rigid bodies. However, the motion of the soft masses around the bones is an obstacle to the proper localization of the musculo-skeletal system that impacts the results of CoM estimation and inverse dynamics [Peters 2010]. To overcome this major issue, studies have suggested to rigidify the set of markers [Cheze 1995] or to use redundant markers sets to reconstruct the frame linked to each segment while preferring areas of lower mobility [Monnet 2012].

The determination of the segments' centers of rotation is another source of errors that propagates to the kinematic and kinetic analyses because it determines the SCS. Among the methods that were introduced to reduce this error, the SCORE method (Symmetrical Center Of Rotation Estimation) is one of the most used today [Ehrig 2006]. It is an optimization algorithm that finds the most constant point relatively to both a parent segment and its child. Unlike former approaches, it does not require center of rotation to be fixed in an inertial frame and has proven to be more precise than state-of the-art methods [Monnet 2007].

Finally, another kind of random error which does not depend on the methodology comes from the different electric noises resulting in randomly fluctuating sensors measurements. They occur in the different sensors (force plates, MoCap), at different frequencies and they are inevitable but they can be handled

during the data processing, either by classical filtering (but this implies an inherent loss of information), or by more elaborate methods, such as the ones presented in Chap. 5 of this thesis.

Chapter 2

Elements of robotics

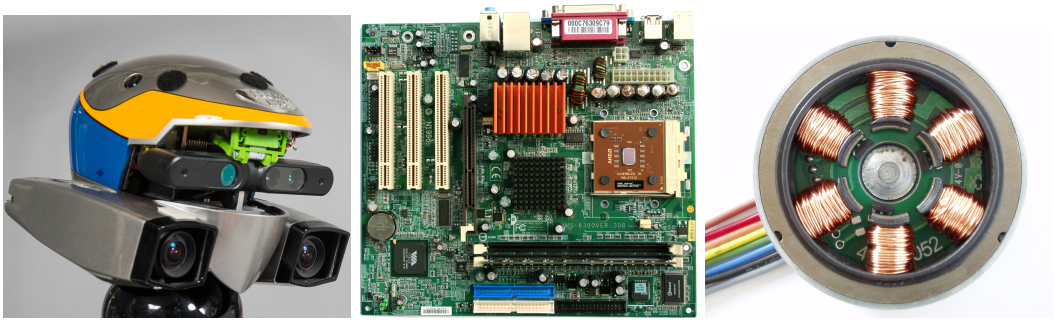

Figure 2.1: Technical parts representing the three cornerstones of robotics: perception, decision and action. Head of the humanoid robot HRP-2 at LAAS-CNRS carrying multiple sensors for multimodal perception *(left)*. Motherboard that holds and allows communication between the central processing unit and the memory, and that provides connectors for other peripherals such as sensors and motors *(middle)*. Brushless DC electric motor, the most prevalent example of actuator in mobile robotics *(right)*.

Contents

2.1 Introduction **28**

2.2 Brief reminder of automatic control **28**

2.3 State representation in polyarticulated mobile robotics . . **30**

2.3.1 Kinematic modeling 30

2.3.2 Dynamic modeling 30

2.4 State observation in mobile robotics **31**

2.4.1 Internal state observation 31

2.4.2 External state observation 32

2.5 The task function approach **32**

2.6 Control strategies in polyarticulated robotics **33**

2.6.1 Inverse kinematics control 33

2.6.2 Inverse dynamics control 34

2.1 Introduction

Robotics encompasses all the aspects of designing, building and controlling a robot, i.e., an autonomous machine capable of perception, decision and action in its environment (see Fig.2.1). Interestingly, the subject of this young science has long captivated both engineers and artists. Since the mid-20th century, several scientific and technical breakthroughs have allowed the appearance and miniaturization of integrated circuits, improving the performances of power electronics and computers, thus revolutionizing robotics among other disciplines. Indeed, even if the earliest records of autonomously operating machines can be traced back to ancient China (described in the Liezi text, 3rd century B.C.), compared to the definition of what a robot should be, the robotic designs developed before the end of the 20th century lacked the capabilities of perception and decision as they were only endowed with motor capabilities. Since then, many impressive robots have been designed, demonstrating more or less developed capabilities in the three basics functions they were endowed with [Hirose 2001, Park 2017].

Studying robotics is therefore a wide statement, at the crossroads of mechanics, electronics, mathematics and control. The robotic aspects of this thesis are focused on state estimation for the locomotion of biped robots. The purpose of the following chapter is to give a broad overview of the functions which are required to address robotic locomotion and to recall the main robotics tools that were used in this thesis. First, a quick reminder of automatic control is presented, providing the fundamental notions for describing and controlling dynamical systems (which robots are part of). Secondly, the robot needs to be endowed with a state representation to describe its trajectory as a function of time, according to the laws of mechanics. Thus, kinematic and dynamic modeling of polyarticulated mobile robots are introduced and discussed. The question of how to choose of the state representation will be developed in Chap. 7. Then, the question of state observation in mobile robotics is addressed, paving the way for the Part III of this thesis. Afterwards, the task function approach is explained, providing the mathematical tools that will be used in Chap. 4. Finally, inverse kinematics and inverse dynamics control are briefly introduced, demonstrating how the previously introduced notions of state and task are used for achieving locomotion with robots.

2.2 Brief reminder of automatic control

Automatic control is the science of modeling, analyzing and controlling dynamic systems. To this end, three fundamental notions are used to describe such systems at each time: their state $\mathbf{x}$, the commands $\mathbf{u}$ applied to them as inputs and the quantities that can be measured as outputs $\mathbf{y}$, as depicted in Fig. 2.2.

The state is a minimal dimension vector that fully characterizes the system's configuration. The choice of state representation is not unique, but its dimension is imposed by the nature of the system. The input control is also a vector of scalar variables used to drive the system. The output is the vector of measured quantities

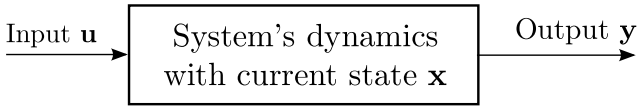

Figure 2.2: Schematic modeling of an open-loop dynamic system.

delivered by sensors. On this basis, the state representation of the system is defined by the two fundamental equations, Eqs. (2.1a) and (2.1b):

$$\dot{\mathbf{x}} = f(\mathbf{x}, \mathbf{u}), \tag{2.1a}$$

$$\mathbf{y} = g(\mathbf{x}, \mathbf{u}). \tag{2.1b}$$

Eq. (2.1a) is a first order differential equation that describes the dynamics of the system. It models how the state varies at each time depending on its current value and the applied input. Eq. (2.1b) is the output equation which models how the outputted measurements depend on the current state of the system and on the control.

On this basis, the **control problem** consists in finding a control law $\mathbf{u}(\mathbf{x}, t)$, which guarantees a desired behavior. Among the strategies that can be implemented, open-loop control laws make it possible to execute time-varying actuation patterns that are not modified according to the current state of the system (i.e., $\mathbf{u}$ does not depend on $\mathbf{x}$). Conversely, closed-loop or feedback control laws, provide control inputs that depend on the state of the system. Such strategies present several advantages against open-loop approaches because they are more robust to modeling errors, and they provide disturbance rejection and stability features among other things. For instance, let us examine stationary state feedback control laws (i.e., $\mathbf{u}$ does not depend on t). By injecting such a law $\mathbf{u}(\mathbf{x})$ into Eq. 2.1a, the closed loop equation that uniquely determines the local behavior of the robot according to its state becomes:

$$\dot{\mathbf{x}} = f(\mathbf{x}, \mathbf{u}(\mathbf{x})) = \tilde{f}(\mathbf{x}).$$

This equation uniquely determines the instantaneous behavior of the system based on its current state. When mathematically defined, the integration of this equation makes it possible to retrieve the state history. Different methods exist in automatic to elaborate such control laws, depending on the nature of the system and its desired behavior. In any case, in order to implement a closed loop control strategy, it is essential to be able to reconstruct the state of the system at any time. Estimating the state $\mathbf{x}$ from the measurements $\mathbf{y}$ and from the control $\mathbf{u}$ is the so-called **state observation problem** (see Sec. 2.4 and Part III). This problem is fundamental in automatic control and it is dual of the control problem. This general formalism applies to the description of any type of deterministic physical system modeled by differential equations, from electrical circuits to chemical processes or mechanical systems.

2.3 State representation in polyarticulated mobile robotics

In this section, classical choices for state representation in polyarticulated robotics are presented, depending on the level of modeling that is required by the use of the robot. Polyarticulated robots are composed of rigid parts connected with rotary joints, usually arranged in one or several chains. They can be of a wide variety of shapes, ranging from simple two-joint structures to systems with 30 or more interacting joints (e.g., industrial robots, humanoids, see Chap. 7 for illustrations). Their joints can be actuated by a variety of means, including electric or hydraulic actuators. The number of rotary joints defines the number of degrees of freedom (DoF) of the robot (if bolted in the ground), which, in turn, determines its aggregate positioning capabilities. For the reasons exposed in Sec. 2.2, to model, control and analyze these robots, their configuration has to be described thanks to an appropriate state representation. According to what is expected from these robots, the level of modeling can be adapted.

2.3.1 Kinematic modeling

Let us first consider the kinematics of polyarticulated mobile robots. In this case, the state representation $\mathbf{x}$ of these systems describes their internal geometric configuration (internal state, $\mathbf{q}$) and their position with respect to the environment (external state, $\mathbf{q_p}$), which is usually defined by the pose of a root frame attached to one specific body of the robot. Therefore, $\mathbf{x} = (\mathbf{q}_p, \mathbf{q})$. If the robot is composed of n 1-DoF joints in rotation, its state representation must include $n+6$ parameters. n of the parameters represent the joint angles $\mathbf{q} = (q_1, q_2, \cdots, q_n)$, the remaining 6 describe the pose (position and orientation) of the robot in space, $\mathbf{q_p} = (p_1, p_2, p_3, \theta_1, \theta_2, \theta_3)$. The presented robot possesses less motors than degrees of freedom resulting in the fact that its pose is not directly actuated. Such systems are called *underactuated*, and their pose can only be modified through forces/moments interactions with the environment. Kinematic modeling is limited to expressing the geometric constraints of the motion without taking into account the forces supplied by the actuators. This level of modeling is sometimes sufficient to describe robotic systems whose posture is stable and for which velocities are adapted with respect to the masses in motion. Under these hypotheses, a low-level control of the robot's motors makes it possible to consider that the control variables are the joint speeds, $\mathbf{u} = \dot{\mathbf{q}} = (\dot{q}_1, \dot{q}_2, \cdots, \dot{q}_n)$, showing that such systems are under actuated (n input variables to control $n+6$ parameters). Thus, kinematic robot models are generally velocity controlled.

2.3.2 Dynamic modeling

Some tasks require a dynamic modeling of the robot, kinematic modeling being insufficient to describe the causes of the motion of a mechanical system. In this case,

it is necessary to consider a dynamic model of the robot in adequacy with Newton's laws which express the link between the inertial effects of the moving bodies, the joint torques developed by the actuators, the contact forces and the derivative of the robot configuration parameters. The state representation of the same robot must then contain not only a representation of its geometric configuration, but also of its generalized velocities. The state vector of dimension $2(n+6)$ is therefore usually written as $\mathbf{x} = (\mathbf{q}_p, \dot{\mathbf{q}}_p, \mathbf{q}, \dot{\mathbf{q}})$. Once the dynamics is modeled, the control variables are the torques delivered by the actuators at each joint, $\mathbf{u} = \boldsymbol{\tau} = (\tau_1, \tau_2, \cdots, \tau_n)$. In this context, the equation (2.1a) of the dynamics of a polyarticulated robot is written as:

$$\dot{\mathbf{x}} = f(\mathbf{x}, \mathbf{u}) = M(\mathbf{x})^{-1}[S\boldsymbol{\tau} - B(\mathbf{x}) - G(\mathbf{x}) - \sum_k J_k \mathbf{f_k}] \tag{2.2}$$

where M is the inertia matrix of the robot which depends at each moment on its internal configuration, $B(\mathbf{x})$ is a non-linear term which includes the Coriolis and centrifugal forces, $G(\mathbf{x})$ represents the effects induced by gravity, S is a selection matrix aiming at connecting the motor torques to the actuated parts of the system, $\mathbf{f}_k$ is the wrench of external contact forces at the kth contact point and J_k is the Jacobian associated with the kinematic chain of this point (see [Saab 2013a] for more details).

2.4 State observation in mobile robotics

The concepts presented so far allow to identify the nature and number of variables needed to describe the robot state, to formulate its dynamic equation and to design its control. However, one fundamental problem has been left outstanding, that of state observation. As mentioned earlier, the state variables of a system generally cannot be directly measured and must be estimated from the output data of the sensors. This operation, the delicate question of state observation, requires to process the signals delivered by the sensors taking into account the different noises they suffer from, as well as the geometrical transformations between the physical quantity to measure and the sensor.

2.4.1 Internal state observation

The dynamic state of a poly-articulated mobile system includes its internal state, defined by the position and velocity of its joints $(\mathbf{q}, \dot{\mathbf{q}})$, and its external state, defined by the pose and velocity of its root frame $(\mathbf{q}_p, \dot{\mathbf{q}}_p)$ with respect to an inertial frame attached to the scene. As most robots have angular encoders at each joint, it is therefore possible, modulo the flexibility of the structure and the measurement noises of the encoders to have a good estimation of their internal state.

2.4.2 External state observation

To understand the stakes of estimating the external state, the case of robot navigation is illustrative. Before planning issues, one of the conditions for autonomous navigation is the robot's ability to determine its own pose and velocity in a frame of reference because it will condition its actions to reach a specific goal. One first naive solution could be to integrate the robot's dynamic equation to retrieve the state at each time from known actions and initial state, this is called odometry. In practice, this technique does not hold because the sensor measurement errors are integrated, accumulating the position errors over time, making it impossible to maintain a meaningful position estimate in long run. Another solution to this problem could be to endow mobile robots with Global Position System (GPS) devices. Unfortunately it is not sufficient for most applications because of the resolution of this technology (several meters) and because one might need more than only localizing the robot in the Earth's reference frame (building a local map for interacting with near objects for instance). MoCap systems provide a sufficient accuracy in indoor environment, but they lack portability, they need to be regularly calibrated and they are expensive. The problem of Simultaneously Localization And Mapping (SLAM), without relying on an external system (e.g. MoCap) is still an active field of research, its complexity coming from the fact that these two functions are strongly interrelated (*if an uncertain change is perceived in the environment, should I attribute it to my personal motion or to an uncertainty of my sensors? And vice versa...*).

Before dealing with processing measurement of sensors, it is necessary to choose the type of sensor and their location[1]. For localizing a robot, a wide variety of sensors has been developed and used. Generally, the best results are obtained when the measurements coming from different technologies are merged together to enrich the perception. Vision sensors (RGB, RGBD, infrared, etc.) are among the most used, inertial measurement units (IMUs) provide addition information about linear acceleration and angular velocities, magnetometers give the absolute orientation with regard to Earth's magnetic filed, sonar or lidar help for map building, etc.

2.5 The task function approach

The notion of task is central in robotics, as it defines the objective behavior of the robot for a given time horizon. The task to be performed may be expressed as a function, called **task function** $\mathbf{e}(\mathbf{x}, t)$ depending on the robot state and the time, whose regulation to zero during a time interval guarantees the achievement of the task [Nakamura 1991, Samson 1991]. Exponential decays control laws of the form $\dot{\mathbf{e}}(\mathbf{x}, t) = -\lambda_e \mathbf{e}(\mathbf{x}, t)$ are commonly used to make the task error converge quickly to a desired value. In order to simplify the presentation, let us focus on the case of stationary tasks that do not depend explicitly on time.

[1] In Chap. 7, the question of sensors placement for external state observation is further discussed.

Let $\mathcal{M}$ be the task space and let us denote by $\mathbf{e}(\mathbf{x}) \in \mathcal{M}$ a task function, where $\mathcal{M}$ is a $m-$dimensional manifold which can be locally identified to $\mathbb{R}^m$. $\mathbf{x} \in \mathcal{Q}$ is the state of the robot, where $\mathcal{Q}$ is a $n = k + 6$–dimensional manifold which can be locally identified to $\mathbb{R}^n$. One straight example is the pointing task defined by the task function $\mathbf{e}(\mathbf{x}) = \mathbf{hand}(\mathbf{x}) - \mathbf{hand}_{target}$, which describes the error between the current hand position $\mathbf{hand}(\mathbf{x})$, when the body is in the state $\mathbf{x}$ and the targeted hand position $\mathbf{hand}_{target}$. In order to express the variation of the task function with respect to the body configuration, the task Jacobian $J_e(\mathbf{x}) = \dfrac{d\mathbf{e}(\mathbf{x})}{d\mathbf{x}}$ is used. $J_e(\mathbf{x})$ is a m by n matrix whose entries are defined as:

$$\forall i \in 1, ..., m,\ \forall j \in 1, ..., n, \quad [J_e(\mathbf{x})]_{ij} = \frac{\partial e_i}{\partial x_j}. \tag{2.3}$$

The task Jacobian (Eq. (2.3)) is also the linear mapping between the time derivative of the task and the derivative of the state:

$$\dot{\mathbf{e}}(\mathbf{x}, \dot{\mathbf{x}}) = J_e(\mathbf{x})\dot{\mathbf{x}}, \tag{2.4}$$

which is convenient for control purposes.

This formalism will be used in Chap. 4 as a basis for the mathematical developments of the uncontrolled manifold approach in motor control.

2.6 Control strategies in polyarticulated robotics

Now that the main descriptive robotics tools used in this manuscript have been introduced, let us broadly present the control methods that use these tools.

2.6.1 Inverse kinematics control

For some geometric applications, it can be sufficient to control a kinematic model of the robot (see Sec. 2.3). To do so, the inverse kinematics problem consists in finding the kinematic state that corresponds to a desired kinematic task behavior.

The first order kinematics formulation consists in finding the joint velocities that produce the desired time derivative of some task function $\mathbf{e}$ using Eq. (2.4). A reference task behavior $\mathbf{e}^*$ is provided as input and the control problem can be expressed as the solution of the following unconstrained minimization problem:

$$\min_{\dot{\mathbf{x}}^*} \|\dot{\mathbf{e}}^* - J_e(\mathbf{x})\dot{\mathbf{x}}^*\|_2^2 .$$

The solution $\dot{\mathbf{x}}^*$ of this problem provides the optimal control law associated to the task function $\mathbf{e}$:

$$\dot{\mathbf{x}}^* = J_e^{\#}(\mathbf{x})\dot{\mathbf{e}}^*, \tag{2.5}$$

where $\{.\}^{\#}$ stands for the generalized inverse of a matrix.

The second order kinematics formulation exploits the time derivative of Eq. (2.4):

$$\ddot{\mathbf{e}}(\mathbf{x}, \dot{\mathbf{x}}, \ddot{\mathbf{x}}) = J_e(\mathbf{x})\ddot{\mathbf{x}} + \dot{J}_e(\mathbf{x}, \dot{\mathbf{x}})\dot{\mathbf{x}}. \tag{2.6}$$

The joints accelerations that produce at best the second order derivative of the desired task function can be obtained by solving the following optimization problem under the specific kinematic constraints of the robot:

$$\min_{\ddot{\mathbf{x}}^*} \left\| \ddot{\mathbf{e}}^* - J_e(\mathbf{x})\ddot{\mathbf{x}}^* - \dot{J}_e(\mathbf{x})\dot{\mathbf{x}} \right\|_2^2.$$

The optimal control law expressed in terms of the joint accelerations expresses:

$$\ddot{\mathbf{x}}^* = J_e^{\#}(\mathbf{x})(\ddot{\mathbf{e}}^* - \dot{J}_e(\mathbf{x})\dot{\mathbf{x}}) \tag{2.7}$$

2.6.2 Inverse dynamics control

When the desired task implies the control of torques and forces quantities, it becomes necessary to control a dynamic model of the robot (see Sec. 2.3). The dynamic control of a robot interacting with the environment has to take into account external forces. Thus, in addition to finding the joint torques that will produce a reference task acceleration behavior $\ddot{\mathbf{e}}^*$, the inverse dynamics control problem has to respect the dynamic model of the system and additional constraints that ensure the feasibility of the motion. Assuming unilateral contacts with the environment, this problem can be solved by setting a minimization problem under equality and inequality constraints as in [Saab 2011]:

$$\begin{aligned}
&\min_{\ddot{\mathbf{x}},\ \boldsymbol{\tau},\ \mathbf{f}} \|\ddot{\boldsymbol{e}}^* - \ddot{\mathbf{e}}(\mathbf{x}, \dot{\mathbf{x}}, \ddot{\mathbf{x}})\|_2^2 \\
&s.t. \quad M(\mathbf{x})\ddot{\mathbf{x}} + B(\mathbf{x}) - G(\mathbf{x}) - \sum_k J_k \mathbf{f_k} = S\boldsymbol{\tau} \\
&J_k\ddot{\mathbf{x}} + \dot{J}_k\dot{\mathbf{x}} = 0 \\
&\mathbf{f}_k^{\perp} \geq 0,
\end{aligned}$$

The first equality ensures that the solution respects the dynamical model of the system. The inequality constraint $\mathbf{f}_k^{\perp} \geq 0$ guarantees that the contact forces are unilateral, correctly oriented and that the contact is rigid. Other inequality constraints are usually added such as joint limits, torque limits or other tasks.

Part II

Descriptive and explanatory tools for human movement

Being able to isolate descriptive variables of biological phenomena is a powerful means of appreciating the relevance of scientific simulations, models, bio-inspired systems, etc. Once they are exhibited, one question comes naturally: do these descriptive variables actually correspond to concepts that are understood and employed by living organisms? One first element of answer lies in the physical quantities involved in the computation of such variables. Is the organism equipped with the appropriate sensory system so that it can sense and process this type of data? And if so, how to ensure that it exerts control over these variables? Among these fundamental questions lie two kinds of analyses, an observational one and an explanatory one.

This part of the thesis brings together the work done on the explanation and the observation of human movement. First, an observational work in which a mechanical descriptor of bipedal locomotion was derived, based on biomechanical methods (Chap. 3). Then, an explanatory work at the control level (Chap. 4), involving motor control methods to assess which tasks are actually controlled by the CNS in the execution of a particular movement.

Chapter 3

A mechanical descriptor of human locomotion

And its application to multi-contact walking in humanoids

*This chapter is almost literally taken from our article [**Bailly** 2018a].*

Contents

3.1 Introduction **41**
3.1.1 Motivations 41
3.1.2 Outline and contributions of the work 42
3.2 Mathematical background **44**
3.3 Experimental identification of $d_{\mathbf{c}-\Delta}$ **44**
3.3.1 Participants 45
3.3.2 Experimental protocol 45
3.3.3 Data acquisition 47
3.3.4 Statistics 47
3.3.5 Experimental results 48
3.3.6 Discussion 49
3.3.7 Conclusion 49
3.4 Humanoid robot trajectory generation **50**
3.4.1 General overview of the motion generation pipeline 52
3.4.2 Centroidal optimal control formulation 52
3.4.3 Simulation results 53
3.4.4 Discussion 53
3.5 Conclusion & perspectives **54**

3.1 Introduction

3.1.1 Motivations

Humanoid robotics and biomechanics share a common interest in the study of principles involved in human locomotion. Researchers from both fields have widely

used the Zero Moment Point (ZMP) to describe and evaluate several properties of locomotion on horizontal walkways. This particular point is the intersection between the ground and the axis along which the moment of contact forces under the feet is collinear to the normal of the ground [Sardain 2004].

In biomechanics, this criterion has been used to investigate gait control analysis, running mechanics, prosthesis, shoes design and fall detection [Fernie 1982, Collins 1993]. In these approaches, researchers have usually studied the ZMP trajectory which is considered to reflect information about neuromuscular control [Prieto 1996], during several tasks. In robotics, researchers have also controlled the ZMP to generate stable bipedal locomotion trajectories. For an extensive review of the computational foundations and applications of the ZMP, see [Kajita 2014].

However, this criterion suffers from limitations as it is only defined when contacts are coplanar. Thus, it becomes irrelevant when motions involve multiple non-coplanar contacts while this situation is common in everyday life (stairs climbing, door opening, elderly locomotion...) and increasingly used in humanoid robotics trajectory generation [Carpentier 2016b]. To overcome these limitations, several works have been done to expand the ZMP approach when locomotion is performed on uneven surfaces or when bipeds use multi-contact (cane, banister, etc.) [Sardain 2004, Harada 2003, Hirukawa 2006, Caron 2017].

3.1.2 Outline and contributions of the work

In this work, we propose to study human locomotion based on another mechanical approach related to the External Contact Wrench (ECW) (see Sec. 3.2). The key idea is to consider the central axis Δ of this wrench along which the moment of the contact forces applied to the body and the resultant of the contact forces are collinear. This axis is also the set of points where the overall moment induced by contact forces is minimal for the Euclidean norm (see Sec. 3.2), and can be computed even for generalized locomotion (uneven surfaces or multi contacts). According to Euler's second law, the overall moment applied to the CoM is equal to the variation of angular momentum at the CoM, and thus reflects the whole body gesticulation [Wieber 2006]. This result establishes a link between the relative position of the CoM with regard to the central axis Δ since, when they coincide, the variation of angular momentum at the CoM is minimal. Within the scope of bipedal locomotion, describing the relation between the need for angular momentum variations during certain phases and the quest for stability is a central question. In this context, the distance between the CoM and the central axis Δ, $d_{\mathbf{c}-\Delta}$, appears to be relevant for describing the motion of the body in contact as it is related to the whole body dynamics in addition to be computed from the contact forces (see Sec. 3.2).

After having theoretically demonstrated the consistency of our mechanical approach, the results of experimental tests in humans are presented (see Sec. 3.3). We hypothesized that the average $d_{\mathbf{c}-\Delta}$ should significantly vary as a function

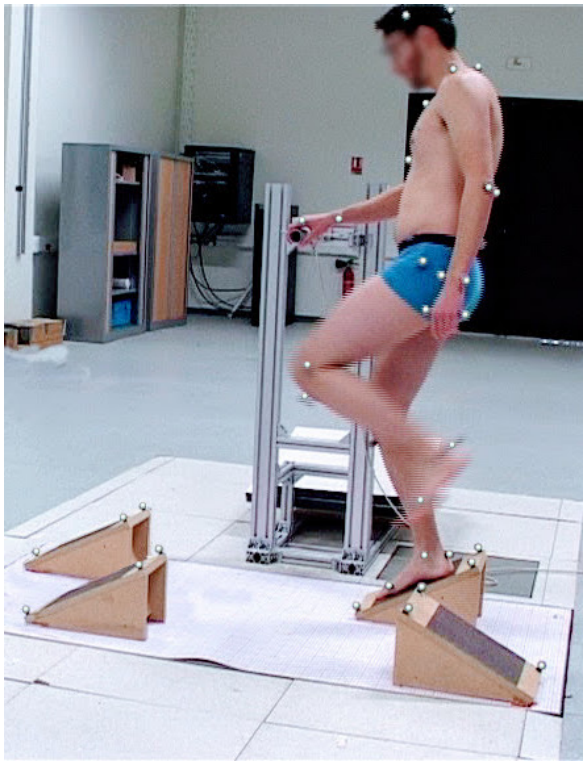

Figure 3.1: Overview of the experimental setup during a recording session. A participant is asked to achieve a challenging locomotion task while using the handlebar to help himself.

of motion phases and of increasingly demanding environmental constraints. This conjecture was corroborated by setting up walking experiments to study five different locomotion tasks involving non-coplanar foot contacts and contacts with hands. In addition, results demonstrate that, at the scale of the walking cycle, $d_{\mathbf{c}-\Delta}$ conveys information about the dynamical state of the body.

The interest of working with this mechanical quantity is finally illustrated in the context of multi-contact locomotion of humanoid robots (see Sec. 3.4). This is done by including $d_{\mathbf{c}-\Delta}$ in the cost function to be minimized within our trajectory generation framework [Carpentier 2016b]. The simulation results performed with the model of the HRP-2 robot show that minimizing this distance under contact constraints leads to dynamically consistent and whole-body feasible centroidal trajectories. These results also support the fact that our criterion is less conservative than simply minimizing the variation of angular momentum, as commonly done in humanoid trajectory optimization [Kajita 2014].

3.2 Mathematical background

In the sequel, we denote by $\mathbf{c}$ the CoM of the body, by Δ the central axis of the ECW and by $d_{\mathbf{c}-\Delta}$ the distance between $\mathbf{c}$ and Δ. Contact forces can be represented by a single 3 dimensional vector $\mathbf{f}$. At any point $\mathbf{a}$, $\mathbf{f}$ induces a moment $\mathbf{m_a}$. Therefore, $\mathbf{f}$ and $\mathbf{m_a}$ define a moment field that can be expressed at any point $\mathbf{b}$ as:

$$\mathbf{m_b} = \mathbf{m_a} + \mathbf{f} \times \mathbf{p_{ab}}, \tag{3.1}$$

where the vector $\mathbf{p_{ab}}$ expresses the position of $\mathbf{b}$ with respect to $\mathbf{a}$.

There exists one axis such that, at each point of this axis, the moment is parallel to $\mathbf{f}$ [Dimentberg 1968]. This axis, directed by $\mathbf{f}$, is the so-called central axis of the ECW (Δ). Without loss of generality, assuming that $\mathbf{a} \in \Delta$, and taking the Euclidean norm of (3.1) yields:

$$||\mathbf{m_b}||_2^2 = ||\mathbf{m_a}||_2^2 + ||\mathbf{f} \times \mathbf{p_{ab}}||_2^2 + 2\, \mathbf{m_a} \cdot (\mathbf{f} \times \mathbf{p_{ab}}), \tag{3.2}$$

with $2\, \mathbf{m_a} \cdot (\mathbf{f} \times \mathbf{p_{ab}}) = 0$ (hypothetically the moment about $\mathbf{a}$ is parallel to $\mathbf{f}$). This leads to the conclusion that, at any point $\mathbf{b}$, $||\mathbf{m_b}||_2^2 \geq ||\mathbf{m_a}||_2^2$, reaching the equality when $\mathbf{b}$ belongs to Δ, along which the moment of contact forces is minimal. Δ is computed as in [Shimba 1984a]:

$$\forall\ \mathbf{b} \text{ in space},\ \forall\ \mathbf{a} \in \Delta,\ \mathbf{p_{ba}} = \frac{\mathbf{f} \times \mathbf{m_b}}{||\mathbf{f}||^2} + \lambda \mathbf{f},\ \lambda \in \mathbb{R}. \tag{3.3}$$

When $\lambda = 0$, $\mathbf{a}$ is the projection of $\mathbf{b}$ onto Δ. In particular, $d_{\mathbf{c}-\Delta}$ is:

$$d_{\mathbf{c}-\Delta} = \frac{||\mathbf{f} \times \mathbf{m_c}||}{||\mathbf{f}||^2} = \frac{||\dot{\mathcal{L}}_\mathbf{c}|| \cdot |\sin(\theta)|}{||\mathbf{f}||}, \tag{3.4}$$

where $\dot{\mathcal{L}}_\mathbf{c} = \mathbf{m_c}$ is the derivative of the angular momentum expressed at $\mathbf{c}$ and θ is the angle between $\mathbf{f}$ and $\dot{\mathcal{L}}_\mathbf{c}$. Hence, controlling this distance amounts to control either the derivative of angular momentum at $\mathbf{c}$, or the angle between contact forces and the derivative of the angular momentum at $\mathbf{c}$, or the norm of contact forces. Furthermore, this distance contains information related to the centroidal dynamics of the body (see Sec. 3.4), which is ordinarily used in the control of humanoid robots. These observations will be discussed later on in Sec 3.3 and Sec. 3.4.

3.3 Experimental identification of $d_{\mathbf{c}-\Delta}$

The following section contains a description of the experimental protocol used to measure $d_{\mathbf{c}-\Delta}$ under increasingly challenging locomotion tasks for humans and a presentation of the outcomes of this experiment.

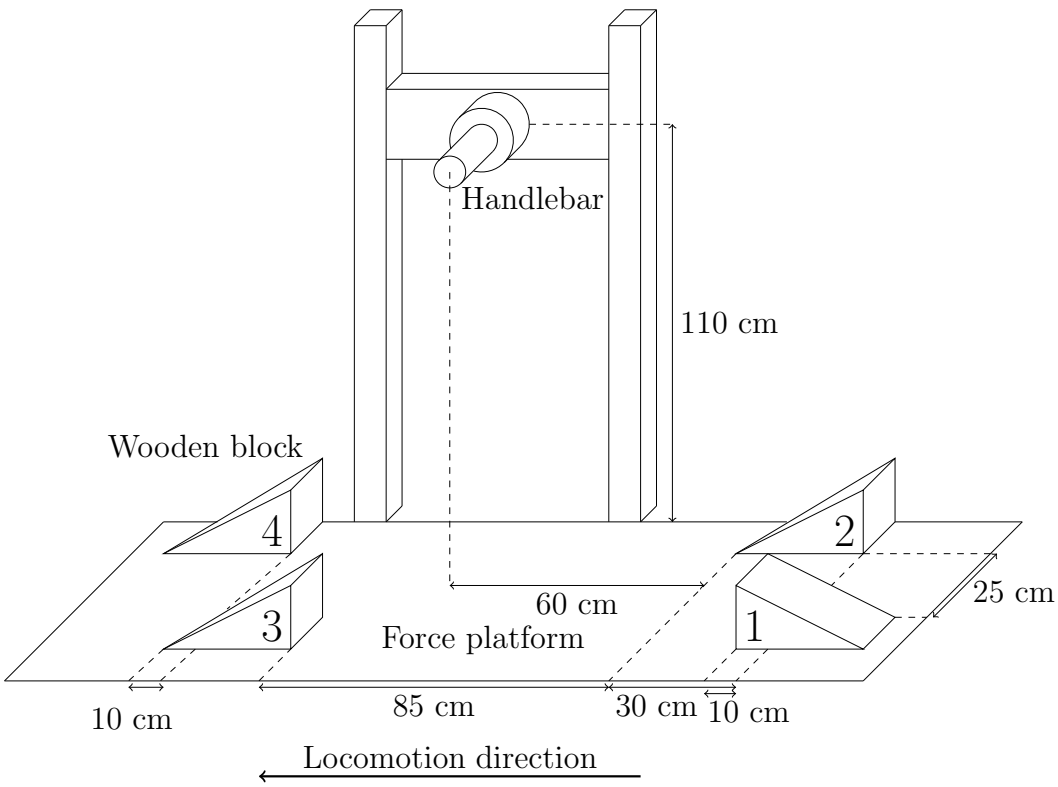

Figure 3.2: Scheme of the experimental setup with the range of distances considered. The scenario is composed of four tilted and adjustable wooden blocks. Each wooden block is topped with an adherent layer to prevent subjects from slipping.

3.3.1 Participants

Fifteen healthy male subjects (25.6 $\pm$ 5.8 y, height 1.77 $\pm$ .035 m, body mass 73 $\pm$ 8 kg) volunteered for this experiment. The participants had no prior or existing injury or neurological disorder affecting gait. Each participant was informed of the experimental procedure and signed an informed consent form prior to the study. The experiment was conducted in accordance with the declaration of Helsinki (rev. 2013) with formal approval of the ethics evaluation committee (IRB00003888, Opinion number 13-124) of the Institut National de la Santé Et de la Recherche Médicale, INSERM, Paris, France.

3.3.2 Experimental protocol

Each participant had to execute five barefoot walking tasks under different stepping conditions, involving an additional hand contact or not (see Fig. 1). They performed three trials for each experimental condition. For each trial, two preliminary steps were achieved before crossing the force platform. Time intervals of about 3 minutes were adjusted to prevent fatigue between repetitions. For conditions involving non-coplanar contacts to be achieved, a custom-made setup

Walking	Standard	On setup		On setup w handlebar	
Speed	Spontaneous	Spontaneous	Fast	Spontaneous	Fast
Condition	A	B	D	C	E
$d_{\mathbf{c}-\Delta}$ (mm)	55.1 ± 6.2	$(74.8 \pm 14.2)^{\star}$	150.9 ± 34.4	69.6 ± 13.5	123.8 ± 25.1
Average speed $(m.s^{-1})$	1.0 ± 0.15	$(0.71 \pm 0.24)^{\star}$	$(1.4 \pm 0.35)^{\dagger}$	0.73 ± 0.21	1.5 ± 0.32

Table 3.1: Distances between the central axis of the external contact wrench and **c**, and average locomotion speeds across conditions A, B, C, D and E. Data are expressed as mean ± SD. Superscript $\star$ (resp. †) stands for "Not significantly different from conditions C (resp. E)".

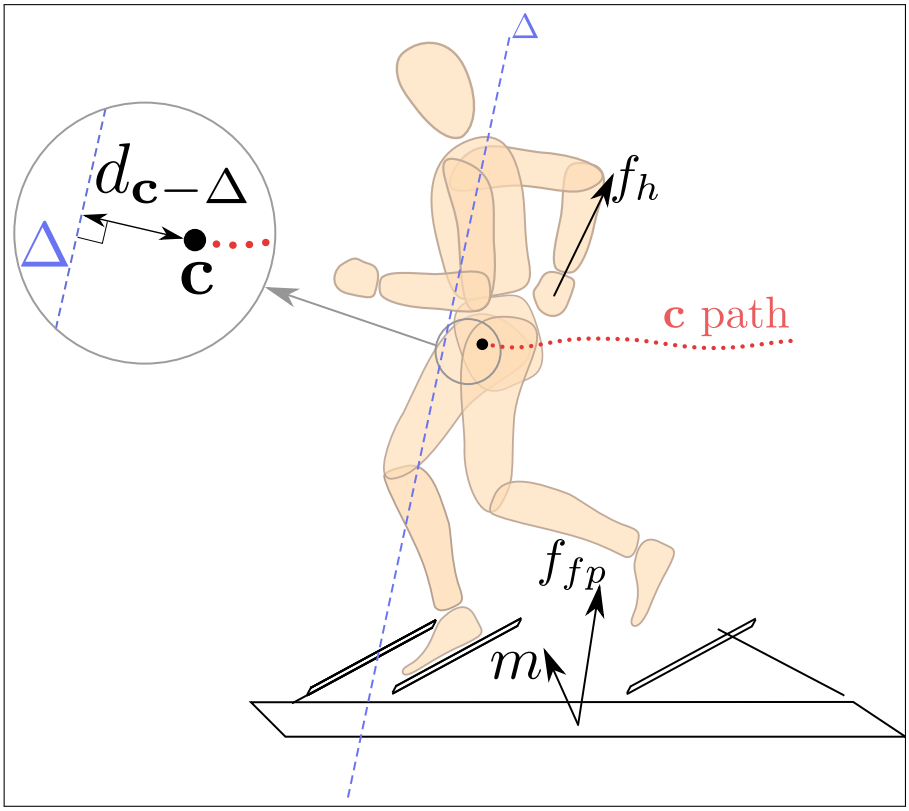

Figure 3.3: Illustration of the different measurement involved in the experiment. $\mathbf{f_{fp}}$ is the force recorded from the force platform, $\mathbf{f_h}$ is the force recorded from the handlebar, $\mathbf{m}$ is the global moment expressed at the center of the force platform. Δ is the central axis of the external contact wrench. The dashed curved line is the path of **c** in time. $d_{\mathbf{c}-\Delta}$ is highlighted in the magnified portion of the image.

was built which consisted of four 35°-sloped wooden blocks (i.e. three steps) fixed on the force platform embedded into the floor. A 6-cells force sensor, hereafter

called handlebar, was placed at 1.1 m high between blocks 2 and 3 (see details in Fig. 3.2). In the first condition (condition A), the volunteers were asked to achieve normal walking through the horizontal force platform, at spontaneous speed without any obstacle. After warming-up and getting familiarized with the experimental setup, participants were asked to walk on it (left foot first) for the four remaining conditions:

- B, at spontaneous speed, without handlebar
- C, at spontaneous speed, using the handlebar
- D, as fast as possible, without handlebar
- E, as fast as possible, using the handlebar

For conditions B, C, D and E, subjects were asked to cross the platform by walking only on the wooden blocks which were intentionally spaced in order to disturb locomotion (Tab. 3.1). Therefore, walking on the experimental setup was the first challenging parameter used to complicate the locomotion task.

In [Lamont 2007] and [Reid 2011], it has been shown that holding a fixed element during locomotion or, stair ascent and descent, slightly improves stability and balance confidence. Thus, the prohibition of the additional hand contact was the second parameter. The third parameter was speed locomotion: the experimental setup was designed in such a way that it was hard to cross it fast. The volunteers were asked to perform the tasks in a given order of what we refer to as increasing complexity (i.e. conditions A, C, B, E then D).

3.3.3 Data acquisition

The computation of $d_{\mathbf{c}-\Delta}$ required to record the ECW and the CoM position (see Eq. (3.4)). For the 3-dimensional kinematic analysis, 47 reflective markers were fixed on the subject's bone landmarks for local frame reconstruction according to [Wu 2005b]. Body segments masses and CoM positions were calculated in accordance with anthropometric tables [Dumas 2007]. Data were recorded by thirteen optoelectronic cameras sampled at 200Hz. The 6-dimensional ECW applied to the subject was recorded by the force platform (180×90 cm) and the handlebar, both sampled at 2kHz. The handlebar was localized thanks to 3D reflective markers. Data were synchronized using Nexus 1.7.1 and filtered using a 4th order, zero phase-shift, low-pass Butterworth with a 15Hz cutoff frequency. The acquisition procedure started when the right foot of the subject left the floor and stopped before the left foot reached the floor, in order to record full-contact motions (see Fig. 3.3).

3.3.4 Statistics

The average $d_{\mathbf{c}-\Delta}$ was computed for each subject and for the five experimental conditions. Before statistical tests, data normality was assessed using the Kolmogorov-Smirnov's test. Two separate one-way repeated measure ANOVAs

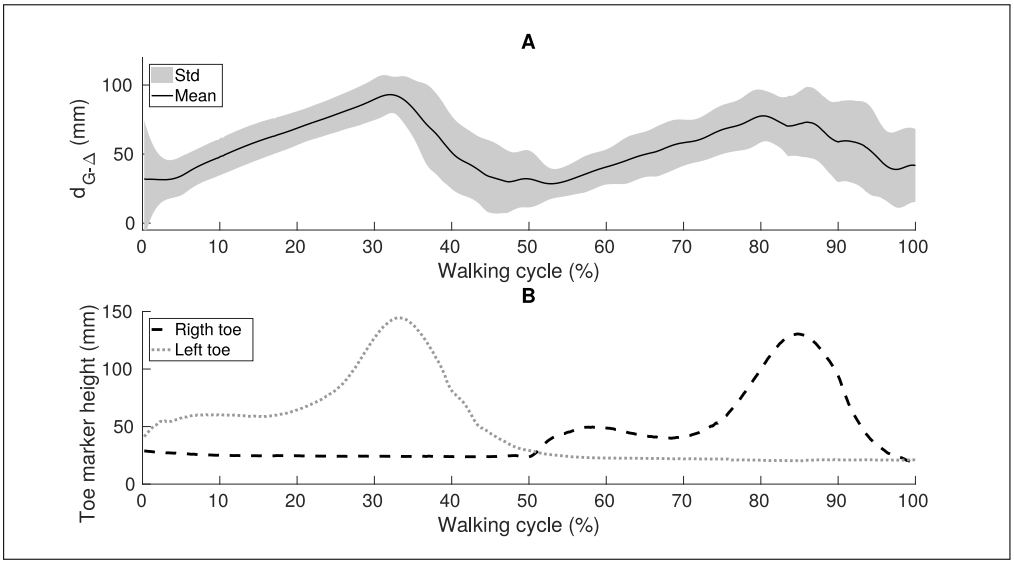

Figure 3.4: Normalized walking cycle in condition A (walking on flat ground). A: $d_{\mathbf{c}-\Delta}$ in mm as mean ± std, for the 15 participants. B: Height (z component) of the right and left toe markers for one participant.

were performed to compare the mean distance and the locomotion speed across conditions ($p < 0.001$) each followed by ten paired t-tests with the Bonferroni correction ($p < 0.05/10$) to assess the effect of each condition on $d_{\mathbf{c}-\Delta}$ and to verify if speed instructions significantly modified subjects' locomotion speed. The main hypothesis was accepted if the mean of $d_{\mathbf{c}-\Delta}$ significantly increased together with the complexity of the locomotion tasks: conditions A, C, B, E then D.

3.3.5 Experimental results

Fig. 3.4A shows $d_{\mathbf{c}-\Delta}$ (in average ± standard deviation) for the three trials of each subject, in condition A. Fig. 3.4B shows the height of one of the right and left toe markers for one participant, in condition A. One normalized walking cycle is displayed for both plots. Toe height profiles are used to identify the different phases of the walking cycle (single support, double support) and segment the time evolution of the distance displayed above (Fig. 3.4A). During double support phases, $d_{\mathbf{c}-\Delta}$ decreases, while it increases during right and left swing phases (from 30mm up to more than 100mm). Values of the average CoM velocity and $d_{\mathbf{c}-\Delta}$ are displayed in Tab. 3.1. The statistical analysis revealed that locomotion speed in conditions B and C was significantly slower than in conditions A, D and E (about twice), and it was significantly faster in conditions D and E than in condition A. These results show that the participants followed the speed instructions correctly. Paired t-tests revealed that $d_{\mathbf{c}-\Delta}$ in B tested against C could not be said to be significantly different (Tab. 3.1). The remaining data in Tab. 3.1 show that the mean distance significantly increased across the different conditions (ranging from

55.1mm to 150.9mm, by order of increasing distance : A,C-B,E then D).

3.3.6 Discussion

Because its depends on the whole body dynamics, the variation profile of $d_{\mathbf{c}-\Delta}$ at the scale of the walking cycle is representative of the rhythm of locomotion as it allows to retrieve double support and leg swing phases. In addition to this temporal analysis, the average analysis of $d_{G-\Delta}$ reveals that, compared to standard locomotion on level ground, asking the subject to walk on the experimental setup noticeably increased $d_{\mathbf{c}-\Delta}$ (condition A against B, C, D and E). Although one cannot conclude whether, at spontaneous speed, using the handlebar modified the distance $d_{\mathbf{c}-\Delta}$ or not, in this study, at high speed, when subjects were allowed to stabilize themselves using the handlebar (condition E), the distance significantly decreased in comparison with the corresponding condition at the same speed but without the handlebar (condition D). When participants were asked to cross the platform at high speed (conditions D and E), $d_{\mathbf{c}-\Delta}$ increased in comparison with the corresponding conditions at spontaneous speed (conditions B and C). In essence, looking into the three different parameters used to perturb the locomotion of the volunteers, $d_{\mathbf{c}-\Delta}$ increased with the complexity of the task. $d_{\mathbf{c}-\Delta}$ being directly related to $\dot{\mathcal{L}}_{\mathbf{c}}$, this general result suggests that increasingly challenging locomotion tasks might require either more variation of angular momentum or non-collinearity between $\dot{\mathcal{L}}_{\mathbf{c}}$ and $\mathbf{f}$. The first possibility makes sense from a mechanical point of view, as both increased velocity and gesticulations due to uneven terrain lead to heavier inertial effects and thus to a larger $\dot{\mathcal{L}}_{\mathbf{c}}$. For the second possibility to be filled, given that contact forces are mainly vertical in the context of bipedal locomotion, the components of $\dot{\mathcal{L}}_{\mathbf{c}}$ must be horizontal and correspond to tipping motions. This might be caused in particular by the inclination of the wooden blocks with regard to the gravity direction, and the whole-body resulting motions.

Finally, by revealing the instantaneous dynamic state of the body (double support, leg swings) or its average rotational behavior (gesticulation, tipping motions), $d_{\mathbf{c}-\Delta}$ characterizes the motion.

3.3.7 Conclusion

In this first part, a mechanical quantity for characterizing human motion was introduced. Both theoretically and experimentally, it was shown to carry relevant information about the dynamics of the body in contact. In particular, it was demonstrated that the average value of $d_{\mathbf{c}-\Delta}$ over a trajectory or its pattern during a walking cycle depends on the complexity and the phase of the locomotion task.

In biomechanics, this result is of particular interest, because, at the cost of estimating the CoM position, it provides a way of characterizing any whole-body motion in contact, even in situations where the classical ZMP would fail (non-coplanar, multi-contact). For instance, it could be used for comparing standard and instrumented walking (e.g., elderly, prosthesis, exoskeleton) on uneven terrains. In

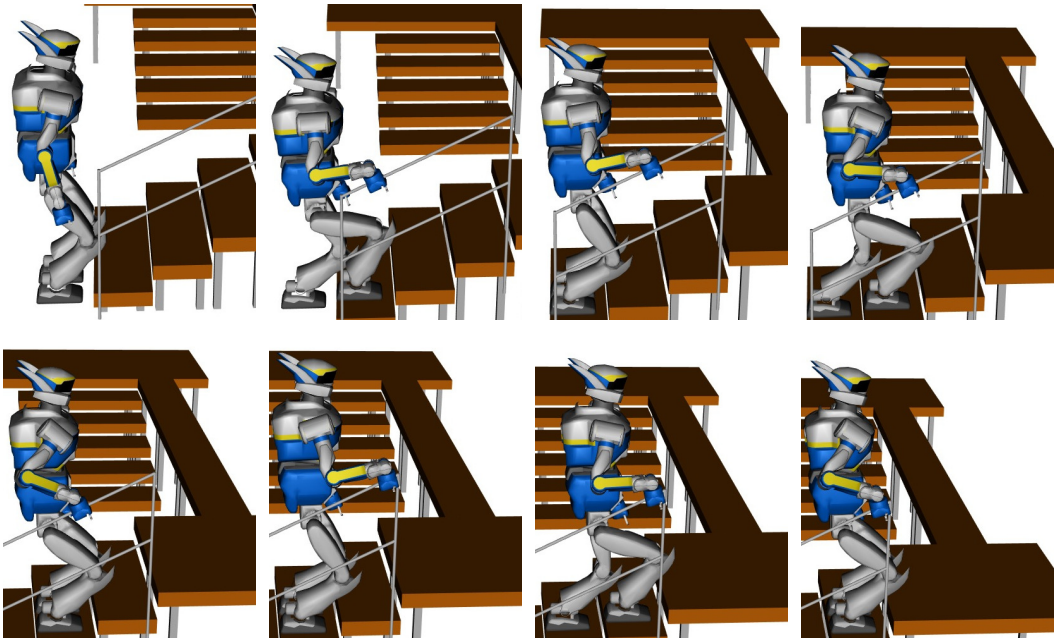

Figure 3.5: Snapshots of the 15-cm steps climbing motion with handrail by the HRP-2 robot in simulation.

addition, our proposal is quite different from the study of angular moment alone [Herr 2008a, Popovic 2004], since $d_{\mathbf{c}-\Delta}$ includes the coupling of the whole-body dynamics with contact forces. Therefore, the control of this quantity opens a larger space of strategies than those related to the control of the angular moment alone (see Eq. (3.4)). Finally, the dependence of $d_{\mathbf{c}-\Delta}$ on $\dot{\mathcal{L}}_{\mathbf{c}}$ and $\mathbf{f}$ supports that this value is plausibly controlled by the central nervous system (CNS) [Robert 2009, Yen 2009].

In humanoid robotics, the control of the angular momentum has been the topic of a number of recent research activities, such as gait control [Yun 2011] or balance assessments [Goswami 2004]. Although some work has been done to handle it for generating whole-body motions in simulation, when it comes to real motions, humanoid robotics approaches are mostly conservative (e.g., angular momentum forced to zero by the model [Kajita 2014], or minimized inside a cost function). Although the dynamic nature of human locomotion results in varying profiles of $d_{\mathbf{c}-\Delta}$, one can choose to minimize this quantity in order to implement a conservative whole-body behavior for the robot. This is illustrated in the next section, in which we propose to regulate $d_{\mathbf{c}-\Delta}$ as a cost function for a stair ascent task with the humanoid robot HRP-2.

3.4 Humanoid robot trajectory generation

In this section, we illustrate the minimization of $d_{\mathbf{c}-\Delta}$ in the context of multi-contact locomotion for the humanoid robot HRP-2. In order to highlight its relevance for real applications, we apply this control strategy on a stair climbing scenario

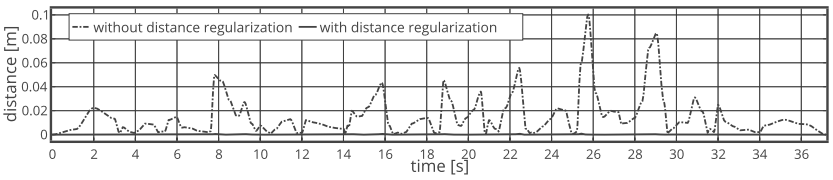

Figure 3.6: Traces representing the distance $d_{\mathbf{c}-\Delta}$ in the two cases of study: with and without regularization of $d_{\mathbf{c}-\Delta}$.

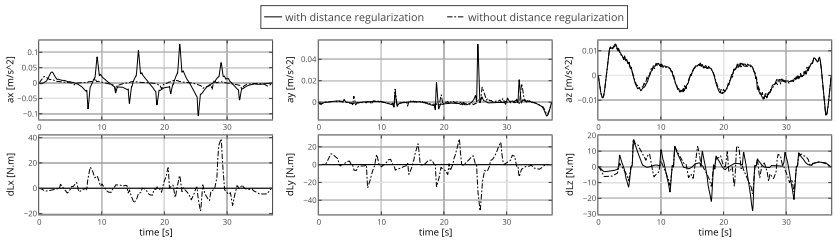

Figure 3.7: Traces representing the control input (acceleration of the CoM and the angular momentum variations expressed at the CoM) that drives the centroidal dynamics in the two cases of study: with and without regularization of $d_{\mathbf{c}-\Delta}$.

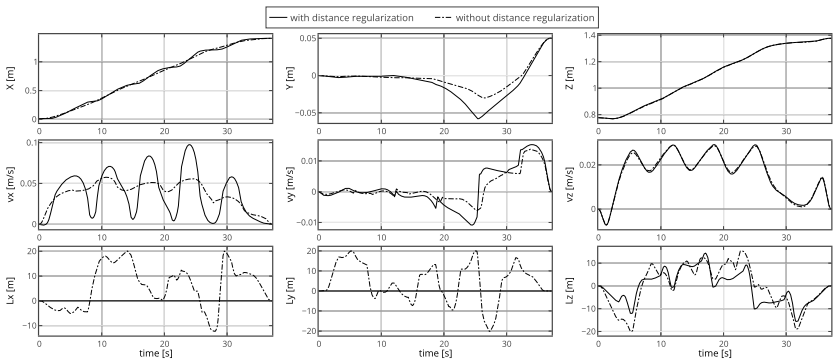

Figure 3.8: Traces representing trajectories of the state of the centroidal dynamics in the two cases of study: with and without regularization of $d_{\mathbf{c}-\Delta}$.

where the robot has to use the handrail for helping itself. After having shown the results of this simulation, we discuss why using $d_{\mathbf{c}-\Delta}$ differs from using the angular momentum alone, and how it could be applied to other scenarios.

3.4.1 General overview of the motion generation pipeline

The pipeline used is the same as the one originally introduced in [Carpentier 2016b] and extended in [Carpentier 2017a]. This formulation allows to compute a feasible trajectory (both kinematically and dynamically feasible) for the centroidal dynamics according to a sequence of contacts given as input. As a reminder, the centroidal dynamics is the dynamics of the whole-body system expressed at its CoM [Orin 2013], involving the CoM position together with the linear and angular momenta expressed at the CoM. From the sequence of contacts and the centroidal dynamics trajectory, we use an inverse dynamics solver [Saab 2013b] to compute the whole-body motion.

3.4.2 Centroidal optimal control formulation

The central piece of this pipeline is the module for generating centroidal trajectories. To be effective, these centroidal trajectories must be dynamically consistent, i.e., all the contact forces which drive the centroid must lie inside the friction cones. In addition, these trajectories must be kinematically feasible by the whole-body model. For instance, the CoM trajectory computed by the module must be achievable by the whole body when computing its inverse dynamics.

To solve this problem, we set up a multi-stage optimal control problem (OCP) over a sequence of contacts S of the following form:

$$\min_{\underline{\mathbf{x}},\underline{\mathbf{u}},(\Delta t_s)} \sum_{s=1}^{S} \int_{t_s}^{t_s+\Delta t_s} \ell_s(\mathbf{x},\mathbf{u}) - \log \underbrace{\mu_s(\mathbf{x},\mathbf{u})}_{\text{feasibility measure}} \, dt \tag{3.5a}$$

$$\text{s.t.} \quad \forall t \quad \dot{\mathbf{x}} = f(\mathbf{x},\mathbf{u}) \tag{3.5b}$$

$$\forall t \quad \mathbf{u} \in \mathcal{K} \tag{3.5c}$$

$$\mathbf{x}(0) = \mathbf{x_0} \tag{3.5d}$$

$$\mathbf{x}(T) = (\mathbf{c}_f, \mathbf{0}, \mathbf{0}), \ \dot{\mathbf{x}}(T) = \mathbf{0} \tag{3.5e}$$

where (3.5a) is the cost function we aim to minimize that contains a feasibility measure to encode the constraints of the centroidal dynamics w.r.t. the whole-body [Carpentier 2017a, Carpentier 2017b]. It also handles a tailored cost function ℓ_s that can be adjusted by the user to obtain smoother motions for instance, or to penalize some quantities. Eq. (3.5b) is the centroidal dynamics of the system with state $\mathbf{x} = (\mathbf{c}, m\dot{\mathbf{c}}, \mathcal{L}_\mathbf{c})$ composed of $\mathbf{c}$, the position vector of the CoM, the linear momentum $m\dot{\mathbf{c}}$, and the angular momentum $\mathcal{L}_c$. The control $\mathbf{u}$ is directly the ECW. To be effective, this ECW must remain inside a certain cone called the centroidal wrench cone expressed in (3.5c) and introduced in [Hirukawa 2006].

In [Carpentier 2017b], the authors suggested an efficient inner approximation of this cone that we used in this work. Finally, starting from an initial state (3.5d), the objective is to reach a final state at rest, encoded by Eq. (3.5e). In this implementation, the duration of each phase (Δt_s) was left as a free variable of the problem. To solve this optimal control problem, we used MUSCOD-II [Leineweber 2003], a multiple-shooting framework dedicated to problems having a shape similar to (3.5). In order to show the effects of our criterion, we provided the OCP solver with different cost functions ℓ_s:

1. In the first case, we investigated the minimization of the distance $d_{\mathbf{c}-\Delta}$ in addition to minimizing the kinetic energy of the system in translation. Thus, we chose $\ell_s = d_{\mathbf{c}-\Delta} + \alpha\, m\|\dot{\mathbf{c}}\|^2$, where α is a weighting coefficient. Typically, $\alpha = 0.1$.

2. In the second case, we left the distance free and the cost function was only composed of the kinetic term, leading to $\ell_s = m\|\dot{\mathbf{c}}\|^2$.

3.4.3 Simulation results

The simulated environment was an industrial stairway equipped with a handrail and made of four 15-cm high and 30-cm deep steps. Snapshots of the complete motion, result of the simulation, are depicted in Fig. 3.5. In Fig. 3.6 $d_{\mathbf{c}-\Delta}$ is displayed for the two cases of study. When $d_{\mathbf{c}-\Delta}$ is included in the cost function, it is successfully regulated to nearly zero during the whole motion. Fig. 3.7 shows control inputs that drives the centroidal dynamics in the two approaches. As a result of the solved OCP, when our criterion is added to the cost function, the derivative of angular momentum about x and y axes is nearly zero. Reaction forces being mostly vertical in this kind of motion, the fact that the z component of the angular momentum variation is not zero is consistent with Eq. (4) and with the fact that $d_{\mathbf{c}-\Delta}$ is regulated to almost zero. Furthermore, one can notice that minimizing the proposed criterion led to greater accelerations of the CoM. This might be the result of a tighter control of the position of the CoM for regulating $d_{\mathbf{c}-\Delta}$ to zero, together with a lesser emphasis placed on the minimization of the kinetic energy (α parameter). Fig. 3.8, displays the state of the centroidal dynamics for the two cases of study. Noticeably, including our criterion in the cost function results in a nearly zero angular momentum about the x and y axes which is an expected outcome of the computed optimal control.

3.4.4 Discussion

As mentioned earlier, minimizing $d_{\mathbf{c}-\Delta}$ leads to the minimization of either $\dot{\mathcal{L}}_{\mathbf{c}}$ or the angle between $\mathbf{f}_c$ and $\dot{\mathcal{L}}_{\mathbf{c}}$ or to the maximization of $||\mathbf{f}_c||$ (see Eq. (4)). This last strategy cannot be found by the solver since we also penalize the kinetic energy of the system in translation, which is equivalent to bound the variations of the linear acceleration of the centroidal dynamics [Wieber 2008]. Simulation results show

that in the context of stair climbing, the solution found by the optimal control framework is noticeably the same as if the criterion was to minimize $\dot{\mathcal{L}}_{\mathbf{c}}$. But given the different available strategies to control $d_{\mathbf{c}-\Delta}$, we claim that our criterion allows for more slackness in the resolution of the problem. Typically, it should succeed in the context of a movement that would require dynamical direction changes and thus, non-zero components of $\dot{\mathcal{L}}_{\mathbf{c}}$ along the direction of $\mathbf{f}$, a situation where harshly forcing $\dot{\mathcal{L}}_{\mathbf{c}}$ to zero would fail. Also, one could extend the use of this criterion in a cost function, in order to make it follow a human-inspired pattern, as the one depicted in Fig. 3.4. In this case, the solver would be able to find a whole-body strategy that involves contributions of all the limbs in the production of appropriate contact forces and angular momentum values, leading to a more dynamical, human-like locomotion. Implementing other motions using this criterion on the real robot is left as a future work.

3.5 Conclusion & perspectives

In this work, we combined biomechanical experiments and robotics simulations in order to introduce a new mechanical descriptor of bipedal locomotion, the distance between the CoM and the central axis of the ECW ($d_{\mathbf{c}-\Delta}$), and illustrated its application to the generation of humanoid motion. At first, significant variations in this distance have been measured during experiments on 15 volunteers. At the scale of the walking cycle, this quantity was shown to convey relevant information about the instantaneous dynamical state of the body. It was also statistically demonstrated that the average of $d_{\mathbf{c}-\Delta}$ increased with the complexity of the locomotion tasks, revealing information about the ongoing movement. In a second step, a conservative mechanical criterion was derived from this biomechanical study and implemented in an optimal control formulation in order to generate multi-contact motion for a humanoid robot and to observe its influence on numerical experiments. The results showed that the minimization of the distance $d_{\mathbf{c}-\Delta}$ led to a dynamically feasible motion for the robot, resulting from a whole body dynamics expected from the mechanical analysis.

In collaboration with the Institut de Bioméchanique Humaine Georges Charpak, further analyses are being carried out on locomotion data in lower-limb amputees wearing prosthetic devices. Their variation profiles of $d_{\mathbf{c}-\Delta}$ are being compared with those of healthy participants. This work could help identify how to adjust the prostheses and to what extent they modify natural locomotion.

We thank the volunteers who took part in the experiment. We warmly thank Dr. Robin Baurès, associate professor at the University of Toulouse for helping us with the statistics.

Chapter 4

On the coordination of highly dynamic human movements

An extension of the Uncontrolled Manifold approach applied to precision jump in parkour

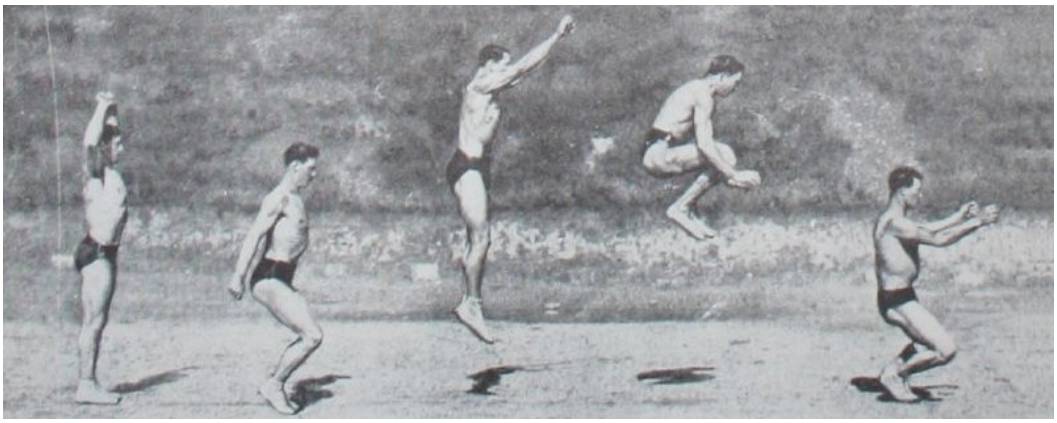

Figure 4.1: The word parkour derives from the classic obstacle course method of military training proposed by Georges Hébert (*Parcours du Combattant* in French). Here are displayed the five steps of the jump from Hébert's *Méthode Naturelle*.

Contents

4.1 Notions of motor control 58

4.1.1 Motor redundancy 58

4.1.2 Hierarchies of motor tasks 59

4.1.3 The Uncontrolled Manifold approach 59

4.1.4 Contribution to the field 61

4.2 Extending the uncontrolled manifold approach 61

4.2.1 Mathematical formulation of the UCM approach 61

4.2.2 Extending the UCM approach to dynamic tasks 62

4.2.3 An application to linear and angular momenta derivative tasks 65

4.3 Application to Take-off and Landing Motions in Parkour . 65

4.3.1 Precision jump and landing in parkour 66

4.3.2 Experimental materials and methods 66

4.3.3 Hypothesized task functions 68
4.4 Results 70
4.4.1 Take-off 70
4.4.2 Landing 71
4.5 Discussion 73
4.5.1 Landing 74
4.6 Conclusion and Perspectives 75

4.1 Notions of motor control

Motor control is an area of natural science studying how the CNS produces purposeful and coordinated movements in its interaction with the rest of the body and with the environment. In this chapter, some notions of motor control that are necessary to present our contribution to the field are briefly recalled. Then, an extension of the uncontrolled manifold approach for studying human motions is presented. Finally, the application of this extension to the study of precision jump in Parkour is reported.

4.1.1 Motor redundancy

The human body possesses more degrees of freedom than necessary to perform the majority of motor tasks. This so-called *motor redundancy* was first studied by the Russian physiologist Nikolai Bernstein [Bernstein 1967]. Bernstein highlighted that one consequence of this redundant organization is that many actions and movements can be executed in multiple ways. This implies that the CNS is able to synthesize a family of control solutions, involving the coordination of different control variables (neurons, muscles, kinematics, etc.) in order to achieve a desired motor behavior (evaluated through performance variables). In the motor control community, such equivalent families of control solution are called *synergies*, and interestingly, they are task-dependent and they are only present in expert performance, not in novices. They provide both flexibility and stability in the execution of the specific task they were learned for, because the control variables are informationally linked, allowing co-varying or compensating behaviors that prevent errors in individual motor components from affecting the performance variables. Following this idea, motor redundancy can be viewed as a benefit rather than a problem for the neuromotor system. According to this motor abundance principle [Gelfand 1998], redundant degrees of freedom are used to better achieve a steady motor solution in the sense of being robust against perturbations. Given the context, the movement might involve several tasks at the same time (e.g. trying to keep balanced, while executing another motor task, see Fig. 4.2). To deal with this apparent conflict, it has been proposed that the brain could organize tasks hierarchically to generate the motion [Todorov 2005, Gera 2010].

4.1.2 Hierarchies of motor tasks

As it was mentioned earlier, among the benefits of kinematic redundancy is the possibility of executing more than one task at the same time. Indeed, possessing a sufficient number of independent degrees of freedom is a necessary condition for achieving multitasking. But an appropriate control strategy has to be followed in order to execute secondary tasks without interfering with the execution of primary ones. This reasoning necessarily introduces priority levels among tasks which can be handled thanks to hierarchical control. Let us take the example of Fig. 4.2, where the balancing act takes place at different levels. First of all, the integrity of the artist implies that he does not fall from the unstable board he stands onto. For security reasons, this could certainly be identified as a first-level priority task. Then, in order to avoid breaking dishes, comes the delicate balancing of the bowls that are stacked on his head. Finally, grabbing an extra bowl could be identified as a third task, the completion of which would be conditioned to the completion of higher priority tasks.

To deal with multiple tasks at the same time, it has been proposed that the human brain could favor a hierarchical organization not only at the neuromotor level [Latash 2008], but also at the level of the tasks execution [Todorov 2005, Gera 2010]. Such a hierarchical control design at the task level has been widely used in robotics [refs], using similar mathematical tools to those used in motor control. Whether for modeling human motion generation or for generating complex robotic motions, the main idea is to exploit the null-space of the task Jacobian, in which a variation of the joint configuration (control variables) does not affect the execution of the task (performance variables). This concept is also used for finding out which performance variables are actually controlled during a particular motion, according to the uncontrolled manifold approach.

4.1.3 The Uncontrolled Manifold approach

The uncontrolled manifold (UCM) approach [Scholz 1999] is a computational method for answering the question of whether a task is preferentially controlled by the CNS during the execution of a particular motion. It is based on the consensus that a performance variable being controlled is stabilized against perturbations, which can be assessed by its variance across trials. In order to interpret the variance of performance variables (in the task space) relative to control variables (in the motor space), the idea of the UCM approach is to embed all variances into the joint space. This is classically done using the framework of the task function approach introduced in Sec. 2.5, thanks to the task jacobian, which is the linear mapping between the time derivative of the performance variables and the derivative of joint configuration (see Eq. 2.4). The structure of the variance in the joint space can then be analyzed by projection onto two subsets, the UCM that contains all combinations of joint configuration that do not alter the achievement of the task, and its orthogonal which contains the bad part of the variability, in the context of

Figure 4.2: What does it take not to fall from this wobbly structure, while keeping bowls balanced on your head? At least, three tasks are executed in parallel: keeping the body balanced on the unstable setup, maintaining the balance of the stack of bowls by controlling the head, all this while modifying the body configuration to grab another bowl. *Craig Nagy, Wikimedia Commons, CC BY-SA 2.0.*

stabilized performance variables. The UCM approach states that when the variance of control variables in the UCM (identified as good variability) is greater than the variance onto its orthogonal space, then the motor task is considered as being preferentially controlled by the CNS. The good variability can be linked to the notion of motor synergies introduced above.

To date, the UCM approach has been applied to the study of various motor tasks. Postural tasks have been studied through muscle modes [Danna-dos Santos 2007] and joint coordination [Hsu 2007]. Tasks such as pointing [Domkin 2005], reaching and grasping [Fan 2006], sit-to-stand [Scholz 2001, Reisman 2002], and drawing [Tseng 2006] have also been studied through joint coordination. Force production tasks have been investigated by considering finger forces [Latash 2001] and joint torques [Yen 2009]. However, most of these studies only accounted for quasi-static motor tasks, although most of human movements are inherently dynamic. In the study of Yen et al. [Yen 2009], the UCM approach was applied to study force tasks in single-leg hopping using the dynamic consistent Jacobian [Khatib 1987]. This mathematical formulation can only be applied for mono-contact force production tasks. Furthermore, this study considered segment angles as control variables in spite that they are dependent variables in a kinematic chain and that sensory receptors provide information to the CNS about changes

in joint angles according to physiology. The UCM approach has also been applied to study linear and angular momentum expressed at the CoM [Reisman 2002] in a sit-to-stand task and the angular momentum in human walking [Robert 2009]. The later study was preceded by a principal component analysis (PCA). This implies dimensionality reduction into principal components whose origin is not well understood and which contradicts the motor abundance principle.

4.1.4 Contribution to the field

In an article that was thought, prepared, and written in collaboration with Galo Maldonado ([Maldonado 2018a], in final review phase), a general framework was proposed to extend the formalism of the UCM approach to tasks in which movement dynamics matter. This framework required to consider higher order derivatives of the joint variables and respects the motor abundance principle. In the following, the content of this work is presented. The next section (Sec. 4.2) is first dedicated to present the mathematical formalism of the classical UCM approach, for educational purposes. Following what, we explain the proposed extension of the UCM approach for studying the organization of movements which are inherently dynamic. Then (Sec. 4.3), an experimental validation applied to specific whole-body parkour motions is presented, in which it is demonstrated that the CNS is able to coordinate degrees of freedom to achieve such an inherent highly dynamic and skilled task. A time-dependent hierarchical organization of tasks is also highlighted in this part.

4.2 Extending the uncontrolled manifold approach

The mathematical developments presented in the following section are literally taken from our article to be published in Scientific Reports [Maldonado 2018a]. They constitute my main contribution to this work.

4.2.1 Mathematical formulation of the UCM approach

Based on the task function approach presented in Sec. 2.5, the UCM approach [Scholz 1999] is formulated as follows. Consider that N_r repetitions of a studied movement have been recorded with one participant. For $r = 1, ..., N_r$, let us define by $\mathbf{q}_r(t)$ and $\mathbf{e}(\mathbf{q}_r(t))$ the joint configuration trajectory and the corresponding task function trajectory for the rth repetition respectively. Let $\bar{\mathbf{q}}(t)$ denote the mean value of the joints configuration trajectory across the N_r repetitions. At each time t, given the definition of the task Jacobian, the first order Taylor expansion of a task $\mathbf{e}(\mathbf{q})$ in the neighborhood of $\bar{\mathbf{q}}$ yields:

$$\forall r = 1, ..., N_r, \quad \mathbf{e}(\mathbf{q}_r) - \mathbf{e}(\bar{\mathbf{q}}) = J_e(\bar{\mathbf{q}})(\mathbf{q}_r - \bar{\mathbf{q}}) + \varepsilon(\mathbf{q}_r), \tag{4.1}$$

where $\varepsilon(\mathbf{q}_r)$ contains higher order terms of the expansion known as residual.
Considering the residual as negligible, for each repetition r, one can compute the projection $\mathbf{ucm}_r$ and $\mathbf{ucm}_{\perp,r}$ of the joint configuration deviation $\mathbf{q}_r - \bar{\mathbf{q}}$ respectively

onto the null space of the Jacobian matrix $J_e(\bar{\mathbf{q}})$ and onto its orthogonal space at each time as follows:

$$\mathbf{ucm}_r = P_e(\mathbf{q}_r - \bar{\mathbf{q}}), \tag{4.2a}$$

$$\mathbf{ucm}_{\perp,r} = (\mathbf{q}_r - \bar{\mathbf{q}}) - \mathbf{ucm}_r, \tag{4.2b}$$

where $P_e = \mathbb{1} - J_e^{\#} J_e$ is the projector onto the null space of J_e (e.g. $P_e J_e = 0$ and $P_e P_e = P_e$). The inter-trial variance of $\mathbf{ucm}_{r=1,\ldots,N_r}$ and $\mathbf{ucm}_{\perp,r=1,\ldots,N_r}$ respectively denoted by $V_{ucm} \in \mathbb{R}$ and $V_{ucm_\perp} \in \mathbb{R}$, are then normalized by the dimension of each space with $N_{ucm} = dim(\mathcal{Q}) - dim(\mathcal{M})$ and $N_{ucm_\perp} = dim(\mathcal{M})$. Note that in order to report the variability of $\mathbf{ucm}_r$ and $\mathbf{ucm}_{\perp,r}$ independently, one should also normalize by the number of repetitions. Then, an index of motor task control "ITC" can be calculated as the ratio between both variances:

$$V_{ucm} = \sum_{r=1}^{N_r} \frac{1}{n} ||\mathbf{ucm}_r||_2^2, \tag{4.3}$$

$$V_{ucm_\perp} = \sum_{r=1}^{N_r} \frac{1}{n} ||\mathbf{ucm}_{\perp,r}||_2^2, \tag{4.4}$$

$$ITC = \ln\left(\frac{V_{ucm} \cdot N_{ucm_\perp}}{V_{ucm_\perp} \cdot N_{ucm}}\right). \tag{4.5}$$

According to the UCM hypothesis, when the ITC is greater than 0, the motor task is considered as being preferentially controlled by the CNS [Nisky 2014, Scholz 1999]. Furthermore, the ITC can be used to quantify a hierarchical structure of motor tasks according to their apparent degree of importance in the generation of the motion. Note that when applying the UCM approach, the choice of hypothetically controlled elemental variables and performance variables must depend on the studied motion. For example, in a pointing task,the finger position ($\dim(\mathbf{e}(\mathbf{q})) = 3$) might be the performance variable whereas the upper-limb joints rotations might be the elemental variables.

In its classical formulation, the UCM approach involves task function $\mathbf{e}_r(\mathbf{q})$ that are expressed as joint position error between the current trial configuration of the joints and a mean reference behavior. In order to extend this approach to the study of the coordination of tasks where movement dynamics matters, we propose to consider candidate task functions that depend on higher order derivatives of the elemental variables. In the next section, we introduce the generalized framework for expressing these motor tasks.

4.2.2 Extending the UCM approach to dynamic tasks

The task Jacobian (Eq. (2.3)) is known to be the linear mapping between the time derivative of the task and the velocity of the elemental variables:

$$\dot{\mathbf{e}}(\mathbf{q}, \dot{\mathbf{q}}) = J_e(\mathbf{q})\dot{\mathbf{q}}. \tag{4.6}$$

In turn, $\dot{\mathbf{e}}(\mathbf{q}, \dot{\mathbf{q}})$ can be viewed as a new task function depending on $\mathbf{q}$ but also on $\dot{\mathbf{q}}$. This task function is well suited for describing differential behaviors as speed tracking tasks for instance. This motion description is still decoupled from the dynamics of the system and thus it does not take into account inertial effects that are essential for analyzing the movement dynamics. Now, if one wants to express the motion at the level of the dynamics, then task functions need to be related to higher order derivatives of the configuration variables. Indeed, it is well-known that rigid body dynamics is expressed as a function of the second order derivative of the joints variables [Saab 2011]. In order to express the system dynamics in the task space, Eq. (4.6) must be time differentiated:

$$\ddot{\mathbf{e}}(\mathbf{q}, \dot{\mathbf{q}}, \ddot{\mathbf{q}}) = \dot{J}_e(\mathbf{q}, \dot{\mathbf{q}})\dot{\mathbf{q}} + J_e(\mathbf{q})\ddot{\mathbf{q}}, \tag{4.7}$$

where $\dot{J}(\mathbf{q}, \dot{\mathbf{q}})\dot{\mathbf{q}}$ can be viewed as a dynamic drift of the task corresponding to nonlinear effects. In robotics, this expression has been used to formulate different kinds of tasks, for instance tasks for visual servoing [Chaumette 2006] or center of mass (CoM) trajectory control [Mansard 2009].
In the sequel, we propose to extend the UCM approach to task functions of the form of Eq. (4.6) and Eq. (4.7). As expressed in Eq. (4.6), $\dot{\mathbf{e}}$ is a function of $\mathbf{q}$ and $\dot{\mathbf{q}}$. The idea is to extend the UCM reasoning by writing down an approximation of $\dot{\mathbf{e}}$ around a particular mean behavior of the participant across trials $(\bar{\mathbf{q}}, \bar{\dot{\mathbf{q}}})$, by computing a first order Taylor expansion as in Eq. (4.1). To this end, the partial derivatives of $\dot{\mathbf{e}}$ need to be computed with respect to $\mathbf{q}$ and $\dot{\mathbf{q}}$ as follows:

$$\left.\frac{\partial \dot{\mathbf{e}}}{\partial \dot{\mathbf{q}}}\right|_{\mathbf{q}=\bar{\mathbf{q}}} \hat{=} A(\bar{\mathbf{q}}, \dot{\mathbf{q}}), \tag{4.8a}$$

$$\left.\frac{\partial \dot{\mathbf{e}}}{\partial \mathbf{q}}\right|_{\dot{\mathbf{q}}=\bar{\dot{\mathbf{q}}}} \hat{=} B(\mathbf{q}, \bar{\dot{\mathbf{q}}}). \tag{4.8b}$$

It is straightforward that $A(\bar{\mathbf{q}}, \dot{\mathbf{q}})$ does not depend on $\bar{\dot{\mathbf{q}}}$: $A(\bar{\mathbf{q}}, \dot{\mathbf{q}}) = J_e(\bar{\mathbf{q}})$. The calculation details for B are given in Appendix A:

$$B_{ij} = \sum_{k=0}^{n} \frac{\partial (J_e(\mathbf{q}))_{ik}}{\partial q_j} \bar{\dot{q}}_k. \tag{4.9}$$

This leads to the first order Taylor expansion of $\dot{\mathbf{e}}$ around $(\bar{\mathbf{q}}, \bar{\dot{\mathbf{q}}})$:

$$\dot{\mathbf{e}}(\mathbf{q}, \dot{\mathbf{q}}) - \dot{\mathbf{e}}(\bar{\mathbf{q}}, \bar{\dot{\mathbf{q}}}) = \underbrace{\left[\, B(\bar{\mathbf{q}}, \bar{\dot{\mathbf{q}}}) \;\middle|\; A(\bar{\mathbf{q}}, \bar{\dot{\mathbf{q}}}) \,\right]}_{J_{\dot{e}}} \begin{bmatrix} \mathbf{q} - \bar{\mathbf{q}} \\ \dot{\mathbf{q}} - \bar{\dot{\mathbf{q}}} \end{bmatrix} + \varepsilon(\mathbf{q}, \dot{\mathbf{q}}). \tag{4.10}$$

Similarly, $\ddot{\mathbf{e}}$ is a function of $\mathbf{q}$, $\dot{\mathbf{q}}$ and $\ddot{\mathbf{q}}$ (Eq. (4.7)). To express its first order

Taylor expansion around the mean behavior of the participant ($\bar{\mathbf{q}}$, $\bar{\dot{\mathbf{q}}}$, $\bar{\ddot{\mathbf{q}}}$), the partial derivatives of $\ddot{\mathbf{e}}$ need to be computed with respect to $\mathbf{q}$, $\dot{\mathbf{q}}$ and $\ddot{\mathbf{q}}$:

$$\left.\frac{\partial \ddot{\mathbf{e}}}{\partial \ddot{\mathbf{q}}}\right|_{\substack{\mathbf{q}=\bar{\mathbf{q}}\\ \dot{\mathbf{q}}=\bar{\dot{\mathbf{q}}}}} \hat{=} C(\bar{\mathbf{q}}, \bar{\dot{\mathbf{q}}}, \ddot{\mathbf{q}}), \tag{4.11a}$$

$$\left.\frac{\partial \ddot{\mathbf{e}}}{\partial \dot{\mathbf{q}}}\right|_{\substack{\mathbf{q}=\bar{\mathbf{q}}\\ \ddot{\mathbf{q}}=\bar{\ddot{\mathbf{q}}}}} \hat{=} D(\bar{\mathbf{q}}, \dot{\mathbf{q}}, \bar{\ddot{\mathbf{q}}}), \tag{4.11b}$$

$$\left.\frac{\partial \ddot{\mathbf{e}}}{\partial \mathbf{q}}\right|_{\substack{\dot{\mathbf{q}}=\bar{\dot{\mathbf{q}}}\\ \ddot{\mathbf{q}}=\bar{\ddot{\mathbf{q}}}}} \hat{=} E(\mathbf{q}, \bar{\dot{\mathbf{q}}}, \bar{\ddot{\mathbf{q}}}). \tag{4.11c}$$

In fact it is straightforward to demonstrate that $C(\bar{\mathbf{q}}, \bar{\dot{\mathbf{q}}}, \ddot{\mathbf{q}})$ does not depend either on $\bar{\dot{\mathbf{q}}}$ or on $\ddot{\mathbf{q}}$: $C(\bar{\mathbf{q}}, \bar{\dot{\mathbf{q}}}, \ddot{\mathbf{q}}) = C(\bar{\mathbf{q}}) = J_e(\bar{\mathbf{q}})$. The calculation details for D and E are given in Appendix A:

$$D_{ij} = \sum_{k=0}^{n} \frac{\partial(\dot{J}_e(\bar{\mathbf{q}}, \dot{\mathbf{q}}))_{ik}}{\partial \dot{\mathbf{q}}_j} \dot{q}_k + \delta_{jk}(\dot{J}_e(\bar{\mathbf{q}}, \dot{\mathbf{q}}))_{ik}, \tag{4.12a}$$

$$E_{ij} = \sum_{k=0}^{n} \frac{\partial(\dot{J}_e(\mathbf{q}, \bar{\dot{\mathbf{q}}}))_{ik}}{\partial q_j} \bar{\dot{q}}_k + \sum_{k=0}^{n} \frac{\partial(J_e(\mathbf{q}))_{ik}}{\partial q_j} \bar{\ddot{q}}_k, \tag{4.12b}$$

with δ, the Kronecker delta. This leads to the first order Taylor expansion of $\ddot{\mathbf{e}}$ around $\bar{\mathbf{q}}$, $\bar{\dot{\mathbf{q}}}$ and $\bar{\ddot{\mathbf{q}}}$:

$$\ddot{\mathbf{e}}(\mathbf{q}, \dot{\mathbf{q}}, \ddot{\mathbf{q}}) - \ddot{\mathbf{e}}(\bar{\mathbf{q}}, \bar{\dot{\mathbf{q}}}, \bar{\ddot{\mathbf{q}}}) =$$

$$\underbrace{\left[\begin{array}{c|c|c} E(\bar{\mathbf{q}}, \bar{\dot{\mathbf{q}}}, \bar{\ddot{\mathbf{q}}}) & D(\bar{\mathbf{q}}, \bar{\dot{\mathbf{q}}}, \bar{\ddot{\mathbf{q}}}) & C(\bar{\mathbf{q}}) \end{array}\right]}_{J_{\ddot{e}}} \left[\begin{array}{c} \mathbf{q} - \bar{\mathbf{q}} \\ \dot{\mathbf{q}} - \bar{\dot{\mathbf{q}}} \\ \ddot{\mathbf{q}} - \bar{\ddot{\mathbf{q}}} \end{array}\right] + \varepsilon(\mathbf{q}, \dot{\mathbf{q}}, \ddot{\mathbf{q}}). \tag{4.13}$$

From these matrix formulations of the first order Taylor expansions of $\dot{\mathbf{e}}$ and $\ddot{\mathbf{e}}$ (Eqs. (4.10) and (4.13)), one can directly apply the UCM approach previously recalled, by computing the null space of $J_{\dot{e}}$ and $J_{\ddot{e}}$ respectively. Then, by projecting the variation of elemental variables with regard to the mean reference behavior onto the null space and its orthogonal, one can compute $\mathbf{ucm}_r$ and $\mathbf{ucm}_{\perp,r}$, as in Eqs. (4.2a) and (4.2b). The computation of the ITC (Eq. (4.5)) is then performed to conclude whether the task under study is preferentially controlled by the CNS or not. In the sequel, a direct application of this UCM extension is made to illustrate the framework. To this end, we study linear and angular momenta derivative task functions that are hypothesized to be preferentially controlled by the CNS during jump and landing motions in parkour. Before introducing the experimental procedure and the results, let us show how the proposed extension can be applied to this specific case study.

4.2.3 An application to linear and angular momenta derivative tasks

The hypothesized tasks are related to the linear and angular momenta derivatives (a justification for this choice is provided in the following section). Momenta tasks can be computed based on the centroidal dynamics: the dynamics expressed at the CoM of the whole body [Orin 2013]. The centroidal momenta matrix $A_c(\mathbf{q}) = I_{sys}J_{sys}$, which is the product of the system inertia matrix I_{sys} and the system Jacobian J_{sys} as described by Orin et al., maps the system joint velocities $\dot{\mathbf{q}}$ to the centroidal momenta $\mathbf{h_c} = \left[\mathbf{p}^T,\ \mathcal{L}_\mathbf{c}{}^T\right]^T$ as follows:

$$\mathbf{h_c} = A_c\dot{\mathbf{q}}, \tag{4.14}$$

where $\mathbf{p} = m_{body}\dot{\mathbf{c}}$ is the linear momentum with m_{body} the total body mass and $\dot{\mathbf{c}} \in \mathbb{R}^3$ its CoM velocity, and $\mathcal{L}_\mathbf{c}$ is the angular momentum of the body expressed at its CoM position $\mathbf{c} \in \mathbb{R}^3$ as:

$$\mathcal{L}_\mathbf{c} = \sum_{k=1}^{K}(\mathbf{c}_k - \mathbf{c}) \times \mathbf{p}_k + \mathcal{L}_{\mathbf{c_k}}, \tag{4.15}$$

where $\mathbf{c}_k \in \mathbb{R}^3$ is the position vector of the CoM of the kth segment, $\mathcal{L}_{\mathbf{c_k}}$ is the angular momentum of the kth body segment about its own CoM $\mathbf{c_k}$ and $\mathbf{p_k}$ is the linear momentum of the kth segment.

Furthermore, the time derivative of Eq. (4.14) gives the momenta derivative and results in the following equation:

$$\dot{\mathbf{h}}_\mathbf{c}(\mathbf{q}, \dot{\mathbf{q}}, \ddot{\mathbf{q}}) = A_c(\mathbf{q})\ddot{\mathbf{q}} + \dot{A}_c(\mathbf{q}, \dot{\mathbf{q}})\dot{\mathbf{q}}, \tag{4.16}$$

where $\dot{\mathbf{h}}_\mathbf{c} = \left[\dot{\mathbf{p}}^T,\ \dot{\mathcal{L}}_\mathbf{c}{}^T\right]^T$ represents the time derivative of the centroidal momenta. This notation is a compact formulation that embeds the three components of the Linear Momentum Derivative (LMD(x), LMD(y) and LMD(z)) and the three components of the Angular Momentum Derivative (AMD(x), AMD(y) and AMD(z)). Eq. (4.16) matches the pattern of Eq. (4.7) and thus can be used as a task function under the presented formalism. Hence, the application of the UCM approach to Eq. (4.16) requires to compute its partial derivatives which are similar to the ones of Eq. (4.7) (Eqs. (4.11a), (4.11b) and (4.11c)). The detailed expressions of these terms are developed in Appendix B.

4.3 Application to Take-off and Landing Motions in Parkour

The application of the UCM extension to the analysis of a jump motion in parkour is presented in what follows. The design of the experiment and the recording of the experimental data are the work of Galo Maldonado. We performed the

analysis and the interpretation of the results together. For the sake of clarity, the experimental part is briefly exposed before detailing the analysis and interpretation of the results. For more details on the experimental setup, please refer to the thesis of G. Maldonado and to [Maldonado 2018a]. This section is adapted from our article under review in Scientific Reports.

4.3.1 Precision jump and landing in parkour

Parkour is a training discipline involving whole-body motions in natural and complex environments (see Fig 4.1). Parkour practitioners – named traceurs – develop highly skilled and dynamic techniques that require an athletic shape as well as the ability to *read* environmental features in order to elaborate motion strategies that exploit these features to navigate in several ways. These techniques include versatile jump, landing, climbing and vaulting. In the following case of application, the work is focused on precision jump and landing techniques. They require traceurs to jump using both feet in parallel while swinging the arms and bending the knees to project the body forwards appropriately. At landing, traceurs have to land with precision on their forefoot without heel contact with the ground, bend their lower-limb joints without any varus-valgus motion of the knees and use their arms to counterbalance the movement and stabilize themselves.

4.3.2 Experimental materials and methods

4.3.2.1 Participants

Seven healthy trained male traceurs (age: 23.5 ± 3.1 y, height: 1.72 ± 0.07 m, mass: 69.2 ± 6.8 kg) volunteered for this study. Their experience in parkour practice was 5.7 ± 2.8 y. The subject exclusion criterion was based on history of lower extremity injuries or diseases that might affect landing biomechanics. Prior to participation in the experiments, informed written consent was obtained from participants. The experiments were conducted in accordance with the standards of the Declaration of Helsinki (rev. 2013) and approved by the ethics evaluation committee of INSERM (IORG0003254,FWA00005831) and the Institutional Review Board (IRB00003888) of the French Institute of medical research and Health.

4.3.2.2 Experimental protocol

Participants performed a warming up session followed by a familiarization period during which they were provided with the protocol instructions and they got accustomed to the laboratory environment. A total of 8 successful repetitions per participant was recorded according to our pretests during which we verified that fatigue and pain were minimized. During the experimental protocol, fatigue was controlled by including resting times of at least 3 minutes between repetitions [Standing 2015] and by getting oral feedback from practitioners. The landing protocol included a jump from 75% of the participant's height toward a target

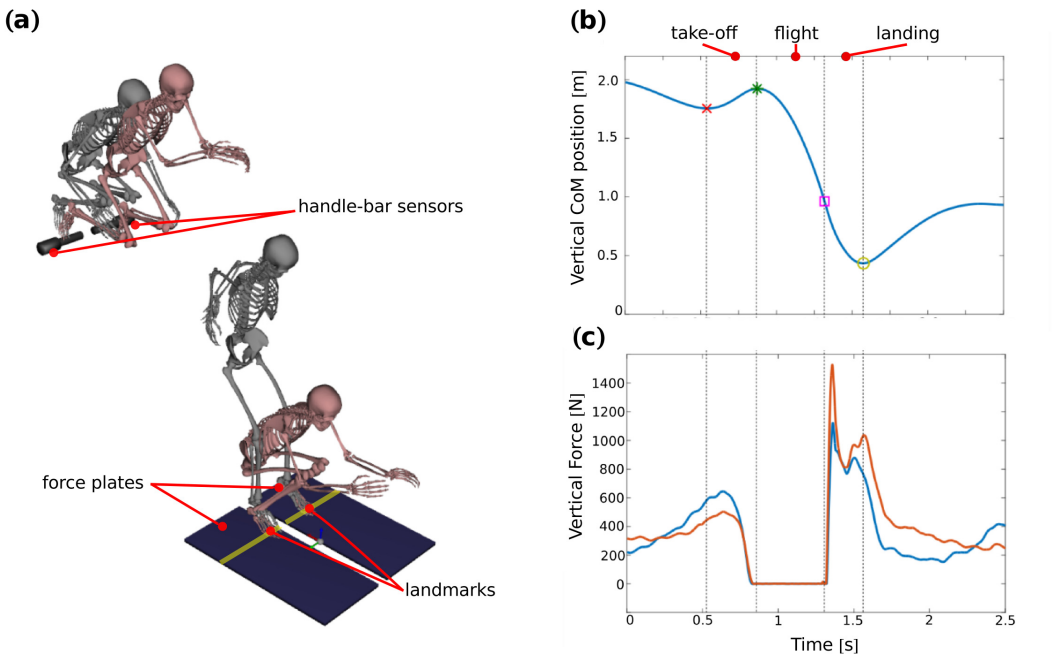

Figure 4.3: Experimental setup and motion analysis for the parkour precision technique. (a) The highest and the lowest two skeletons illustrate the beginning and the end of the take-off and of the landing motion, respectively. (b) Vertical trajectory of the CoM during the whole motion. (c) Vertical reaction force profiles during the whole motion. *From [Maldonado 2018a].*

landmark placed on the floor at a distance equal to the square of the jump height (Fig. 4.3). Participants were asked to land on the target landmark and to stabilize their posture using the parkour precision technique. Only successful trials were taken into account.

4.3.2.3 Skeletal model

A whole-body 3D model including 42 degrees of freedom and 19 body segments was used to reconstruct the main elementary movements of each traceur. This model is limited to joints that are relevant for the task and includes some simplifications. A 3D model is required because, as shown in previous studies [Hickox 2016], a simpler sagittal model is not sufficient to study the upper body motion during standing long jumps.

4.3.2.4 Data acquisition

For details about data acquisition, please refer to Sec. 3.3.2. Acquisition frequencies, infrared cameras and forces sensors are the same except that two handles were used in this experiment (see Fig. 4.3). Force data were used to double-check the computations of the momenta derivative and to define the onsets of the motion phases (% of the motion).

4.3.2.5 Data analysis

Kinematics and kinetics were processed with the same cut-off frequency [Kristianslund 2012] using a low-pass Butterworth digital filter of 4th order applied in zero-phase. A cut-off frequency of 35 Hz was used after a residual analysis [Winter 2009]. The introduced whole-body model was used to compute inverse kinematics which was solved with OpenSim [Delp 2007] by minimizing the squared distance between recorded and virtual markers [Lu 1999] and by using the Euler xyz body-fixed rotation angles [Seth 2010]. The free-flyer joint (root frame, six degrees of freedom) was not taken into account in the control variables. Indeed, according to the dynamic equations of poly-articulated systems, this joint is under-actuated by the action of the body joints and therefore cannot be directly controlled.

4.3.2.6 Statistical analysis

Individual statistical studies were conducted for the take-off and landing motions. All data are presented as the mean $\pm$ the confidence interval. The normality of the data was assessed with the Shapiro–Wilk test. The p-value for determining statistical significance of hypotheses was $p = 0.05$. To statistically verify if motor task functions were preferentially controlled by the CNS, unpaired t-tests comparing the ITC value with a zero mean were performed. To investigate if task hierarchies could be identified in the organization of the motion and to assess the temporal evolution of ITC values during each motion, a repeated measures ANOVA (task $\times$ phase, take-off: 2×4, landing: 3×5) with the phases and the tasks as within-subjects factors was performed. Paired t-tests with the Bonferroni correction were then carried out to assess main effects. Finally, the eta-squared method was used to test the effect size on the measures and the power of the statistics.

4.3.3 Hypothesized task functions

Following the concept of the UCM approach, the idea of this case of application study was to highlight potentially controlled task functions during the precision jump and landing in traceurs. Hypothesized task functions of this motion were chosen according to the literature and the observation of recorded pretests. Selected task functions were related to linear and angular momenta. Besides testing whether these task functions were preferentially controlled by the CNS or not, our goal was also to check for the existence of a hierarchical structure of functions that could help describe the whole motion organization (e.g. performing the precise landing versus avoiding tipping over or getting injured).

4.3.3.1 Motion phases

The motion was divided into three sub-motions: take-off, flight and landing. As our goal was to focus on momenta task functions, which are conserved quantities

during the flight (according to Newton's laws of motion), we decided to exclude the flight motion from our analysis. The take-off phase was defined between the time at which the height of the CoM was minimal and the last foot contact instant. The flight phase was defined between the end of the take-off phase and the initial contact with the ground, defined as the time at which the vertical ground reaction force reached 50 [N]. The landing phase was defined between initial contact with the ground and the time at which the height of the CoM became minimal. The phases were normalized by time duration from 0% to 100% (Fig. 4.3).

4.3.3.2 Motor task functions during take-off

During the take-off motion, one condition for the traceur to succeed his jump is to drive their CoM to the appropriate initial conditions for the beginning of the flight phase. The CoM velocity, both in norm and in direction, has to be precisely tuned. For doing so, the traceur can regulate the external force profile applied to his body, whose integration during the take-off period is proportional to its CoM velocity. According to the experimental setup, the traceur was already aligned with the target in the horizontal direction (x), as a result, the first selected task function was:

- "LMD(y,z)": A task function that reflects the control of the forces to generate the required CoM velocity expressed in terms of the antero-posterior (A-P) and vertical components of the linear momentum derivative (LMD).

Furthermore, it has been shown that swinging the arms contributes to increasing the impulsion, and therefore the CoM velocity, through joint torque augmentation [Cheng 2008, Hara 2006] and that it improved the performance by alleviating excessive forward rotation [Ashby 2002] and contributing to properly position the body segments for landing [Ashby 2006]. Accordingly, the second selected task function was:

- "AMD(y)": A task function that enhances the traceur's performance when jumping and contributes to preparing the body posture for landing in terms of the A-P component of the angular momentum derivative (AMD) expressed at the CoM.

4.3.3.3 Motor task functions during landing

Throughout the landing motion, one objective of the traceur is to bring his CoM position to static equilibrium (right up to the target) and his CoM velocity to zero. Naturally, at the beginning of the landing phase, the conditions are far from this objective (reasoning on the energy of the system, one can see that a lot of potential energy has to be dissipated before achieving the required static equilibrium). In addition to that, care must be taken with pain and injury prevention. Indeed, trying to land without an appropriate strategy could lead to bone fractures and lesions.

It was shown that traceurs are able to reduce the vertical ground reaction forces (GRFs) and the loading rate in order to prevent pain and injury [Standing 2015]. Moreover, traceurs are able not only to land safer but also to better control their posture through the modulation of A-P and medial-lateral (M-L) components of the GRFs [Maldonado 2015]. As a result, the first selected tasks were:

- "LMD(z)": A task function that reflects a strategy to guarantee a safe landing execution by lowering the vertical reaction forces and the loading rate. This task function is expressed in terms of the vertical component of the LMD.
- "LMD(x,y)": A task function that reflects a strategy of postural control in terms of the M-L and A-P components of the LMD.

The angular momentum derivative expressed at the CoM was also reported to be regulated during parkour landings [Maldonado 2017]. Accordingly, the second selected task function was:

- "AMD(x,y,z)": A task function that reflects a falling-down avoidance strategy through rotational motions around the body principal axes expressed in terms of the AMD. This task function might also contribute to injury prevention by decreasing the varus-valgus motion of the knees.

4.4 Results

The Index of Task Control (ITC) refers to the ratio between the variance in the UCM and in its orthogonal. According to the UCM hypothesis, when the ITC is greater than 0, the motor task is considered as being preferentially controlled by the CNS. ITC values were always positive for all the hypothesized task functions during take-off and landing. Moreover, task functions had significantly different levels of ITC.

4.4.1 Take-off

Each of the two hypothesized task functions turned out to be preferentially controlled at each motion phase ($p < .001$) (Table 4.1). Indeed, during the whole motion, ITC indexes are higher than 0. Thus, the derivative of the linear momentum along y and z (LMD(y,z)) and the derivative of the angular momentum around z (AMD(y)) appear to be preferentially controlled by the CNS during the take-off (Fig. 4.4). A repeated measures analysis of variance of the ITC emphasized a main effect for the task factor ($F(1,6) = 36.77,\ p < .001,\ \eta^2 = .86,\ f = 2.47$). No significant effect was observed for the phase factor ($F(3,18) = 2.74,\ p = .071,\ \eta^2 = .31,\ f = 2.47$). Furthermore, post-hoc comparisons using paired t-tests with the Bonferroni correction ($p/4$) indicated that task functions ITCs were significantly different at the 1% ($p = .005$), at 40% ($p = .002$) and at 100% of the motion ($p = 0.042$).

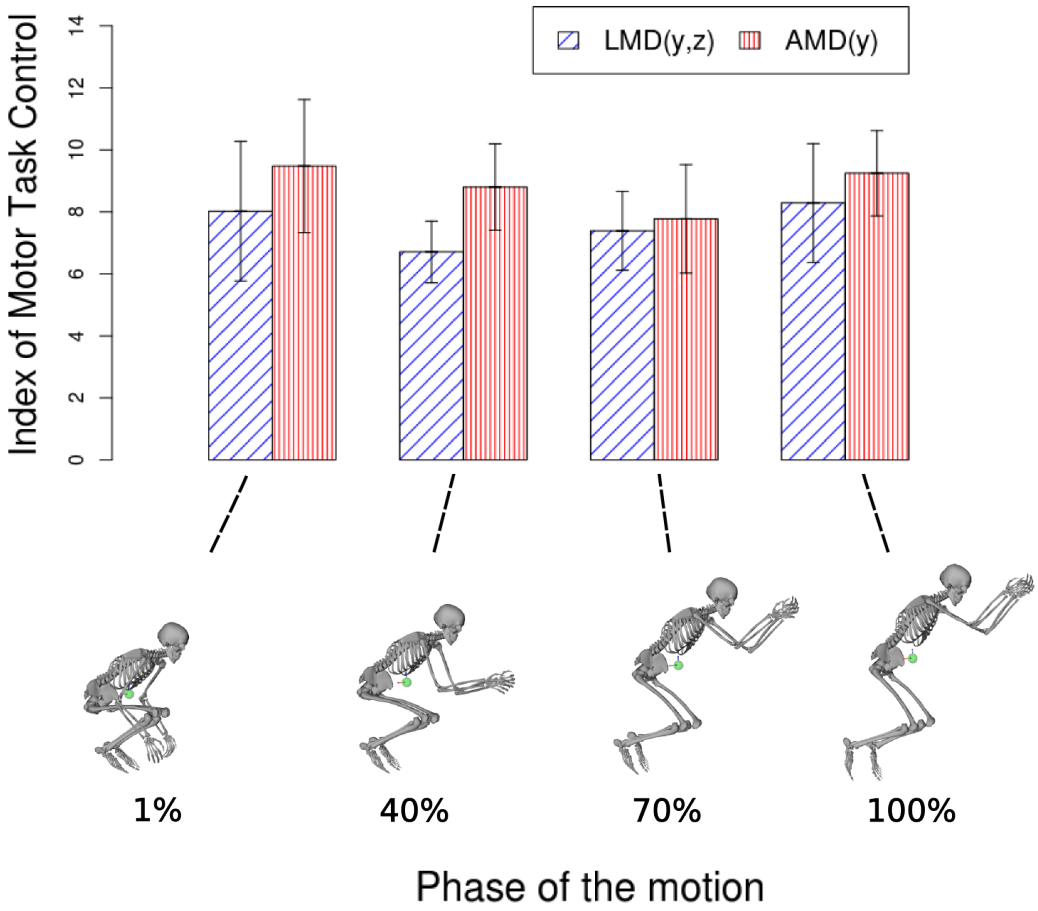

Figure 4.4: Mean (± confidence intervals) values of the indexes of task control (ITC) during the take-off motion for the LMD(y,z) and the AMD(y) task functions, at each selected phase (1, 40, 70 and 100%.) Below: corresponding snapshots of the reconstructed motion. *From [Maldonado 2018a].*

Rank	Phases			
	1%	**40%**	**70%**	**100%**
1	AMD(y) ∗	AMD(y) ∗	AMD(y)	AMD(y) ∗
2	LMD(y,z)	LMD(y,z)	LMD(y,z)	LMD(y,z)

Table 4.1: ITC-based hierarchical organization of the task functions during the take-off motion. ∗ stands for AMD(y) ITC significantly different from LMD(y,z) ITC.

4.4.2 Landing

Both the derivatives of the angular and linear momenta in the three directions were preferentially controlled by the CNS at each motion phase ($p < .001$) during landing (Fig. 4.5). A repeated measures analysis of variance of the ITC indicated a main

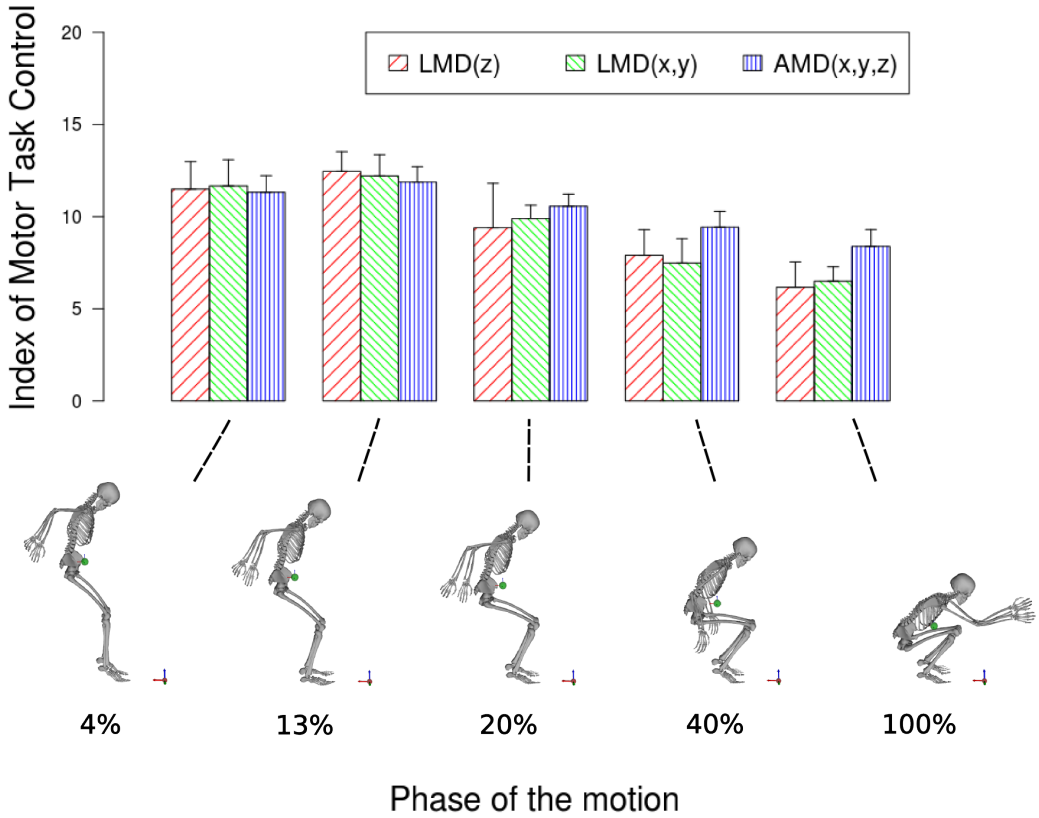

Figure 4.5: Mean (± confidence intervals) values of the indexes of task control (ITC) during the landing motion for the LMD(z), LMD(x,y) and the AMD(x,y,z) task functions, at each selected phase (4, 13, 20, 40 and 100%.) Below: corresponding snapshots of the reconstructed motion. *From [Maldonado 2018a].*

effect for the task factor ($F(2,12) = 14.23,\ p < 0.001,\ \eta 2 = 0.70,\ f = 1.54$) and for the phase factor ($F(4,24) = 67.4, p < 0.001, \eta 2 = 0.91, f = 3.35$). Post-hoc comparisons using paired t-tests with Bonferroni correction corroborated that task functions ($p/15$) were significantly different ($p < 0.001$) (Table 4.2) and that ITC values of the phases ($p/10$) evolved differently with time (Table 4.3). Fig. 4.5, displays the decrease of each task function after the first 13% of the motion. This shows that the control appears to be more important at the beginning of the landing phase, for the LMDs and AMD task functions. Moreover, Table 4.2 shows that at 20%, 40% and 100% of the landing phase, AMD(x,y,z) and LMD(x,y)'s ITCs were significantly different and that at 13%, 40% and 100%, AMD(x,y,z) and LMD(z)'s ITCs were significantly different. Table 4.3 contains the evolution of each ITC index during the landing phase. LMD(z)'s ITC was significantly smaller at 40% and 100% with regard to 4% and 13% (it decreased at the end of the landing phase). In a same manner, the ITC values of LMD(x,y) and AMD(x,y,z) significantly decreased during the landing phase. Table 4.4 shows which task function was prioritized by the CNS at each phase of the landing: LMD(z) at 13% of the landing phase, then

AMD(x,y,z) from 20%, up to 100%).

	Phases				
Task Functions Comparison	**4%**	**13%**	**20%**	**40%**	**100%**
LMD(z) & LMD(x,y)	1	1	1	1	1
LMD(x,y) & AMD(x,y,z)	.94	.59	.044	.003	<.001
LMD(z) & AMD(x,y,z)	1	.011	.275	.005	.004

Table 4.2: ITC pairwise comparisons using paired t-tests for the task factor during the landing phases. $p-$values are adjusted with the Bonferroni correction.

	LMD(z)				**LMD(x,y)**				**AMD(x,y,z)**			
Phase	**4%**	**13%**	**20%**	**40%**	**4%**	**13%**	**20%**	**40%**	**4%**	**13%**	**20%**	**40%**
13%	.674	-	-	-	1	-	-	-	1	-	-	-
20%	.284	.092	-	-	.102	.005	-	-	1	.05	-	-
40%	.007	.001	.592	-	.008	<.001	.005	-	.064	.002	.065	-
100%	.002	<.001	.079	.088	<.001	<.001	<0.001	.041	.005	<.001	.024	.067

Table 4.3: ITC pairwise comparisons using paired t-tests for the phase factor during the landing phases. $p-$values are adjusted with the Bonferroni correction.

	Phases				
	4%	**13%**	**20%**	**40%**	**100%**
1	LMD(x,y)	LMD(z)†	AMD(x,y,z) ∗	AMD(x,y,z) ∗‡	AMD(x,y,z) ∗‡
2	LMD(z)	LMD(x,y)	LMD(x,y)	LMD(z)	LMD(x,y)
3	AMD(x,y,z)	AMD(x,y,z)	LMD(z)	LMD(x,y)	LMD(z)

Table 4.4: ITC-based hierarchical organization of the task functions during the landing motion. ∗, † and ‡ stand for significantly different from LMD(x,y), AMD(x,y,z) and LMD(z), respectively.

4.5 Discussion

The hypothesized motor task functions in this study were chosen according to the physics of the motion and the literature. The UCM extension was used to verify whether these task functions are being preferentially controlled by the CNS during the parkour motion. Results reveal that the CNS is able to coordinate complex whole-body motion strategies, which lead to the control of the hypothesized dynamic task functions. The higher the ITC, the more the task function appears to be preferentially controlled by the CNS. As a consequence, the values of ITCs associated to different task functions reveal the level of involvement of each of them in the achievement of the task. This involvement is interpreted in terms of task hierarchy in the proposed framework. Moreover, the time decomposition of the motion phases reveals that the amount of control dedicated to a task function might not depend on the task function only but also on the phase of the motion. This might be interpreted as a time-dependent task hierarchical control used by the CNS to organize the motion. In the sequel, we discuss the results obtained

by analyzing the proposed extension of the UCM approach to take-off and landing motions in parkour.

Take-off

The ITC of the LMD(y,z) task function, which is expressed in terms of the A-P and vertical components of the linear momentum derivative, reveals that this task function is preferentially controlled during the take-off motion. This is consistent with the physics of the problem: the traceur has to drive his CoM up to a certain velocity in order to precisely determine the ballistic motion of his body during the flight phase [Wakai 2005]. This velocity is obtained by integrating over time the acceleration of the CoM, which is the result of the forces applied by the participant on the ground (Newton's second law). The time integration of the forces exerted on the ground must therefore be precisely controlled at each time step during the take-off.

The AMD(y) task function, which is expressed in terms of the A-P component of the angular momentum derivative expressed at the CoM, is also preferentially controlled by the CNS during the take-off phase. Its ITC value turns out to be greater than in the LMD(y,z) task function throughout the take-off motion. This result makes sense with regard to Euler's law of motion and the conservation of angular momentum in the sense that, after the very moment of contact loss and during the whole flight, traceurs will not be able to change their angular momentum. As a consequence, excessive rotational motions must be avoided. Another reason for traceurs to control the AMD(y) before flying is to ensure they can reach an appropriate posture in preparation for landing [Ashby 2006]. The leaning forward position of the traceur (Figure 4.4) and the gravity force, are used to generate a net torque at the CoM which has to be counteracted throughout the take-off in order to reach the desired angular momentum. To this end, the observed strategy of the arms, pelvis, trunk and head swings contributes to counterbalance the forward sagittal angular momentum [Ashby 2002]. This upper body strategy permits lower limbs to be more involved in the production of the impulsion torques without having to compensate for the forward momentum [Ashby 2002]. This complex inter-limb coordination highlights the importance of controlling the AMD(y) task function as corroborated by our results.

The AMD(y) task function is significantly more controlled at the beginning and at the end of the take-off. This might reflect that ensuring a correct body posture before landing is more important than generating the desired ballistic trajectory of the CoM. A wrong control of the angular momentum during the take-off might imply falling down and getting injured at landing.

4.5.1 Landing

The LMD(z) task function, which is expressed in terms of the vertical component of the linear momentum derivative, is controlled throughout the landing motion.

From the beginning and up to 20% of the motion, the vertical force is controlled so that the peak loading rate and the peak forces can be reduced [Standing 2015]. This contributes to preventing pain and injuries [Gittoes 2012]. During the remaining of the landing, this task function is kept controlled. This is not surprising when considering that the time integration of this force provides the vertical deceleration of the CoM.

The LMD(x,y) task function, which is expressed in terms of the M-L and A-P components of the linear momentum derivative, is also controlled during the whole landing. This is expected during this process because the resulting GRF direction, which depends on the amount of M-L and A-P forces with regard to the normal force must remain inside the friction cones of contact in order to avoid slipping. Moreover, the LMD(x,y) task function affects the center of pressure (CoP) position, which reflects the neuromuscular postural control. Note that, in order to reach static equilibrium — which is the final goal of the parkour technique —, the CoP must finally coincide with the projection of the CoM on the ground. The LMD(x,y) task function is also linked to the forward deceleration of the CoM.

The AMD(x,y,z) task function, which is expressed in terms of the 3 components of the angular momentum derivative expressed at the CoM, is also controlled during landing. Due to the conservation of angular momentum principle, the value of the AMD before the impact is zero. Right after it, because of the external forces and torques, the AMD increases. One way to compensate this augmentation in order to keep balance, is to limit the derivative of joint torques during the landing phase. One can note that the pre-activation of muscles in preparation for landing [Yeadon 2010] contributes to keep the derivative of joint torques into reasonable bounds. This strategy might also be responsible for the apparent smoothness of the motion in terms of compliance and style. Furthermore, controlling the AMD(x,y,z) around the vertical axis contributes to reduce the varus-valgus motion and can be an injury prevention mechanism.

Two hierarchies of task functions and a temporal evolution of the ITC value were observed during the landing phase. At 13% of the motion, traceurs appear to control more the LMD(z) task function. The AMD(x,y,z) task function is significantly more controlled throughout the end of landing (from 20% to 100%). Note that after 20% of the landing, the vertical force is lowered. This control might be used to perform small postural adjustments thanks to the observed segment cancellation strategy [Maldonado 2017].

4.6 Conclusion and Perspectives

This study proposed a general framework for identifying dynamic task functions that appear to be preferentially controlled by the CNS in humans, based on the task function approach used in robotics and on an extension of the UCM approach. This theoretical contribution is illustrated by the study of parkour movements for which task functions are formulated in terms of whole-body linear and angular momenta

derivatives. Based on the analysis of the considered parkour motions, reasonable assumptions about which physical quantities are preferentially controlled by the CNS during the take-off and landing phases were made. By using the proposed UCM extension to study the organization of highly dynamic and skilled tasks, consistent computational arguments were provided to demonstrate that different components of linear and angular momenta are organized by the CNS which exploits motor abundance during successive phases of the parkour motion. This study also reveals the potential of the proposed method for identifying the hierarchical organization of task functions during complex human motions. This organization should be useful by the CNS to generate precise, dynamic, stable and injury-free motions.

The proposed extension of the existing approach to the study of human motions in which the dynamics matters is also promising for the synthesis of task-based motion generation algorithms for anthropomorphic systems. These results might also be useful in the frameworks of computer animation and humanoid robotics to generate human-inspired motions. Future works might be oriented towards testing different tasks under other experimental protocols to demonstrate the sensitivity of the proposed method with non-controlled task functions. The main limitation of the proposed approach lies in the inherent errors of biomechanical methods that are related to human movement analysis (experimental protocol, scaling of anthropomorphic data, inverse kinematics, ...).

We wish to thank all the volunteer traceurs who took part in the experimental part of this study.

Part III

From centroidal state estimation in engineering to state observation in animals

Whether in engineering or in animals, closed-loop control strategies are the foundation of robust and adaptive behaviors. As noted in Sec. 2.2, such control strategies depend on the state of the system and, therefore, they rely on state observation. The control of legged robots is no exception to this rule. However, the complexity and the size of a system such as a humanoid robot impels engineers to control a simplified model of it and thus to opt for streamlined state representations. The very same question of simplified state representation applies when the purpose is to describe a complex system, as it is the case in biomechanics. Though simpler, the chosen state representation has to capture the main physical behaviors of the system in order to describe it properly or to make it possible to design a suitable control for it.

In the context of locomotion, the centroidal state of a mechanical system (already introduced in Secs. 3.4 and 4.2.3), is a good candidate for addressing this problem, as its number of variables is drastically reduced and, in the same time, it encompasses information about the gravity, the interaction forces/moments and the effects of whole body motions projected at the CoM (see Sec. 6.2 for further details). In humanoid robotics, the relevance of centroidal state control for multi-contact locomotion has been thoroughly demonstrated [Orin 2013, Carpentier 2016b]. However, it should be noted that controlling such a reduced model of the robot cannot immediately provide a full joint control. The final joint trajectories are subsequently obtained by imposing additional constraints or tasks (see Sec. 3.4).

Our work was motivated by the lack of reliable centroidal state estimation methods for the closed-loop control of legged robots and the straight compatibility of these approaches with human motion analysis. In the following, Chaps. 5 and 6 present two technical contributions on the estimation of physical quantities related to the dynamics of the CoM of a polyarticulated system in contact. The first contribution is a method for recursively estimating the CoM position and the angular momentum derivative of the body expressed at the CoM. The second one is a method for optimally estimating the full centroidal state of a system in contact, using the differential dynamic programming algorithm. Both were built in such a way that they can be used either in legged robotics or in biomechanics.

The presented techniques for estimating the centroidal state of systems in contact involve elaborated signal processing and optimization algorithms. They illustrate that, using signals similar to the physiological ones, such as force sensors, kinematic proprioception, etc., the centroidal dynamics is not straightforward to estimate even though it only contains position, velocity, acceleration and mass information. One reason for this apparent difficulty is that the CoM, which is configuration-dependent, is a moving point in any frame fixed to the body, and thus it is technically not possible to measure its state directly by attaching and IMU (or an inner ear) to it. Interestingly, when looking at animals which are living models of adapted motor behaviors and which therefore obviously master the control of their centroidal dynamics, the biological sensory solutions are different with regard to this problem. It appears that animals decouple external state observation (i.e. the underactuated part of their dynamics) from proprioception (i.e. the actuated part) which amounts to estimate their full state. For doing so, whether it is in insects, fishes, birds, mammals, etc., the exteroceptive sensory organs which enable to measure the underactuated dynamics (eyes, ears, inner ears, sonars, etc.) are attached to one body, their head, which is anatomically distant from their CoM. Then, this paradigm is quite different because if the CoM plays a central role in the reduced models and in the control algorithms developed by engineers as well as in the laws of motion, in living organisms, it is the head that seems to be fundamental for state estimation through exteroceptive perception. Starting from this statement, Chap. 7 presents a multidisciplinary and prospective work about the role of the head for state estimation and perception in organisms, and the relevance of such a solution for mobile robotics systems.

Chapter 5

State estimation for systems in contact

Recursive estimation of the center of mass position and angular momentum variation of the human body

*This chapter is literally taken from our article [**Bailly** 2018c].*

Contents

5.1 Introduction **85**
5.1.1 State of the art 86
5.1.2 Contribution 86
5.2 Methods **87**
5.2.1 Estimated variables coupling 87
5.2.2 Measurements 88
5.2.3 Multi-source estimation of the CoM position 88
5.2.4 Multi-source estimation of the angular momentum variation quantity 90
5.2.5 Recursive estimation of the CoM position and the angular momentum variation 92
5.3 Experimental validation of the estimation framework **93**
5.3.1 Generation of ground truth and noisy measures in simulation 93
5.3.2 Application to human data 96
5.4 Discussion **98**

5.1 Introduction

The precise estimation of the CoM position and the angular momentum variation of the body is an important topic in the field of human motion analysis. It has various applications in biomechanics, medical disorder diagnosis or for the control of legged machines. The main difficulty lies in the fact that these two quantities are not directly measurable, but depend on fixed parameters (e.g. mass distribution of the body, dimensions of the limbs, etc.) as well as varying quantities (e.g. limb configurations, external forces, etc.).

5.1.1 State of the art

In order to estimate the CoM position, several methods exploiting different sources of information are commonly applied in biomechanics [Lafond 2004]. They can be grouped into two broad categories, namely *kinematic methods* which only exploit kinematic measurements and *kinetic methods* which reconstruct the CoM position from kinetic signals.

The first category is certainly the most popular one. It considers the body as a rigid poly-articulated system whose masses and joint angles can be obtained from anthropomorphic tables and MoCap systems respectively [De Leva 1996, Farley 1998]. Then, computing the CoM position boils down to a weighted average calculation accounting for the mass distribution and the position of each segment's CoM. This approach is experimentally demanding as the subject's body has to be covered with an appropriate set of reflective markers, in order to accurately estimate the limb positions. It is also worth noticing that kinematic methods are subject to noises of various types stemming from soft tissue artifacts [Cappozzo 1996, De Rosario 2012], the statistical character of anthropometric tables, MoCap systems and the applied methodology itself [Baker 2006].

For the kinetic methods, estimation of the CoM position is achieved by measuring either the CoP or the contact forces from force plate signals. For instance, if the body is modeled as an inverted pendulum, the CoM position can be estimated from the mechanical relationship between the CoM and the CoP [Morasso 1999]. This approach then assumes that the CoM trajectory can be associated to the oscillations of an inverted pendulum, and the acceptable range of motion of such a method is mostly limited to balance assessments. [Caron 1997] have proposed to filter the CoP trajectory with a low-pass filter to estimate the horizontal components of the CoM. Once again, the accuracy of this approach is limited to slow movements. Finally, by assuming a constant-height CoM, performing a double integration of external forces together with an estimation of the angular momentum rate expressed at the CoM, [Shimba 1984b] and [Levin 1996] have provided another way to estimate the horizontal components of the CoM.

Concerning the estimation of the angular momentum rate of change, to the best of our knowledge, only kinematic estimation has been performed [Dapena 1978, Bruijn 2008], although kinetic data can also be used as suggested in [Herr 2008b].

In [Carpentier 2016a], a complementary filter in the spectral domain was used to merge kinematic and kinetic data in order to estimate the CoM position, by assuming that angular momentum variations were negligible.

5.1.2 Contribution

In this work, we propose a generic framework to simultaneously and accurately estimate the CoM position together with the angular momentum variation by exploiting the intrinsic properties that link both quantities. This work extends the approach in [Carpentier 2016a] by also estimating the variations of angular

momentum which leads, as we show thereafter, to a better estimation of the CoM quantity. In addition, we exploit a recursive strategy in order to improve the estimate of the CoM trajectory from the angular momentum trajectory and vice-versa. The consistency of the proposed approach is validated in simulation, by assessing the accuracy of our estimated quantities against ground truth data. Finally, our estimation framework is applied to the analysis of a human walking motion in order to illustrate the efficiency of our approach on real data.

5.2 Methods

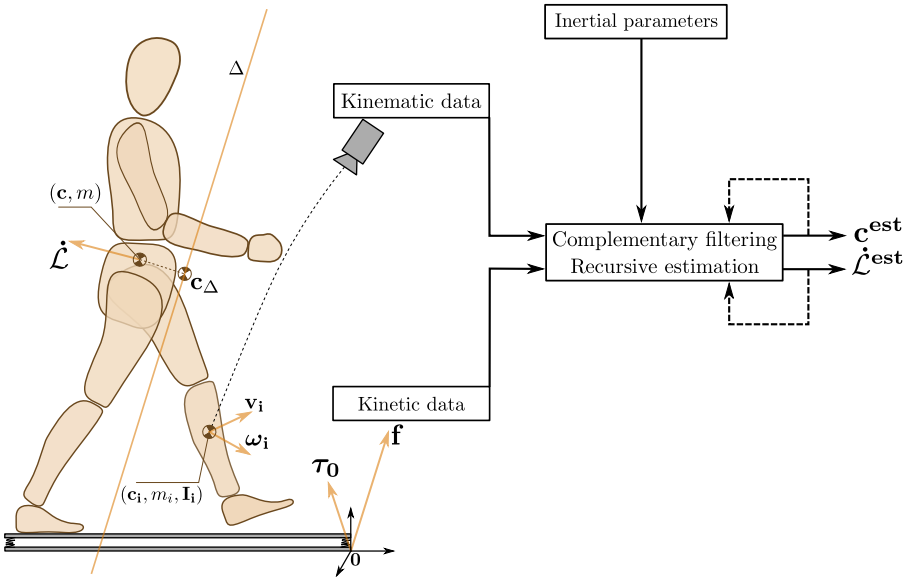

Figure 5.1: Illustration of the measurement apparatus. The several physical quantities involved in the estimation framework are displayed, as well as a simplified sketch of the estimation framework.

This section recalls how the position of the CoM (denoted by $\mathbf{c}$) and the angular momentum variation expressed at the CoM (denoted by $\dot{\mathcal{L}}_\mathbf{c}$) are linked together through the wrench of external forces. Then, we identify the different sources of information which contribute to the estimation of $\dot{\mathcal{L}}_\mathbf{c}$ and $\mathbf{c}$, and we explain how to efficiently fuse them by exploiting their level of accuracy in the spectral domain.

5.2.1 Estimated variables coupling

Let m be the mass of the body, and $\mathbf{c}$, $\dot{\mathbf{c}}$ and $\ddot{\mathbf{c}}$ its CoM position, velocity and acceleration. Let $\mathbf{f_i}$ be the ith contact force applied to the system at the contact point $\mathbf{p_i}$. The external actions exerted on the system by the environment can be described by the resulting wrench of contact forces, $\mathbf{f}$, and moments, $\boldsymbol{\tau_0}$, expressed

at the origin $\mathbf{0}$:

$$\mathbf{f} = \sum_i \mathbf{f_i}, \tag{5.1a}$$

$$\boldsymbol{\tau_0} = \sum_i \mathbf{p_i} \times \mathbf{f_i} \tag{5.1b}$$

This wrench can then be expressed at any other point of the space using the Varignon formula. It follows that the wrench of external forces at the CoM is given by:

$$\boldsymbol{\tau_c} = \boldsymbol{\tau_0} + \mathbf{f} \times \mathbf{c} \tag{5.2}$$

According to the Euler equation of motion, the angular momentum variation at the CoM is equal to the moment of the external action expressed at the CoM:

$$\dot{\mathcal{L}}_\mathbf{c} = \boldsymbol{\tau_0} + \mathbf{f} \times \mathbf{c} \tag{5.3}$$

Eq. (5.3) provides the coupling between the two quantities we want to estimate, namely the CoM position and the angular momentum variation.

5.2.2 Measurements

In order to use our estimation framework, one must know the total mass m of the subject and the gravitational acceleration $\mathbf{g} = [0, 0, -g]^T$, with g the standard gravity value. These are rather reasonable assumptions since the mass is easily measurable from force plates in standing position and the gravity is precisely known. Using a complete MoCap system associated to a 6D force measurement unit, one can measure kinematic and kinetic data related to the physical quantity we aim to estimate:

- the resulting wrench of contact ($\mathbf{f}$ and $\boldsymbol{\tau}_0$) expressed at the origin, via force sensors (force plates, embedded sensors, etc.);
- the position of the CoM, denoted by $\mathbf{c^{mocap}}$, deduced from the MoCap and the mass distribution of the subject;
- the angular momentum at the CoM, denoted by $\mathcal{L}_\mathbf{c}^\mathbf{mocap}$, which can be obtained from the angular velocities and the inertias of the segments.

5.2.3 Multi-source estimation of the CoM position

This section explains how to compute and process the three different input signals that carry information about the position of the CoM. The spectral accuracy of each signal is depicted in Fig. 5.2.

5.2.3.1 From kinetic data

The second law of Newton states that:

$$\ddot{\mathbf{c}} = \frac{\mathbf{f}}{m} + \mathbf{g}. \tag{5.4}$$

By double integration of the right-hand side of this equation one can estimate the CoM position thanks to the information provided by the force platform data. Let us denote this estimation by $\mathbf{c}^{\mathbf{force}}$. However without the knowledge of integration constants, a quadratic drift, which is visible in low and medium frequencies, is present and disturbs the estimation.

5.2.3.2 From kinematic data

Reflective markers' position combined with anthropomorphic data are usually used to retrieve the CoM position. Let us denote this estimation by $\mathbf{c}^{\mathbf{mocap}}$. Note that it mainly suffers from biases due to the modeling errors of mass distribution. It is also subject to the high frequency sensor noise due to the MoCap technology. Then, the error between this signal and the real position of the CoM mostly lies in low and high frequency domains.

5.2.3.3 From the central axis of contact wrench

Considering the contact moment field, there exists one unique axis called the central axis of contact wrench and denoted by Δ [Dimentberg 1968], where the moment of contact forces is collinear to $\mathbf{f}$. The projection $\mathbf{c}_{\boldsymbol{\Delta}}$ of the CoM $\mathbf{c}$ onto Δ is given by:

$$\mathbf{c}_{\boldsymbol{\Delta}} = \frac{\mathbf{f} \times \boldsymbol{\tau}_0 + (\mathbf{c} \cdot \mathbf{f})\mathbf{f}}{\|\mathbf{f}\|^2}. \tag{5.5}$$

This quantity can be computed thanks to the force and moment signals provided by the force plates and the kinematic reconstruction of the CoM $\mathbf{c}_{\mathbf{mocap}}$ as follows:

$$\mathbf{c}_{\boldsymbol{\Delta}} = \underbrace{\frac{\mathbf{f} \times \boldsymbol{\tau}_0}{\|\mathbf{f}\|^2}}_{\text{Force plates data}} + \underbrace{(\mathbf{c}^{\mathbf{mocap}} \cdot \mathbf{n})\mathbf{n},}_{\text{Force plates, MoCap data and mass distribution}} \tag{5.6}$$

where $\mathbf{n}$ is the direction cosine of $\mathbf{f}$. Besides, knowing $\dot{\mathcal{L}}_{\mathbf{c}}$ and $\mathbf{f}$, the difference between $\mathbf{c}$ and $\mathbf{c}_{\boldsymbol{\Delta}}$ can be computed as:

$$\mathbf{c} - \mathbf{c}_{\boldsymbol{\Delta}} = \underbrace{\frac{\dot{\mathcal{L}}_{\mathbf{c}} \times \mathbf{f}}{\|\mathbf{f}\|^2}}_{\text{Force plates, MoCap data and inertias}}. \tag{5.7}$$

This leads to a third estimate of the CoM position that will be denoted by $\mathbf{c}^{\mathbf{axis}}$

and expressed as:

$$\mathbf{c}^{\mathbf{axis}} = \mathbf{c}_{\boldsymbol{\Delta}} + \frac{\dot{\mathcal{L}}_{\mathbf{c}} \times \mathbf{f}}{\|\mathbf{f}\|^2}, \tag{5.8a}$$

$$\mathbf{c}^{\mathbf{axis}} = \frac{\mathbf{f} \times \boldsymbol{\tau}_0}{\|\mathbf{f}\|^2} + (\mathbf{c}^{\mathbf{mocap}} \cdot \mathbf{n})\mathbf{n} + \frac{\dot{\mathcal{L}}_{\mathbf{c}} \times \mathbf{f}}{\|\mathbf{f}\|^2}. \tag{5.8b}$$

5.2.3.4 Complementary filter of the CoM

Similarly to [Carpentier 2016a], we use a complementary filtering approach [Higgins 1975] to fuse these three signals ($\mathbf{c}^{\mathbf{force}}$, $\mathbf{c}^{\mathbf{mocap}}$ and $\mathbf{c}^{\mathbf{axis}}$) in order to retrieve an accurate estimate of the CoM position. The main idea of this filter is to exploit the accuracy of the different signals in the spectral domain. Indeed, each of these signals conveys a certain level noise, but these noises do not have the same spectral distribution. This property is exploited to design the complementary filter on the CoM estimates.

The theory of complementary filtering provides a way to make these three different sources contribute to the estimation of the CoM position by taking profit from the information about the spectral distribution of noise they suffer from. In the Laplace domain, 3 complementary filters are designed (high-pass, band-pass and low-pass filters, see Fig. 5.3), so that their transfer functions sum to 1. The sum of these filters maintains the energy of the signal with zero phase modification [Higgins 1975].

5.2.4 Multi-source estimation of the angular momentum variation quantity

In this section, we present how to compute and process the two input signals that permit to estimate the value of $\dot{\mathcal{L}}_{\mathbf{c}}$. More precisely, we show how an estimate of the angular momentum quantity can be built from kinematic and kinetic signals (see Fig. 5.2).

5.2.4.1 From kinematic data

The time derivative of reflective markers positions combined with statistical anthropomorphic inertia matrices are usually used to compute the angular momentum of the human body by exploiting the following relation:

$$\mathcal{L}_{\mathbf{c}}^{\mathbf{mocap}} = \sum_i \mathbf{I_i}\boldsymbol{\omega}_i + \overrightarrow{\mathbf{cc_i}} \times m_i \mathbf{v_i}, \tag{5.9}$$

where $\mathbf{I_i}$, $\boldsymbol{\omega}_i$, $\mathbf{c_i}$, m_i and $\mathbf{v_i}$ are the moment of inertia, angular velocity, CoM position, mass and relative velocity of the ith body respectively. Taking the derivative of this quantity provides an estimation of $\dot{\mathcal{L}}_c$ from this first source of information at the price of amplifying high-frequency noise. The modeling error of mass and

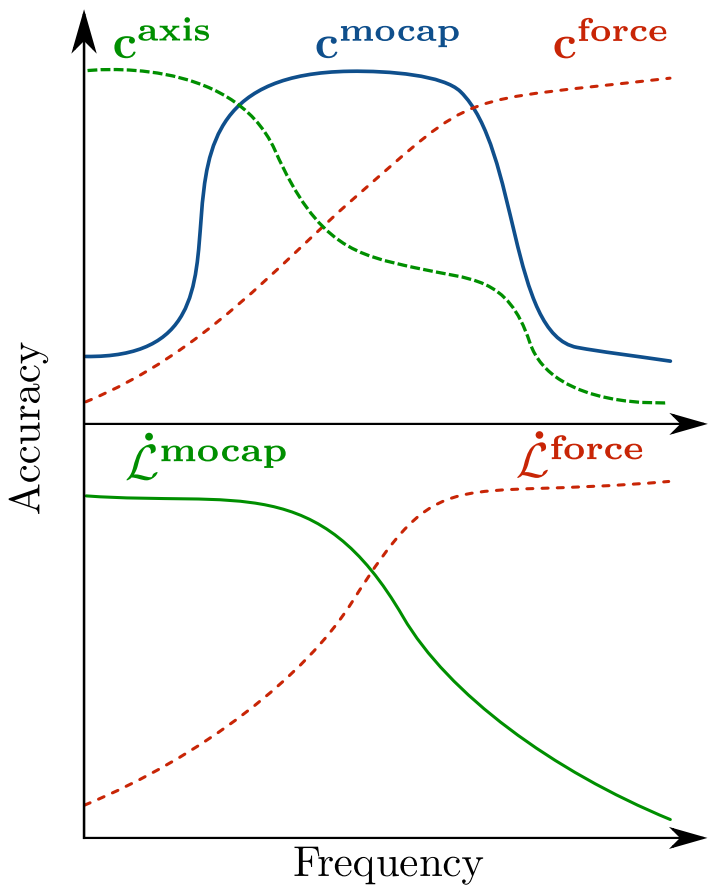

Figure 5.2: Schematic representation of the spectral accuracy of the different input signals involved in the estimation of $\mathbf{c}$ and $\dot{\mathcal{L}}_{\mathbf{c}}$.

inertias distribution produces a bias on the estimation of $\mathcal{L}_{\mathbf{c}}$. Theoretically, this bias depends on the posture of the body but in practice, as this posture remains fairly constant during most locomotor tasks, the bias can be considered constant. Hence, by taking the derivative of $\mathcal{L}_{\mathbf{c}}^{\mathbf{mocap}}$, this measurement can be trusted in the low frequency domain.

5.2.4.2 From the moment field properties

The second source of information for the estimation of $\dot{\mathcal{L}}_{\mathbf{c}}$, lies in Eq. (5.3):

$$\dot{\mathcal{L}}_{\mathbf{c}}^{\mathbf{force}} = \boldsymbol{\tau}^0 + \mathbf{f} \times \mathbf{c}, \tag{5.10}$$

and is provided by force plates measurements with an estimation of $\mathbf{c}$.

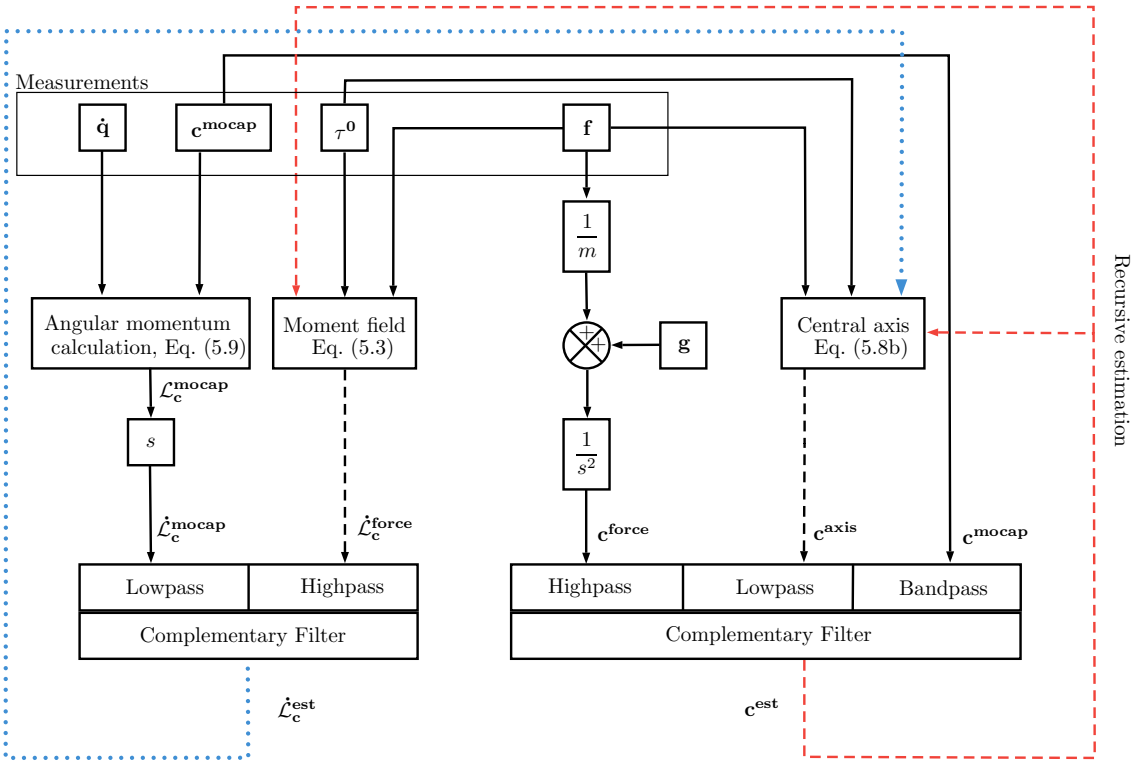

Figure 5.3: Flow chart for the recursive complementary estimation framework. s is the Laplace variable. Dotted lines represent the update step of the algorithm. Complementary filtered components are summed up in order to output $\dot{\mathcal{L}}_{\mathbf{c}}^{\mathbf{est}}$ and $\mathbf{c}^{\mathbf{est}}$, estimates of $\dot{\mathcal{L}}_{\mathbf{c}}$ and $\mathbf{c}$ respectively.

5.2.4.3 Complementary filter for the angular momentum variation quantity

In the same way as before, complementary filtering is used to add both contributions to the estimation of $\dot{\mathcal{L}}_{\mathbf{c}}$. In the Laplace domain, two complementary filters are designed (high-pass and low-pass filters, see Fig. 5.3) such that their transfer functions sum to 1.

5.2.5 Recursive estimation of the CoM position and the angular momentum variation

Our recursive approach is motivated by the fact that the estimation of $\dot{\mathcal{L}}_{\mathbf{c}}^{\mathbf{force}}$ depends on an estimation of $\mathbf{c}$ (see Eq. (5.10)) and that the estimation of $\mathbf{c}_{\mathbf{axis}}$ depends on an estimation of $\dot{\mathcal{L}}_{\mathbf{c}}$ (see Eq. (5.8b)). Hence, the estimation of $\mathbf{c}$ can be refined by refining the estimation of $\dot{\mathcal{L}}_{\mathbf{c}}$, and vice versa. In Fig. 5.3, a detailed diagram of the proposed estimation framework is displayed.

5.3 Experimental validation of the estimation framework

In this section, the efficiency of the estimation framework was first demonstrated by its application on simulated data. Then experimental data were processed to illustrate the performance of the proposed method on a real application scenario. In both cases, the estimation was performed recursively as sketched in Fig. 5.3.

5.3.1 Generation of ground truth and noisy measures in simulation

In this subsection, we present the simulation of dynamically consistent walking data for an avatar. Then, by adding noise to the several quantities involved in the estimation framework we show that it is possible to compare our estimation to ground truth data.

5.3.1.1 Methods

The simulated avatar consisted of a simplified humanoid model endowed with 36 degrees of freedom. The simulated motion was a walking task on horizontal ground at 0.5 m/s using the dynamically consistent approach introduced in [Carpentier 2016b]. Ground truth kinetic data were computed at $200Hz$ using the modeling software Pinocchio which includes rigid body dynamics algorithms for poly-articulated systems [Carpentier 2017c]. Band-limited centered white noise was added to each signal, in accordance with our analysis of the noise spectral density. The low, medium and high frequency domains were delimited from 0 to 4 Hz, 16 to 24 Hz and 92 to 100 Hz respectively. The standard deviations of the noise were 1 N and 1 Nm in the low and medium frequency domains for the force and moment measurements respectively, 0.1 N and 0.1 Nm in the high frequency domain for $\mathbf{c}^{\mathbf{mocap}}$ and $\dot{\mathcal{L}}_{\mathbf{c}}^{\mathbf{mocap}}$ respectively, in order to replicate the errors due to the motion capture technology. Inertial data (mass, CoM position and inertia matrix) of each segment was randomly biased in order to simulate the error due to anthropometric tables (multiplicative random value following a 1-centered normal distribution with a standard deviation of 1). The cut-off frequencies were 1 Hz and 25 Hz for the low-pass and high-pass second order filters of $\mathbf{c}^{\mathbf{est}}$ respectively. The band-pass filter was deduced by complementarity. The cut-off frequency for the low pass filter of $\dot{\mathcal{L}}_{\mathbf{c}}^{\mathbf{est}}$ was 2 Hz, the high-pass filter was deduced by complementarity too.

5.3.1.2 Results

The estimation procedure was initialized with the value of $\mathbf{c}^{\mathbf{mocap}}$ before filtering, because it is the best guess one can make before adding further data. The recursion was stopped when the difference between the values of the last estimates of $\dot{\mathcal{L}}_{\mathbf{c}}$ and $\mathbf{c}$ and the current ones were below 10^{-3}. Fig. 5.4 depicts the error of $\mathbf{c}^{\mathbf{mocap}}$, $\mathbf{c}^{\mathbf{axis}}$ and $\mathbf{c}^{\mathbf{est}}$ integrated over the whole trajectory and normalized with regard to the error of $\mathbf{c}^{\mathbf{mocap}}$. This result shows how the complementary filter improves the initial

guess $\mathbf{c}^{\mathbf{mocap}}$ by reducing the norm of the error with regard to the ground-truth values (which are exactly known in simulation).

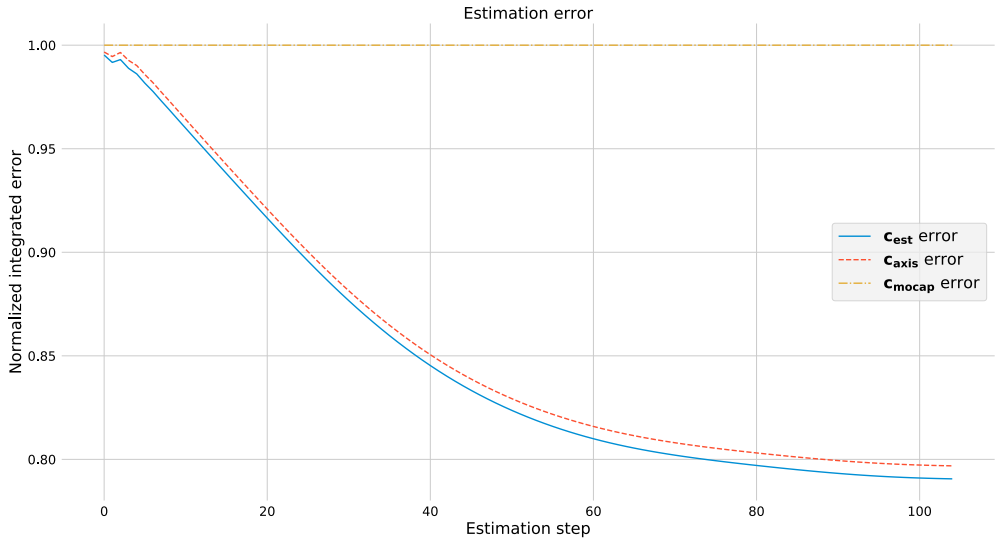

Figure 5.4: Norm of the error integrated over the whole trajectory for the different estimates of $\mathbf{c}$ in simulation, as a function of estimation steps.

In more details, Fig. 5.5 shows the 3 components of $\mathbf{c}$ and of $\dot{\mathcal{L}}_{\mathbf{c}}$ for the different estimates, in addition to the real values of the simulation, without noise. On the second row of Fig. 5.5, $\mathbf{c}^{\mathbf{mocap}}$ unfiltered is displayed, to exhibit the improvement provided by our method. A low frequency bias between $\mathbf{c}^{\mathbf{mocap}}$ unfiltered and the ground truth value is noticeable, in particular on the y and z components because of the scale of the plots. This bias comes from the error on the inertial parameters that we purposely introduced in the simulated data. Fig. 5.5 also shows that the final estimation $\mathbf{c}^{\mathbf{est}}$ is better than the initial guess, as corroborated by the error analysis in Fig. 5.4. For instance, on the vertical axis, the average absolute error of the MoCap estimate is of 3.6 cm, whereas it is reduced to 1.1 cm for the final estimate. On the Y axis the average absolute error is reduced from 2.1 cm to 2.9 mm by the presented framework. On the X axis, which is the main direction of locomotion, no significant improvement is measured: the average absolute error remains close to 6 mm. This overall improvement is also noticeable on the third row of Fig. 5.5 where the low frequency of the norm of the error of $\mathbf{c}^{\mathbf{est}}$ is reduced, with regard to $\mathbf{c}^{\mathbf{mocap}}$ unfiltered. The contribution of $\mathbf{c}^{\mathbf{force}}$ in the high frequency domain was quasi zero, because the simulated motion was smooth, and thus the trajectory of $\mathbf{c}$ was limited to low and medium frequency components. On the fourth raw of Fig. 5.5, the estimation of $\dot{\mathcal{L}}_{\mathbf{c}}$ is displayed, and the result is in accordance with the true value, with overshooting up to 100%.

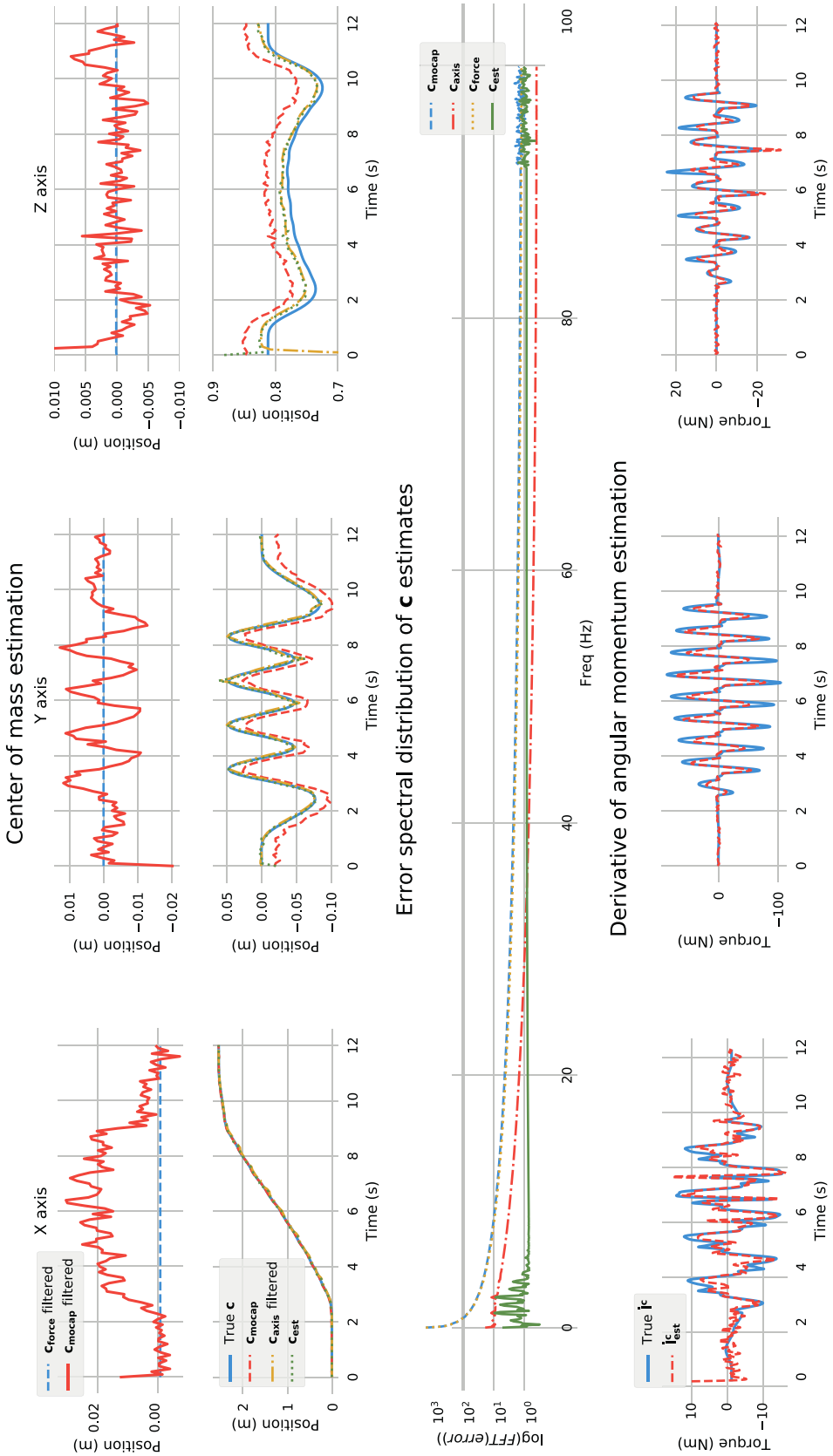

Figure 5.5: Different contributions to the estimates of $\mathbf{c}$ and $\dot{\mathcal{L}}_{\mathbf{c}}$ in simulation. First row: $\mathbf{c}^{\mathbf{force}}$ high-pass filtered, $\mathbf{c}^{\mathbf{mocap}}$ band-pass filtered. Second row: true $\mathbf{c}$, $\mathbf{c}^{\mathbf{mocap}}$, $\mathbf{c}^{\mathbf{axis}}$ low-pass filtered and $\mathbf{c}^{\mathbf{est}}$. Third row: Logarithm of the norm of the FFT of the error for the different estimates. Fourth row: $\dot{\mathcal{L}}^{\mathbf{est}}_{\mathbf{c}}$ and $\dot{\mathcal{L}}_{\mathbf{c}}$.

5.3.2 Application to human data

In this second subsection, we present how the estimation framework was applied to real kinematic and kinetic data obtained during human walking experiments, in order to retrieve the estimates of $\mathbf{c}$ and $\dot{\mathcal{L}}_{\mathbf{c}}$.

5.3.2.1 Methods

One male participant (age: 23 y, mass: 64 kg, height: 1.81 m) volunteered for this study and signed an informed written consent. Experiments were conducted in accordance with the standards of the Declaration of Helsinki (rev. 2013) and approved by a local ethic evaluation committee. The participant was asked to freely walk across the two force plates at a comfortable walking speed. Whole-body 3D kinematic data were collected by 13 infra-red cameras sampling at 200 Hz, that recorded the motion of 43 reflective markers placed on the subject, following the [Wu 2002b, Wu 2005a] and [Dumas 2007] recommendations. A whole-body 3D model including 42 degrees of freedom for 15 segments was used to reconstruct the movements of the walker. Two force plates embedded into the floor were used to record ground reaction forces at 1 kHz. Inertial parameters were computed thanks to anthropomorphic tables [Dumas 2007], resulting in the computation of $\mathbf{c}^{\mathbf{mocap}}$ and $\mathcal{L}_{\mathbf{c}}^{\mathbf{mocap}}$, see Fig. 5.3.

5.3.2.2 Results

Fig. 5.6 displays a variety of curves relative to the estimation of $\mathbf{c}$ and $\dot{\mathcal{L}}_{\mathbf{c}}$ for a human walking on horizontal ground.

Firstly, one can notice that the CoM position profiles were slightly different from the simulated ones, presented in section 5.3.1, especially for the vertical component. This is due to the reduced number of degrees of freedom of the simulation avatar and to the motion in simulation which was designed to keep the humanoid closed to a half sitting position while walking, in order to avoid joint limits that leads to kinematic singularities. In the case of human data experiment, there was no ground truth values available to assess the quality of the estimation. On the second row of Fig. 5.6, the average absolute differences between the final estimates and $\mathbf{c}^{\mathbf{mocap}}$ unfiltered are of $3,1$ cm, 3.5 mm and 5 mm on the X, Y and Z axes, respectively. These error values are consistent with the improvement towards the ground-truth values which were computed in simulation. This result suggests two remarks: the levels of noise introduced in simulation were realistic and the differences observed on real data after recursion correspond to an improvement in the estimate. Indeed, the low frequency contribution of $\mathbf{c}^{\mathbf{axis}}$ seems to compensate for the low frequency drift of $\mathbf{c}^{\mathbf{mocap}}$ band-pass filtered and, as noticed in simulation, it also provides a low frequency correction of the initial guess $\mathbf{c}^{\mathbf{mocap}}$. On the second raw of Fig. 5.6, the estimation of $\dot{\mathcal{L}}_{\mathbf{c}}$ is rather noisy, but the values of the estimates are consistent with the dynamic of the motion and the weight of the participant.

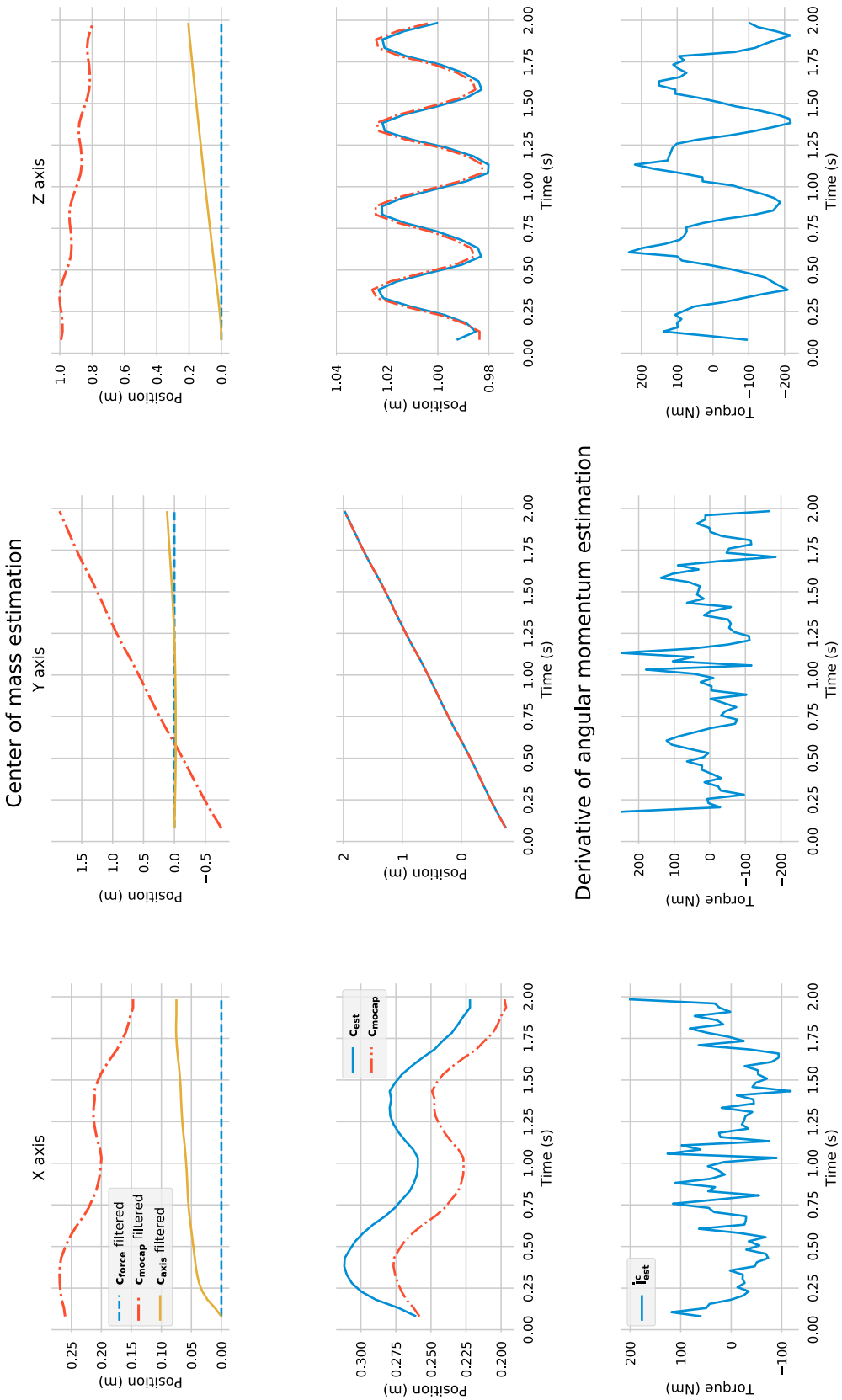

Figure 5.6: Different contributions to the estimates of $\mathbf{c}$ and $\dot{\mathcal{L}}_{\mathbf{c}}$ on human recorded data. First row: $\mathbf{c}^{\mathbf{force}}$ high-pass filtered, $\mathbf{c}^{\mathbf{mocap}}$ band-pass filtered and $\mathbf{c}^{\mathbf{axis}}$ low-pass filtered. Second row: $\mathbf{c}^{\mathbf{est}}$ and $\mathbf{c}^{\mathbf{mocap}}$. Third row: $\dot{\mathcal{L}}_{\mathbf{c}}^{\mathbf{est}}$.

5.4 Discussion

In this study, we proposed a method to simultaneously estimate the CoM position and the variation of angular momentum expressed at the CoM by complementary filtering of kinematic and kinetic data, in order to get the best of both worlds. Unlike previous works, our estimation framework does not rely on any simplifying assumption, such as the negligible angular momentum variations hypothesis [Carpentier 2016a], or the coplanarity of the contact surfaces [Levin 1996, Morasso 1999].

The quality of the estimation provided by this approach could be of interest in the fields of human and animal motion analysis [Minetti 2011], sports biomechanics [Maldonado 2017], and, generally speaking, in every research area that requires to estimate such quantities.

In simulation, the results showed that the proposed framework enabled us to reduce the norm of the error between the estimation of the CoM position and its real value, when compared to kinematic estimation alone. This reduction was a direct consequence of the exploitation of the spectral properties of each measurement. More precisely, this improvement was mainly due to a low frequency bias correction brought by a better estimation of the angular momentum variation, and exploited in the geometrical link between the CoM position and the central axis of contact forces.

The application of the method to human walking data also provided a difference between the raw estimation coming from the MoCap alone and the complementary estimation at a low frequency level. Although one cannot compare the quality of these two estimates on real data, results in simulation suggest that the low frequency correction was an improvement in favor of the complementary estimation. Results in simulation showed that the estimation of the derivative of the angular momentum was not perfect, and this is one explanation to the small bias that remained on the estimation of the CoM position after convergence of the algorithm. The final user would only have to adjust the cutting frequencies inside the complementary filters if needed, which may depend on the nature of the recorded motion. The overall estimation could be enhanced by improving the estimation of the angular momentum variation which is shown, via a different method, in the next chapter.

Finally, it is important to notice that our framework is not limited to biomechanics, as it can be exploited directly in robotics in order to estimate linear and angular momenta, which are the two critical quantities for the balance of legged robots [Orin 2013].

Chapter 6

State estimation for systems in contact

Using Differential Dynamic Programming for optimal centroidal state estimation

---

Contents

6.1 Introduction **101**
6.2 State of the system and motivations **102**
6.3 System's state observation **103**
6.4 Estimating the state **104**
6.4.1 State transition and observation equations 104
6.4.2 Problem formulation 104
6.4.3 The DDP algorithm 108
6.5 Illustration **109**
6.6 Perspectives **110**

6.1 Introduction

Although the methodology presented in Chap. 5 involves elaborated spectral data fusion as well as recursive refining of the centroidal state estimation, it remains local. Indeed, the computation of each sample of the estimated state depends on a number of measurement samples equal to the order of the numerical filters involved in the complementary filtering algorithm (in our case, two). This implies that there is no global consideration of the state trajectory although a local change in the state of the system spreads throughout time because of the dynamic consistency of the estimation. Among the consequences of this limitation, estimating the initial conditions of the system cannot be handled properly. To overcome this issue, the estimation process must include a global time preview that models how locally changing the estimated state will impact the estimated trajectory. This is typically what is provided by the Differential Dynamic Programming (DDP) algorithm, classically used for control [Tassa 2014].

In the sequel, DDP is applied to estimating the centroidal dynamics of a system in contact. With regard to the estimation framework presented in Chap. 5, the

state of the system is extended as it also contains the linear momentum of the whole body and its derivative as well as the angular momentum. First, the problem is formulated as the maximization of a likelihood function over a temporal horizon as in [Kobilarov 2015]. To this end, the dynamics of the centroid is modeled with Gaussian priors on the derivatives of the linear and angular momenta, which are unknown. Then, the likelihood function is maximized over the state and the unknown dynamics using the DDP algorithm.

6.2 State of the system and motivations

The dynamic equations of the system were already introduced in Sec. 5.2. Let us recall the equations of the angular momentum and its derivative:

$$\mathbf{p} = m\dot{\mathbf{c}}, \tag{6.1}$$

$$\dot{\mathbf{p}} = \mathbf{f}. \tag{6.2}$$

The state of the system is:

$$\mathbf{x} = \begin{bmatrix} \mathbf{c} \\ \mathbf{p} \\ \dot{\mathbf{p}} \\ \mathcal{L}_{\mathbf{c}} \\ \dot{\mathcal{L}}_{\mathbf{c}} \end{bmatrix}. \tag{6.3}$$

This state vector contains the centroidal dynamics of the system. This notion was formalized in [Orin 2013], where it is presented as the dynamics of the system projected at its CoM. The term *projected* comes from the computational view of the authors according to which the derivatives of linear and angular momentum expressed at the CoM are the result of a change of basis, from the joint space, where physical interactions occur to the CoM space (for further details, see Sec. 4.2.3). One of the motivations for recasting the dynamics of the system in its CoM space comes from a fundamental principle of dynamics (Newton-Euler's laws of motion) which states that the derivatives of angular and linear momentum expressed at the CoM are equivalent to the external contact wrench, which encompasses all the external interactions of the system with its environment. In humanoid robotics, it was demonstrated that, starting with a sequence of contacts, generating locomotion can be done efficiently by finding an appropriate centroidal dynamic trajectory that satisfies the physical constraints of the problem (dynamic equation of the robot, Eq. (2.2), consistent contact model), and then finding a whole-body trajectory using second-order inverse kinematics [Carpentier 2016b]. Using this approach, the Gepetto team was able to demonstrate a versatile set of motions with the HRP-2 robot (big steps walking on flat terrain, stairs ascent and descent, multi-contact

stairs ascent using a handrail). However, one of the possible improvements of this motion generation pipeline would be to provide the pattern generator with a centroidal state feedback (which it does not have yet) for balancing purposes in case of discrepancy between the expected and the real contact sequences, external perturbations, and so on... The work presented in the sequel fits within this framework, as the chosen state (Eq. (6.3)) contains the centroidal dynamics of the robot. Because of the deep connections between legged robotics and human motion analysis (dynamic equations, type of sensors, etc.), this work on estimation follows that of Chap. 5 and can directly be used in motion analysis to gain a deeper insight into the dynamic quantities that characterize human motion.

6.3 System's state observation

The choices that are exposed hereafter, concerning the measured physical quantities for state observation, were thought in order to remain fully compatible with both humanoid robotics and biomechanics. Consequently, some possible sources of information that could be used in robotic cases of applications, such as IMUs, are not addressed in the following developments. However, they remain fully relevant as independent sources of information, and incorporating them into this formulation would not transform the approach and would be a highly relevant development. This perspective is discussed in Sec. 6.6.

The physical quantities that are supposed to be known are:

- the total mass m of the system,
- the gravitational acceleration $\mathbf{g}$.

Whether in robotics or in biomechanics, the physical quantities that can be measured are:

- the resulting wrench of contact ($\mathbf{f}$ and $\boldsymbol{\tau}_0$) via embedded force sensors (or force plates, handles, etc.),
- the position of the CoM $\mathbf{c}$ via forward kinematics (or anthropometric methods): $\mathbf{c}^{\mathbf{kyn}}$, w.r.t. an inertial frame,
- the angular momentum at the CoM $\mathcal{L}_{\mathbf{c}}$ via joint velocity and mass distributions (or anthropometric methods): $\mathcal{L}^{\mathbf{kyn}}$.

As a result, the measurement vector is:

$$\mathbf{y} = \begin{bmatrix} \mathbf{c}^{\mathbf{kyn}} \\ \boldsymbol{\tau}_{\mathbf{0}} \\ \mathbf{f} \\ \mathcal{L}^{\mathbf{kyn}} \end{bmatrix} \tag{6.4}$$

6.4 Estimating the state

6.4.1 State transition and observation equations

Let $\mathbb{0}$ and $\mathbb{1}$ be the null element and the identity of $\mathbb{R}^{3\times 3}$. The first-order Euler approximation of the state transition equations for this model are:

$$\mathbf{x}_{i+1} = \tilde{f}(\mathbf{x_i}, \boldsymbol{\omega_i}) = f(\mathbf{x_i}) + \boldsymbol{\omega_i} \tag{6.5}$$

$$= \begin{bmatrix} \mathbb{1} & \mathbb{1}\frac{T}{m} & \mathbb{1}\frac{T^2}{2m} & \mathbb{0} & \mathbb{0} \\ \mathbb{0} & \mathbb{1} & \mathbb{1}T & \mathbb{0} & \mathbb{0} \\ \mathbb{0} & \mathbb{0} & \mathbb{1} & \mathbb{0} & \mathbb{0} \\ \mathbb{0} & \mathbb{0} & \mathbb{0} & \mathbb{1} & \mathbb{1}T \\ \mathbb{0} & \mathbb{0} & \mathbb{0} & \mathbb{0} & \mathbb{1} \end{bmatrix} \mathbf{x_i} + \begin{bmatrix} \frac{T^3}{6m} & 0 \\ \frac{T^2}{2} & 0 \\ T & 0 \\ 0 & \frac{T^2}{2} \\ 0 & T \end{bmatrix} \begin{bmatrix} \boldsymbol{\omega}_i^{\dot{k}} & \boldsymbol{\omega}_i^{\dot{l}^G} \end{bmatrix}^T \tag{6.6}$$

$$\hat{=}\ A\mathbf{x_i} + B\boldsymbol{\omega_i}, \tag{6.7}$$

where $\boldsymbol{\omega}_i^{\dot{k}}$ and $\boldsymbol{\omega}_i^{\dot{l}^G}$ are random samples drawn from $\mathcal{N}(0, \Sigma_{\dot{k}}^2)$ and $\mathcal{N}(0, \Sigma_{\dot{l}}^2)$ respectively, representing unknown derivatives of the linear and angular momenta. The observation equations for this model are:

$$\hat{\mathbf{y}}_i = \tilde{g}(\mathbf{x_i}, \boldsymbol{\eta_i}) = g(\mathbf{x_i}) + \boldsymbol{\eta_i} = \begin{bmatrix} \mathbb{1} & \mathbb{0} & \mathbb{0} & \mathbb{0} & \mathbb{0} \\ \mathbb{0} & \mathbb{0} & \mathbf{c}_i\times & \mathbb{0} & \mathbb{1} \\ \mathbb{0} & \mathbb{0} & \mathbb{1} & \mathbb{0} & \mathbb{0} \\ \mathbb{0} & \mathbb{0} & \mathbb{0} & \mathbb{1} & \mathbb{0} \end{bmatrix} \mathbf{x_i} + \boldsymbol{\eta_i} \tag{6.8}$$

$$\hat{=}\ C(\mathbf{x_i})\mathbf{x_i} + \boldsymbol{\eta_i}, \tag{6.9}$$

where $\boldsymbol{\eta}_i = [\boldsymbol{\eta}_i^{kyn}, \boldsymbol{\eta}_i^{\tau}, \boldsymbol{\eta}_i^{f}, \boldsymbol{\eta}_i^{l}]^T$ are random samples drawn from $\mathcal{N}(0, \Sigma_{\eta_i}^2)$ representing noises on the measurements.

6.4.2 Problem formulation

In the following developments, let us assume that $\mathbf{x_i} \in \mathbb{R}^X$, and that $\mathbf{y_i} \in \mathbb{R}^Y$. Solving this estimation problem amounts to maximizing the likelihood $\mathcal{L}$ of the joint probability $p(\mathbf{x}, \mathbf{y})$ on a horizon of N time steps:

$$\mathcal{L}(\mathbf{x}, \mathbf{y}) = \left(p(\mathbf{x_0}) \prod_{i=1}^{N} p(\mathbf{y_i}|\mathbf{x_i}) p(\mathbf{x_i}|\mathbf{x_{i-1}}) \right), \tag{6.10}$$

$$x^* = \arg\max_x \mathcal{L}(\mathbf{x}, \mathbf{y}). \tag{6.11}$$

In other words, the optimal solution is the state trajectory $\mathbf{x}$, that most probably

outputted the measurements $\mathbf{y}$, limiting how far each state ($\mathbf{x_i}$, at step i), can be from the known dynamics of the previous one ($\mathbf{x_{i-1}}$). Given the Gaussian assumption on the jerk of the state and on the noise of the measurements, the conditional probability in (6.10) are:

$$p(\mathbf{y_i}|\mathbf{x_i}) \sim \mathcal{N}(g(\mathbf{x_i}), \Sigma_{\eta_i}), \tag{6.12a}$$

$$p(\mathbf{x_i}|\mathbf{x_{i-1}}) \sim \mathcal{N}(f(\mathbf{x_{i-1}}), \Sigma_{\omega_i}). \tag{6.12b}$$

The expected values of the probability density functions in Eqs. (6.12a) and (6.12b) represents the deterministic parts of Eqs. (6.5) and Eqs. (6.8). This implies that the random part of the dynamics is centered at zero, which is a reasonable physical assumption. Indeed, on a sufficient time horizon, a non-zero mean value of the concerned physical quantities ($\dot{\mathbf{p}}$ and $\dot{\mathcal{L}}_\mathbf{c}$) would result in a diverging dynamics of the CoM, by integration. Injecting (6.12) into (6.10) yields:

$$\mathcal{L}(\mathbf{x}, \mathbf{z}) \propto \exp[-\frac{1}{2}(\mathbf{x_0} - \hat{\mathbf{x}}_\mathbf{0})^T \Sigma_{\mathbf{x_0}}^{-1}(\mathbf{x_0} - \hat{\mathbf{x}}_\mathbf{0})] \times \prod_{i=1}^{N} \exp[-\frac{1}{2}(\mathbf{y_i} - g(\mathbf{x_i}))^T \Sigma_{\eta_\mathbf{i}}^{-1}(\mathbf{y_i} - g(\mathbf{x_i}))]$$
$$\exp[-\frac{1}{2}(\mathbf{x_i} - f(\mathbf{x_{i-1}}))^T \Sigma_{\eta_\mathbf{i}}^{-1}(\mathbf{x_i} - f(\mathbf{x_{i-1}}))].$$

Taking the negative natural log of this expression changes our maximization problem into an equivalent minimization one. But first let us recall that $\mathbf{x_i} - f(\mathbf{x_{i-1}}) = \boldsymbol{\omega_i}$ (see Eq. (6.12b)):

$$\begin{aligned} -\log(\mathcal{L}(\mathbf{x}, \mathbf{z})) &\propto \frac{1}{2}\left[||\mathbf{x_0} - \hat{\mathbf{x}}_\mathbf{0}||^2_{\Sigma_{\mathbf{x_0}}^{-1}} + \sum_{i=1}^{N} ||\boldsymbol{\omega}_i||^2_{\Sigma_{\boldsymbol{\omega_i}}^{-1}} + ||g(\mathbf{x_i}) - \mathbf{y_i}||^2_{\Sigma_{\boldsymbol{\eta_i}}^{-1}}\right], \\ &\hat{=} \frac{1}{2}||\mathbf{x_0} - \hat{\mathbf{x}}_\mathbf{0}||^2_{\Sigma_{\mathbf{x_0}}^{-1}} + \sum_{i=1}^{N} L_i(\mathbf{x_i}, \boldsymbol{\omega_i}). \end{aligned} \tag{6.13}$$

For the record, f is linear while g is bilinear in $\mathbf{x}_i$. In the running cost $L_i(\mathbf{x_i}, \boldsymbol{\omega_i})$, the two different contributions that were already discussed can be found. $||\boldsymbol{\omega}_i||^2_{\Sigma_{\boldsymbol{\omega_i}}^{-1}}$ is the cost which limits the norm of the random part of the dynamics. $||g(\mathbf{x_i}) - \mathbf{y_i}||^2_{\Sigma_{\boldsymbol{\eta_i}}^{-1}}$ is the cost which limits the discrepancy between the prediction and the measurements. These costs imply a tuning flexibility for the end user, contained in the covariation matrices $\Sigma_{\boldsymbol{\omega_i}}$ and $\Sigma_{\boldsymbol{\eta_i}}$. They enable to specify the trust that one has on the quality of a measurement with regard to another as well as the relative penalty to apply on the norm of the unknown dynamics with regard to the one applied on the measurement discrepancy.

Starting from this point, this estimation problem can be viewed as an equivalent control problem. The system's dynamics is driven by the unknown dynamics $\boldsymbol{\omega_i}$, and the measurements are kind of viewpoints that must be outputted at best by

the optimal trajectory, through function g (see Eq. (6.8)). This problem can be solved using DDP, by defining the cost-to-go from state $\mathbf{x}_i$ given that the unknown dynamics $\boldsymbol{\omega_i}$ is applied:

$$J_i(\mathbf{x_i}, \boldsymbol{\omega_i}) = \sum_{k=i}^{N} L_k(\mathbf{x_k}, \boldsymbol{\omega_k}).$$

The optimal value function at time i is denoted by $\mathcal{V}_i$ and defined according to:

$$\mathcal{V}_i(\mathbf{x_i}, \boldsymbol{\omega_i}) = \min_{\boldsymbol{\omega}_i} \; J_i(\mathbf{x_i}, \boldsymbol{\omega_i})$$

Recursively, through Hamilton-Jacobi-Belman equation, in can be expressed as:

$$\mathcal{V}_i(\mathbf{x_i}, \boldsymbol{\omega_i}) = \min_{\boldsymbol{\omega_i}}(L_i(\mathbf{x_i}, \boldsymbol{\omega_i}) + \mathcal{V}_{i+1}(f(\mathbf{x_i}, \boldsymbol{\omega_i}))$$

Let Q_i denote the unoptimized value function given by:

$$Q_i(\mathbf{x_i}, \boldsymbol{\omega_i}) = L_i(\mathbf{x_i}, \boldsymbol{\omega_i}) + \mathcal{V}_{i+1}(f(\mathbf{x_i}, \boldsymbol{\omega_i})),$$

in DDP, a second order approximation of this function is performed, in order to compute a cost change accordingly:

$$\Delta Q_i = Q_i(\mathbf{x_i} + \delta\mathbf{x_i}, \boldsymbol{\omega_i} + \delta\boldsymbol{\omega_i}) - Q_i(\mathbf{x_i}, \boldsymbol{\omega_i}) \approx$$
$$\frac{1}{2}\begin{bmatrix} 1 \\ \delta\mathbf{x_i} \\ \delta\boldsymbol{\omega_i} \end{bmatrix}^T \begin{bmatrix} 0 & \nabla_{\mathbf{x_i}} Q_i^T & \nabla_{\boldsymbol{\omega_i}} Q_i^T \\ \nabla_{\mathbf{x_i}} Q_i & \nabla^2_{\mathbf{x_i}} Q_i^T & \nabla_{\mathbf{x_i}\boldsymbol{\omega_i}} Q_i^T \\ \nabla_{\boldsymbol{\omega_i}} Q_i & \nabla_{\boldsymbol{\omega_i}\mathbf{x_i}} Q_i^T & \nabla^2_{\boldsymbol{\omega_i}} Q_i^T \end{bmatrix} \begin{bmatrix} 1 \\ \delta\mathbf{x_i} \\ \delta\boldsymbol{\omega_i} \end{bmatrix}$$

The optimal change $\delta\boldsymbol{\omega_i^*}$ for this quadratic approximation of $Q_i(\mathbf{x_i}, \boldsymbol{\omega_i})$ is:

$$\begin{aligned} \delta\boldsymbol{\omega_i^*} &= -\nabla^2_{\boldsymbol{\omega_i}} Q_i^{-1} \nabla_{\mathbf{x_i}\boldsymbol{\omega_i}} Q_i \cdot \delta\mathbf{x_i} - \alpha_i \nabla^2_{\boldsymbol{\omega_i}} Q_i^{-1} \nabla_{\boldsymbol{\omega_i}} Q_i \\ \delta\boldsymbol{\omega_i^*} &= -K_i \delta\mathbf{x_i} - \alpha k_i \end{aligned}$$

So we need to compute the several partial derivatives of Q_i.

$$\begin{aligned} \bullet \nabla_{\mathbf{x_i}} Q_i \mathrel{\hat{=}} Q_{xi} &= \nabla_{\mathbf{x_i}} L_i + \nabla_{\mathbf{x_i}} \mathcal{V}_{i+1}(f(\mathbf{x_i}, \boldsymbol{\omega_i})) \\ &= 2\tilde{C}(\mathbf{x_i})^T \Sigma^{-1}_{\boldsymbol{\eta_i}}(g(\mathbf{x_i}) - \mathbf{y_i}) + A^T \mathcal{V}'_x, \end{aligned}$$

where $\mathcal{V}'_x$ is computed backwards recursively and corresponds to the derivative of $\mathcal{V}_{i+1}$ wrt $\mathbf{x}$.

Proof:

$$\nabla_{\mathbf{x_i}} L_i = 2\frac{\partial ||g(\mathbf{x_i}) - \mathbf{y_i}||^2_{\Sigma^{-1}_{\boldsymbol{\eta_i}}}}{\partial \mathbf{x_i}} = 2\frac{\partial (g(\mathbf{x_i}) - \mathbf{y_i})^T}{\partial \mathbf{x_i}} \Sigma^{-1}_{\boldsymbol{\eta_i}} (g(\mathbf{x_i}) - \mathbf{y_i})$$

$$\frac{\partial g(\mathbf{x_i})}{\partial \mathbf{x_i}} = \frac{C(\mathbf{x_i})}{\partial \mathbf{x_i}} \mathbf{x_i} + C(\mathbf{x_i}) = \begin{bmatrix} \mathbb{1} & \mathbb{0} & \mathbb{0} & \mathbb{0} & \mathbb{0} \\ \mathbb{0} & \mathbb{0} & 2\mathbf{c}_i\times & \mathbb{0} & \mathbb{1} \\ \mathbb{0} & \mathbb{0} & \mathbb{1} & \mathbb{0} & \mathbb{0} \\ \mathbb{0} & \mathbb{0} & \mathbb{0} & \mathbb{1} & \mathbb{0} \end{bmatrix} = \tilde{C}(\mathbf{x_i})$$

$$\begin{aligned} \bullet \nabla_{\boldsymbol{\omega_i}} Q_i \mathrel{\hat{=}} Q_{\omega i} &= \nabla_{\boldsymbol{\omega_i}} L_i + \nabla_{\boldsymbol{\omega_i}} \mathcal{V}_{i+1}(f(\mathbf{x_i}, \boldsymbol{\omega_i})) \\ &= 2\Sigma^{-1}_{\boldsymbol{\omega_i}} \boldsymbol{\omega_i} + B^T \mathcal{V}'_x, \end{aligned}$$

Proof:

$$\nabla_{\boldsymbol{\omega_i}} L_i = \frac{\partial ||\boldsymbol{\omega_i}||^2_{\Sigma^{-1}_{\boldsymbol{\omega_i}}}}{\partial \boldsymbol{\omega_i}} = 2\Sigma^{-1}_{\boldsymbol{\omega_i}} \boldsymbol{\omega_i}$$

$$\begin{aligned} \bullet \nabla^2_{\mathbf{x_i}} Q_i \mathrel{\hat{=}} Q_{xxi} &= \nabla^2_{\mathbf{x_i}} L_i + \nabla^2_{\mathbf{x_i}} \mathcal{V}_{i+1}(f(\mathbf{x_i}, \boldsymbol{\omega_i})) \\ &= \nabla^2_{\mathbf{x_i}} L_i + A^T \mathcal{V}_{xx} A, \end{aligned}$$

where, the element at the kth row and l^{th} column is denoted by:

$$\begin{aligned} [\nabla^2_{\mathbf{x_i}} L_i]_{kl} &= \sum_{n=1}^{Y} \sum_{m=1}^{Y} [\Sigma^{-1}_{\boldsymbol{\eta_i}}]_{mn} \left(\frac{\partial \tilde{C}^T_{km}}{\partial \mathbf{x}_l} [g(\mathbf{x_i}) - \mathbf{y_i}]_n + \tilde{C}^T_{km} \frac{\partial [g(\mathbf{x_i})]_n}{\partial \mathbf{x}_l} \right), \\ [\nabla^2_{\mathbf{x_i}} L_i]_{kl} &= [\tilde{C}^T \Sigma^{-1}_{\boldsymbol{\eta_i}} \tilde{C}]_{kl} + \sum_{n=1}^{Y} \sum_{m=1}^{Y} \frac{\partial \tilde{C}^T_{km}}{\partial \mathbf{x}_l} [\Sigma^{-1}_{\boldsymbol{\eta_i}}]_{mn} [g(\mathbf{x_i}) - \mathbf{y_i}]_n, \\ [\nabla^2_{\mathbf{x_i}} L_i]_{kl} &= [\tilde{C}^T \Sigma^{-1}_{\boldsymbol{\eta_i}} \tilde{C}]_{kl} + \tilde{\tilde{\mathbf{c}}}^T_{kl} \Sigma^{-1}_{\boldsymbol{\eta_i}} (g(\mathbf{x_i}) - \mathbf{y_i}), \end{aligned}$$

where, $\tilde{\tilde{\mathbf{c}}}_{kl} \in \mathbb{R}^Y$ is the stacked vector of $\dfrac{\partial \tilde{C}^T_{km}}{\partial \mathbf{x}_l}$ for $m \in [1..Y]$.

$$\begin{aligned} \bullet \nabla^2_{\boldsymbol{\omega_i}} Q_i \mathrel{\hat{=}} Q_{\omega\omega i} &= \nabla^2_{\boldsymbol{\omega_i}} L_i + \nabla^2_{\boldsymbol{\omega_i}} \mathcal{V}_{i+1}(f(\mathbf{x_i}, \boldsymbol{\omega_i})) \\ &= 2\Sigma^{-1}_{\boldsymbol{\omega_i}} + B^T \mathcal{V}_{xx} B, \end{aligned}$$

Proof:

$$\nabla^2_{\boldsymbol{\omega_i}} L_i = 2\Sigma^{-1}_{\boldsymbol{\omega_i}} \frac{\partial \boldsymbol{\omega_i}}{\partial \boldsymbol{\omega_i}} = 2\Sigma^{-1}_{\boldsymbol{\omega_i}}$$

$$\bullet \nabla_{\boldsymbol{\omega_i}\mathbf{x_i}} Q_i \hat{=} Q_{\omega x i} = B^T \mathcal{V}_{xx} A,$$

6.4.3 The DDP algorithm

The update equations used for computing the value of the derivatives $\mathcal{V}_x$ and $\mathcal{V}_{xx}$ of the cost function after optimization are:

$$\mathcal{V}_x = Q_{xi} - Q_{\omega i} Q_{\omega\omega i}^{-1} Q_{\omega x i}$$
$$\mathcal{V}_{xx} = Q_{xxi} - Q_{x\omega i} Q_{\omega\omega i}^{-1} Q_{\omega x i}$$

Recursively computing the local quadratic models of $\mathcal{V}_i$ and the optimal estimation changes $\delta\boldsymbol{\omega}_{\boldsymbol{i}}^*$, from $i = N-1$ down to $i = 1$, constitutes the backward pass. In the following, we describe a method for estimating the initial conditions of state variables that depends on the integration of higher order variables once the backward pass is achieved. In our case of application this step retrieves the initial value of the state vector.

In the sense of optimal estimation, the best initial conditions $\delta\rho^\star$ of the problem are the one that will lead to a minimal cost to go at step 0. This amounts to perform a last step at the end of the backward pass that will compute a locally optimal increment in the initial conditions. In the forward pass, this will lead to an impulse dynamics of the system at time zero that can be formulated as:

$$\hat{\mathbf{x}}_0' = \hat{\mathbf{x}}_0 + P\ \delta\rho^\star$$

where, P maps a change in the initial conditions to a change in the state. In our case, as the objective is to estimate the initial conditions of the whole state, P is the identity of $\mathbb{R}^{X\times X}$.

Similarly to $\delta\boldsymbol{\omega}_{\boldsymbol{i}}^*$ but including only one open loop term:

$$\delta\rho^\star = -(P^T \mathcal{V}_{xx} P)^{-1} P \mathcal{V}_x.$$

Note that this termination step is not present in the classical DDP algorithm. The way it is presented here is original but it is inspired from the Parameter-dependent DDP algorithm (PDDP) [Kobilarov 2015].

Once the backward pass is completed, a forward pass computes a new state trajectory. It is the result of the locally optimal changes in the control variables computed throughout the backward pass:

$$
\begin{aligned}
\hat{\mathbf{x}}_0' =& \hat{\mathbf{x}}_0 + P\ \partial\rho^\star \\
For\ i \in 0 : N :& \\
& \boldsymbol{\omega}_i' = \boldsymbol{\omega}_i + k_i + K_i \delta \mathbf{x_i} \\
& \hat{\mathbf{x}}_{i+1} = f(\hat{\mathbf{x}}_\mathbf{i}, \hat{\boldsymbol{\omega}}_i) \\
& \delta \mathbf{x}_{i+1} = \hat{\mathbf{x}}_{i+1}' - \hat{\mathbf{x}}_{i+1}
\end{aligned}
$$

Then, the DDP algorithm consists in iteratively chaining the backward and forward passes until $\nabla_{\boldsymbol{\omega}_i} Q_i \approx 0$.

6.5 Illustration

The presented methodology is illustrated using a simulation of a walking motion with the HRP-2 robot that was purposefully noised, as in Chap. 5. The estimation algorithm was purposely applied to a sub-part of the simulated motion, in order to demonstrate the quality of the estimation for retrieving non-zero initial conditions of the system. In Fig. 6.1, the minimization of the cost function is displayed as well as the convergence of the algorithm.

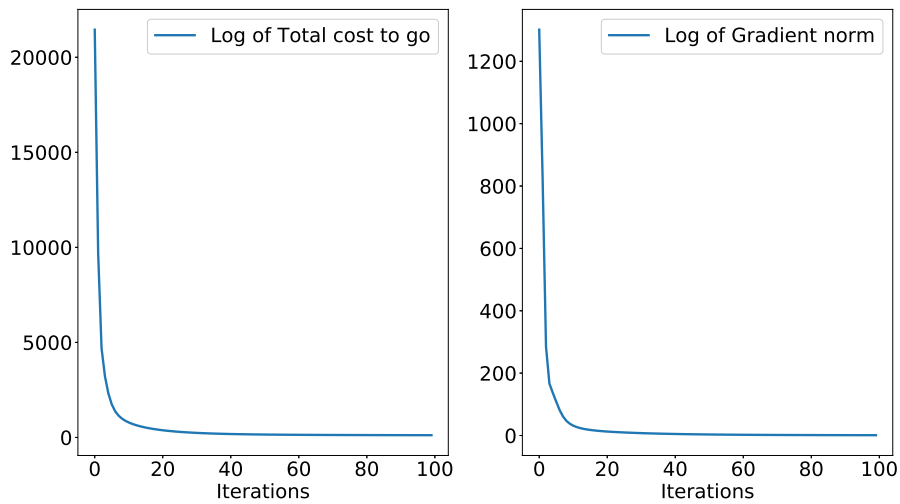

Figure 6.1: (*Left*) Logarithm of the total cost to go as a function of iterations of the DDP. (*Right*) Logarithm of $\nabla_{\boldsymbol{\omega}_i} Q_i$ as a function of iterations of the DDP.

This method allows us to recover the five components of the state trajectory of the robot. The noise on the measurements is filtered thanks to the cost on the control ($\boldsymbol{\omega}_i$) and to dynamics imposed by the DDP formulation. The different sources of information (MoCap, kynematic chain, force sensors) mutually correct one another. This result is particularly highlighted in the first column of Fig. 6.2,

where one can observe the way the three components of the kinematic CoM were noised (in blue), and that the retrieved estimation (in green) is almost perfectly filtered. All the initial conditions are properly recovered (15 scalar variables in total) except for the z component of the CoM which is not observable in standard walking conditions [Carpentier 2016a]. Another nice property of this approach is the quality of the estimation of the three components of the angular momentum (see first column of Fig. 6.3), where the overshooting of the measured kinematic angular momentum, due to noised mass distribution of the robot model, is well corrected. Another interesting result with regard to the approach proposed in Chap. 5 is the quality of the estimation of $\dot{\mathcal{L}}_{\mathbf{c}}$ (see second column of Fig. 6.3), whereas no measurement enables to directly recover this variable, unlike in the case of $\dot{\mathbf{p}}$ (see third column of Fig. 6.2).

6.6 Perspectives

This work is promising for an implementation on the robotic platforms of the Gepetto team (HRP-2 and Talos humanoid robots). To this end, the approach needs to be designed for running online, which requires code optimization, on the one hand, and working on a time sliding-window implementation, on the other hand. As suggested in Sec. 6.3, the measurements vector could also be extended by adding the data from the robot's IMU. The quality of the angular and linear momenta derivatives estimation suggests that this way of estimating the centroidal state of the robot could perform well for designing a stabilizer that would take into account the whole dynamics of the CoM. It turns out that, during the DARPA robotics challenge, the only not-falling robot was endowed with such a stabilizer, demonstrating the efficiency of centroidal state estimation. This is left as a future work.

In the biomechanics community, such estimation tools could be used to provide accurate recordings of human motions, on the one hand, and to evaluate state of the art methods for estimating the centroidal state of humans, on the other hand. The strength of our approaches being that they do not rely on statistical regression parameters or simplified modeling assumptions.

The time global approach of the DDP algorithm provides the nice performances of the estimation method presented in this chapter. This is an improvement with regard to what was proposed in Chap. 5, even though the sophisticated way of handling the complementarity of the measurements was not included in this work. Therefore, in order to have the best of both worlds, it would be necessary to import in the DDP formulation the information brought by the central axis of contact wrench and the spectral complementary filtering presented in Chap. 5. The way of achieving this process remains an open question, but following this idea, the z bias of the CoM could be better estimated, provided that the central axis of contact wrench (in the direction of the resulting contact force) is appropriately excited thanks to a specially designed movement.

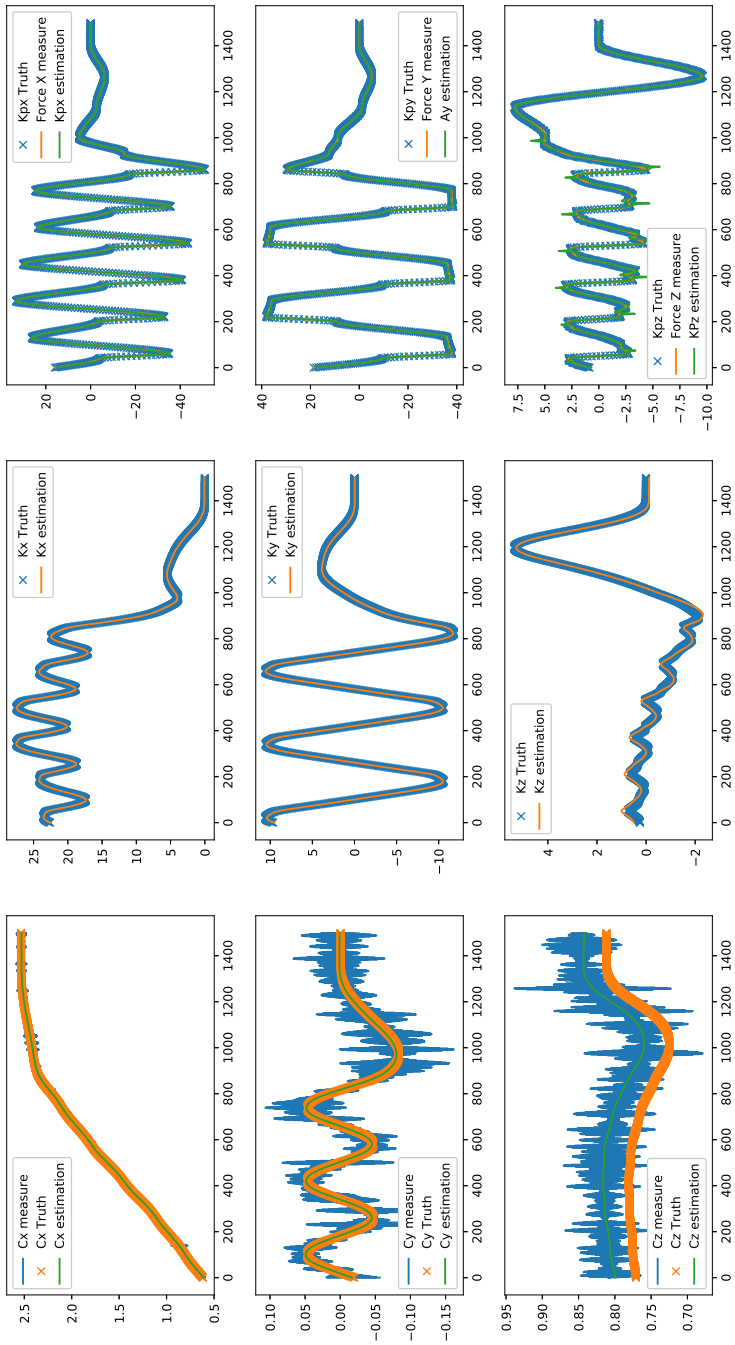

Figure 6.2: Three components of $\mathbf{c}$, $\mathbf{p}$ and $\dot{\mathbf{p}}$

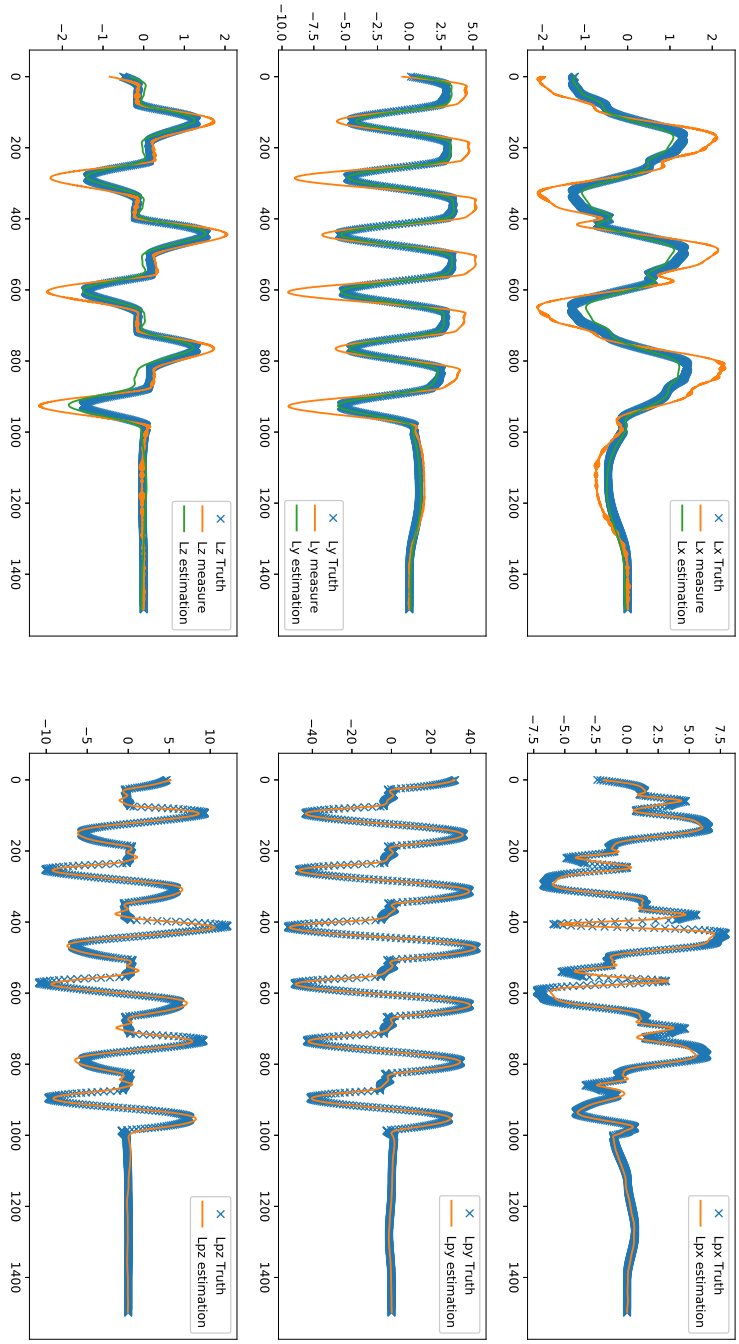

Figure 6.3: Three components of $\mathcal{L}_c$ and $\dot{\mathcal{L}}_c$

Chapter 7

Should mobile robots have a head ?

A rationale based on behavior, automatic control and signal processing

---

"If, then, there were no solid bodies in nature there would be no geometry.(...) On the other hand, our body, thanks to the number of its articulations and muscles, may have a multitude of different movements, but all are not capable of "correcting" a modification of external objects; those alone are capable of it in which our whole body, or at least all those in which the organs of our senses enter into play are displaced ***en bloc*** *— i.e., without any variation of their relative positions, as in the case of a solid body. "*, [Poincaré 1905, "Space and Geometry"].

Contents

7.1 Introduction 116

7.2 The Head in animals 119

7.3 A Head for state observation in robotics 121

7.3.1 State space representation and control of a multi-joint mobile robot. 121

7.3.2 The observation problem. 122

7.3.3 Head morphology and exteroceptive sensors. 124

7.4 A Head for signal processing and cognition 124

7.4.1 Centralizing exteroceptive perception and its processing. . . . 124

7.4.2 Shortening of the brain-ESO transmission channel. 125

7.4.3 Stiffening the exteroceptive kinematics. 125

7.4.4 Head mobility for enhanced perception 125

7.5 The role of the head in locomotion and manipulation 126

7.5.1 The head at the front-end of the movement for locomotion. . 126

7.5.2 One Head for supervising manipulation 127

7.6 Conclusion 127

Figure 7.1: *Kingfisher in the wind.* These pictures are extracted from a short video clip of the bird fishing. The kingfisher's head remains still, while its body, attached to a swaying blade of grass, moves and deforms in all directions. The red dot is fixed in the frame of the camera, showing the anchorage of the head with regard to an inertial frame, despite the external perturbation applied to the bird's body.

*The opening quote of this chapter reveals how Poincaré had intuitively sensed the importance of the relative placement of the exteroceptive sensory organs for self motion perception or, in our words, for external state estimation. The "en bloc" displacement that he refers to is reminiscent of what the head provides in terms of kinematic support for the exteroceptive sensory organs. In the following, we discuss the role of the head for state estimation and perception in organisms, and the relevance of such a solution for mobile robotics systems. This work was realized in collaboration with researchers Vincent Bels and Emmanuelle Pouydebat from the Muséum National d'Histoire Naturelle de Paris, France [**Bailly** 2018b].*

7.1 Introduction

In Sec 2.1, it was recalled that robots are machines that should be able to perceive, process sensory information and act in the physical world. In order to endow robots with such capabilities, roboticists are free to use the most advanced methodologies and techniques as well as the best adapted materials. A priori, their work should not be constrained by biomimicry concerns as only performance objectives should guide it. However, in the quest of designing systems that are able to sense and drive their movement consistently, animals appear as living models of efficiency. For this reason, roboticists sometimes try to design bio-inspired robots.

Figure 7.2: Examples of anterior structures in different bilateral animals highlighting their heads, sensory and trophic systems. From left to right: Zygoptera, Sepiida, Felidae (*Panthera* lineage), Callitrichinae, Gekkota, Tetraodontidae, Culicidae, Casuarius.

However, in most cases, the bio-inspiration focuses on a particular functionality that engineers attempt to reproduce. In this perspective, various bio-inspired systems have been designed. Among the most remarkable are the salamander robot in [Ijspeert 2007] that demonstrates locomotion modes based on central pattern generators, the use of insect optical flow for navigation in [Ruffier 2003], the gecko robot in [Menon 2004] whose leg coating texture reproduces adhesion abilities, the eel robot in [Boyer 2008] endowed with an electric sense, and, more generally, humanoids robots designed to reproduce bipedal walking [Naveau 2017]. Despite these encouraging achievements, a lot of work remains to be done to understand the key principles that endow living beings with such autonomous navigation capabilities and transfer them to robots. Developing research in this direction is possible only through interdisciplinary studies involving biology and engineering. With this objective in mind, the present chapter aims at gathering a set of arguments from life sciences and robotics to demonstrate that the existence of the head under the process of cephalization ([Manzanares 2000]) is linked to animals' ability to perform voluntary spatial actions and simplifies the integration process of sensory and motor functions for navigation. First, morphological and behavioral characteristics of animals capable of voluntary spatial action through evolution are examined. Then, the complexity of state-space representation and observation of multi-joints mobile robots is presented in the context of automatic control. After that, some perception related features brought by the presence of a head are presented in the light of signal processing. Finally, the role of the head in locomotion and manipulation in animals and robots is discussed, paving the way for future robot design.

Figure 7.3: Artist's impression of the fauna at the Ediacaran–Cambrian boundary. Different kinds of morphotypes are illustrated as well as their feeding behaviors. © Agathe Haevermans.

7.2 The Head in animals

The evolution of organisms is related to a large number of external (environmental) and internal (phylogenetic or historical) pressures [Bateson 2013]. Every organism has to perform a series of motor actions to ensure its fitness at any time of its life. These actions are produced by functional structures in response to environmental stimuli. The process of natural selection has governed the shape of these structures and their functioning under different but complementary proximate and ultimate causes through the evolutionary time [Tinbergen 1963]. Therefore, each individual has to optimize various motor strategies to respond to the diverse constraints of its environment (abiotic and biotic) and to its physiological needs (i.e., feed and cover the physiological demands, find mates and cover the reproductive effort, find partners for social interactions, etc.). This ability to perform different motor actions through various integrated systems, such as limbs or jaws, necessarily relies on appropriate decision mechanisms initiated and controlled by complex releasing factors [Legreneur 2012]. Anatomy and functional morphology associated with developmental research make it possible to empirically categorize the structures and the motor patterns involved in these motor actions. Behavioral ecology and other disciplines (i.e., cognitive phenotypes studies) provide an understanding of their sensory-motor bases. Some of them are determined as taxes (animals simply heading towards or away from sources of stimulation), some other as fixed action patterns (FAPs, or activities with a relative fixed pattern of coordination [Lorenz 2013, Schleidt 1974]).

The evolutionary and ecological pressures involved into a trophic web can be considered as playing a primary role (though not the only one) to explain the diversity of these actions in organisms. Despite continued uncertainty on how community and ecosystem trajectories are working, a coherent pattern of ecological pressure appears to be related to the trophic web involving all organisms in the majority of their voluntary motor actions. In such a web, individuals are either predators (including food foragers) and/or preys at one time of their life and thus have to select actions within contrasting contexts to gain food and energy while avoiding being injured or killed. A rough review of all metazoan organisms into extinct and extant food web shows that they can be divided into three major categories, according to their primary feeding behaviors [Budd 2017, Erwin 2011]: fixed organisms with no voluntary exploratory movements, organisms whose movements follow any type of gradient (e.g., chemical), and organisms capable of voluntary movements. This difference remains in the diversification of all taxa, although our understanding of the earliest evolution of metazoans is still a controversial problem as well as the precursors, causes, and consequences of their evolution. For example, the concept of ecosystem engineering attempts to explain how voluntary activities have affected the biological diversity of organisms through their ecological and evolutionary implications (i.e., nutriments flow modification, sediments transformation) at the Ediacaran-Cambrian boundary. Although faunas of both eras were probably temporally separated by a mass extinction, some

forms of moving bilaterian animals that are characteristic of the Cambrian fauna are suggested to be present since the last Ediacara [Budd 2017, Erwin 2011]. Although their evolution is not discussed here, paleontological evidences (organisms and traces) suggest that these bilateral organisms developed voluntary tasks associated with two main strategies in aquatic environment: movement on and in the substratum, and navigation at benthic and pelagic levels in the water column. From anatomical descriptions, these actions were associated with a structural anterior-posterior organization. Besides, since the early time of metazoan evolution, two major predator/prey strategies seem to have emerged: burrowing in benthic communities, and hunting or escaping in other communities. Indeed, phylogenetically related urrowing activities (horizontal, linear or zigzag series of short, widely U-shaped galleries) recorded from traces appearing around 560–555 Mya were probably produced by bilaterian animals with symmetry related to complex body structures (e.g., coeloms). Some authors ([Pecoits 2012]) suggested that burrowing was hydraulically done with a frontal (anterior) organ that can be called *head*. Bilateria of the Cambrian era developed new ecological niches and strategies such as active hunting and escaping from predators, and probably building more complex branching burrows. Therefore the Cambrian Period marks an important point in the history of the shape of organisms linked to their motor actions in space. Indeed, most of the major groups of animals first appearing in the fossil record ("Cambrian Explosion") show rather similar morphotypes with two successive anterior-posterior regions of the body: an anterior region cumulating a series of sensory systems (visual, olfactory, vomerolfactory, auditory, etc.) with a specialized trophic system, and a posterior region comprising morphological devices permitting body deformations via multi-joint systems, in order to move in determined directions. The anterior region comprises a series of symmetrical complex structures (e.g., eyes, ears, whiskers, antennae) and the exteroceptive sensory organs (ESOs), that sense exteroceptive stimuli for actively interacting with the environment and generating voluntary spatially related actions (see Fig. 7.2). The head can be either fixed or mobile, probably to improve the success of actions implying the integration of sensory information or recruiting the trophic structure. This morphotype with accumulated morphological and sensory systems into the anterior region includes a CNS to integrate the sensory information and produce coordinated motor orders for the body and the head (move towards a prey and catch it). Studying the evolution of such organisms through their centralized nervous system shows two alternative possibilities from the analysis of the brain–body complexity among extant Bilateria. The first one, a diffuse nerve plexus with ganglionated systems, probably existed in Ediacaran organisms that were not able to produce voluntary coordinated actions. The second one, an anterior cephalic nerve system (brain or a series of nervous ganglions) arose in the common Bilateria ancestor. From this point, ecological pressures could have triggered the evolutionary pattern of complex actions, in the context of two body regions with highly different morphological and functional traits. Indeed, within trophic webs, the predatory-prey strategies involved into an escalatory "arms race" can be as complex as needed

Figure 7.4: Three different multi-joint mobile robots at LAAS: the flying manipulator Aeroarm (left), the mobile manipulator Jido (center), and the humanoid robot Talos (right). The usual choices for their root frame placement are displayed.

to produce highly diversified morphological systems and FAPs under the control of the nervous system. Along the evolutionary process of the various phyla, these FAPs have been modulated by a series of traits such as learning or cognitive abilities. As soon as animals are able to voluntarily control their actions at any stage from initiation, they can exploit diverse ecological niches.

In conclusion, one of the main characteristics of all organisms that developed the ability to produce complex voluntary spatial actions along their evolution is the morphological, developmental and functional dichotomy of the body regions into a head, mobile or not, integrating the majority of sensory systems and the rest of the body.

7.3 A Head for state observation in robotics

Although robots are not subject to physiological needs, the morphological solutions that arose in animals capable of voluntary spatial actions are relevant for mobile robotics design. In the following, we consider the problem of endowing a multi-joint mobile robot with the capacity to autonomously drive its motion in space. The theoretical framework that allows engineers to formalize this problem is the one of automatic control, the science of modeling, analysis and control of dynamic systems. It was introduced in Sec. 2.2.

7.3.1 State space representation and control of a multi-joint mobile robot.

Contrary to manipulator robots, which are rigidly fixed to the ground by their basis, mobile robots can move freely in their environment. Depending on their locomotion

mode, they can strongly differ as shown in Fig. 7.4.

Their kinematic modeling was recalled in Sec. 2.2, where the notions of internal and external states were introduced. In order to simply illustrate these definitions, let us consider the case of a planar robot made of three bodies linked by two rotational joints, as depicted in Fig. 7.5a. Each joint is actuated by a motor and thanks to the combination of both rotations the robot is supposed to be able to move in the plane. The internal state of the robot is defined by two angles q_1 and q_2. Once both angles are fixed, the pose of the robot in the plane depends on two degrees of freedom in translation and one in rotation as shown in Fig.7.5b. Hence, five scalar parameters are necessary to fully describe the kinematic configuration of the robot in the plane. Though the parameterization of the internal state by means of q_1 and q_2 appears to be quite natural, many parameterization can be used to describe the external state. Figures 7.5c and 7.5d depict two of them, encoded with respect to a world frame. In the first one, the pose of the first body is fully determined by its orientation θ_1 and the coordinates (x_1, y_1) of a point attached to it. Whereas in the second case, the parameterization is distributed over the three bodies, including the abscissa x_1 of a point on the first body, the orientation θ_2 of the second body, and the ordinate y_3 of a point on the third body. From a mathematical point of view, if all variables can be determined with the same accuracy, both parameterizations are equivalent. In practice, we will demonstrate in the sequel that, as the measurement relies on sensors, these two parameterization cannot be implemented with the same level of accuracy.

7.3.2 The observation problem.

As previously explained the state variables cannot be directly measured and must be reconstructed from data provided by sensors at the output. Ideally, the sensors should be installed in such a way as to limit geometrical transformations and data processing. Usually the internal state of robots can be easily reconstructed from encoders located at the joints. It is then possible, modulo proprioceptive biases and flexibilities, to have a good knowledge of the internal structure of the robot and its variation. However, as previously explained, several parametrizations can be used to represent the external state. These parametrizations fall into two main categories as illustrated by examples (c) and (d) in Fig. 7.5. In the first one, the exteroceptive sensors are used to fully measure the pose and the velocity of one of its bodies, called *root-body*, whereas in the second, the exteroceptive sensors are distributed on different bodies of the robot providing partial measurements of their pose and velocity. In view of the inherent proprioceptive biases and the flexibility of the structure these two strategies are not equivalent. Indeed, with the first strategy, the quality of the estimation of the pose and velocity of the root-body only depends on the accuracy of exteroceptive sensors mounted on it. Whereas using the second strategy, the estimation of the complete pose and velocity of any one of these bodies is degraded by proprioception inaccuracy. In sum, for the sake of accuracy, it is preferable to attach all exteroceptive sensors to one root-body in order to fully

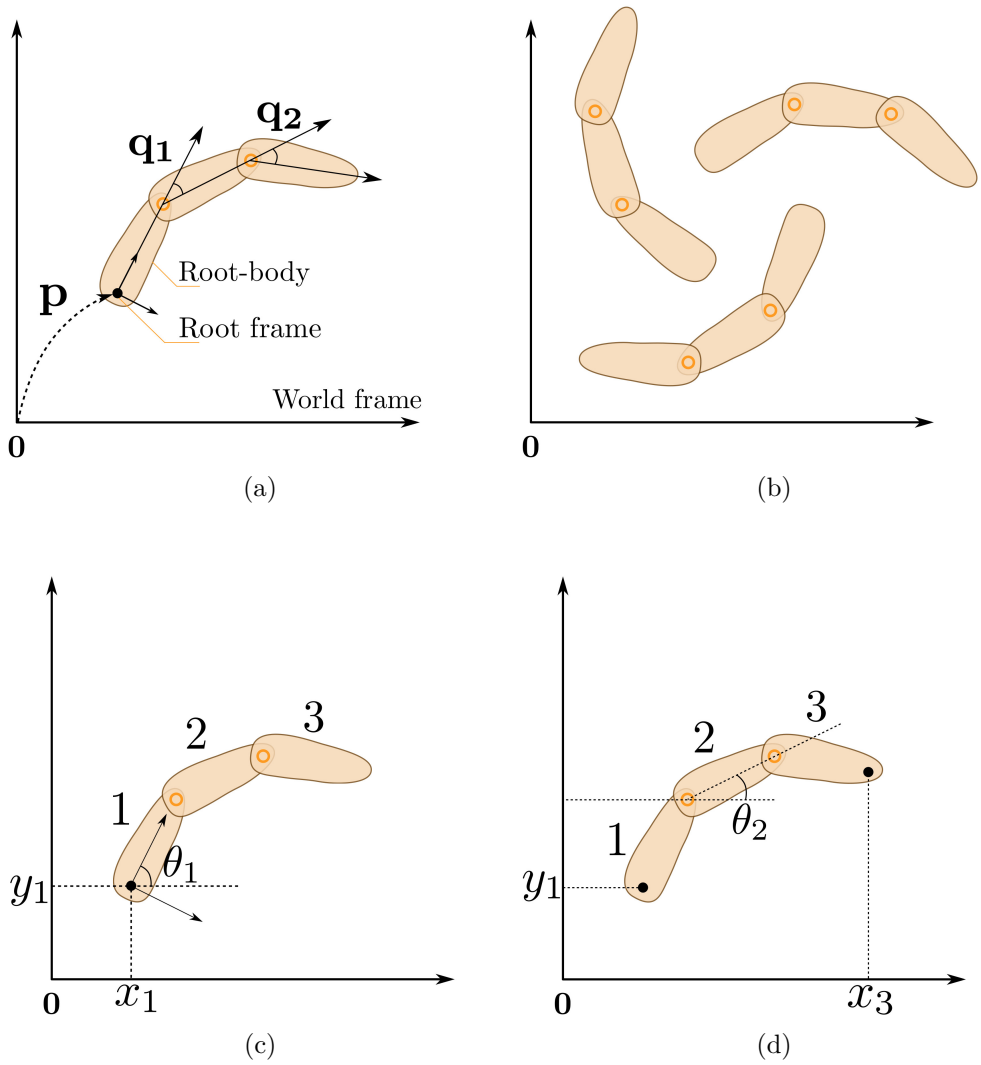

Figure 7.5: Illustrations depicting the internal and external states of a simple polyarticulated robot. (a): Absolute parameterization of the system in the plane. (b): Between the three cases depicted, only the external state of the system is changed. (c): The external state is parametrized by fully positioning the first body. (d): The parameterization of the external state is distributed on the three bodies of the robot.

reconstruct its pose and velocity, and then deduce the relative configuration of other bodies from proprioception, rather than distributing the exteroceptive measurement on different bodies and then integrating them through proprioception. Furthermore, this strategy offers a natural way to decouple the exteroceptive anchoring of the robot in its environment and the estimation of its internal state. In practice, the 12 state variables describing the pose and the velocity of the root-body can be

reconstructed from the measurement provided by an inertial central unit, combined with exteroceptive sensors such as cameras, laser, microphones, sonars, etc.

7.3.3 Head morphology and exteroceptive sensors.

Considering the analogy with the notion of root-body in robotics, it is interesting to remark that, in animals, the anatomic symmetry of the head and the positioning of the ESOs on it offer natural spatial references. Whether they are eyes, ears, whiskers, antennae, or of any other sort, exteroceptive sensors are symmetrically placed on the head and turned outward, making the "center of the head" as a common virtual origin for multi-sensory perception. This organization provides a natural and simple way of defining right, left, up and down direction for the animal, playing exactly the same role as a reference frame in geometry. Following this idea, interesting works have been carried out in humans based on the perception of visual and auditory targets alignment [Barbeito 1979, Neelon 2004, Sukemiya 2008]. They reported the existence of a similar origin for vision and hearing in humans strongly linked to the position of the ESOs. The sagittal plane of the head and the direction of gravity provided by the vestibular system constitute two fundamental geometrical references which, combined with visual and auditory data, provide all the necessary kinematic information to fully localize the head pose and estimate its velocity with respect to its environment.

7.4 A Head for signal processing and cognition

7.4.1 Centralizing exteroceptive perception and its processing.

The purpose of exteroceptive multisensory fusion is to combine a variety of sensory signals to mutually enrich them in order to make the perception as complete as possible. The fusion of these different signals can only be accomplished by collecting and matching information, a solution provided by the brain. For instance, the McGurk effect [McGurk 1976] and other experiences of sensory enrichment [Ernst 2002, Hillis 2002, Clark 2013] are evidences that the addition or the removal of a sensory modality makes it possible to change the overall interpretation of a phenomenon. Alongside, the spatial proximity of the ESOs resulting from their attachment to a head, enables a spatially and temporally coherent acquisition of the different exteroceptive sensory modalities involved in multisensory perception. This seems essential since most of the physical processes living beings have to measure vary in space and time. Thus, if the ESOs were dispersed over the body, it would be necessary to estimate the measurement that they would have provided from a same spot and at the same time, in order to coherently enrich each other. For example, picture an imaginary creature with its ears placed on its hands and its eyes placed on its head. The spatial matching of the two resulting signals would require to estimate what the ears would have acquired if they had been located near the eyes, or vice versa. It goes without saying that this problem is of such mathematical

complexity (equations of propagation, diffusion, diffraction, dynamics, etc.) that the centralization of ESOs on the head considerably simplifies the problem of coherent multisensory fusion. Cephalization, the evolutionary trend in which the concentration of the nervous system along with the migration of the ESOs result in a head, thus provides an efficient solution with regard to both acquisition and processing of multisensory signals.

7.4.2 Shortening of the brain-ESO transmission channel.

A second feature provided by cephalization is the proximity of the ESOs with regard to the CNS. This observation relates to the fields of information theory and data transmission, which attest that shortening a transmission channel limits a large number of undesirable effects, such that attenuation, phase distortion, delays and different noises that depend on the type of transmission and on the environment. According to Shannon [Shannon 1949], who connected the bandwidth of a communication channel to its signal-to-noise ratio introducing the notion of channel capacity, the less distorted the signal, the higher the admissible bitrate. In the context of visual, auditive and inertial data transmission, shortening the connections between the brain and the ESOs is one way of increasing the capacity of this transmission channel in order to increase the admissible flow rates which contribute to the richness of animal perception.

7.4.3 Stiffening the exteroceptive kinematics.

Another interesting characteristic of the head is the kinematic limits that it imposes between the ESOs, especially in the clade of craniates. These animals are chordates with a cartilaginous or bony skull protecting the anterior part of the CNS. This rigid support strongly constrains the mobility between the ESOs which are fixed on it, limiting it to voluntary and very well calibrated displacements (eye saccades, ear and nose inflections, etc.). These kinematic constraints simplify the mathematical relationship between the signals acquired by different sensory modalities, enabling simple implementation of intermodal processes. For instance, the vestibulo-ocular reflex relies on simplified and very well calibrated transformations between the inner ear and the eyes. Moreover, these kinematic constraints make it easier to estimate the relative placement of the various ESOs, by reducing the number of parameters to be estimated. For instance, the distances between the two eyes, the two ears, the inner ears and the eyes, etc., are constant in most craniates. Thus, the estimation of the extrinsic calibration of the ESOs, which is necessary for multi-sensory fusion (see [Zhang 2004]), is simplified.

7.4.4 Head mobility for enhanced perception

As the ESOs are gathered on it, endowing the head with sufficient mobility and proprioception is a way of mechanically filtering and stabilizing perception. Indeed, as the head is attached to the body, dynamic effects of the body moving during

locomotion may induce disturbance on exteroceptive measurements. Notably, in legged organisms, foot contacts with the ground generate strong undesirable accelerations that are transmitted throughout the body via its musculo-skeletal structure. Decoupling the movement of the head from the one of the body is an efficient mean of compensating for these disturbances (see Fig. 7.1, where head stabilization in Kingfishers is highlighted). Such a decoupling has been observed in humans during walking, based on vestibular data [Pozzo 1990] and thanks to the vestibulocollic reflex that stabilizes visual and auditory perception [Wilson 1995]. In [Laumond 2017], it was explored how this stabilization of the head could mechanically contribute to the balance of bipedal walking. In addition, the mobility of the head allows for an efficient implementation of active exploration strategies that are essential to perception [Bajcsy 1988]. Indeed, moving the head alone is more precise and requires less energy than performing whole-body exploration. This mobility, however, must be supported by a rich proprioception at the neck level, as observed in many animals and in humans [Pettorossi 2014].

7.5 The role of the head in locomotion and manipulation

7.5.1 The head at the front-end of the movement for locomotion.

Addressing the question of the head position with regard to the body is highly relevant in the context of locomotion. Animals whose morphology is bilateral are structured along a mouth-anus axis and, except for bipeds in which this axis is verticalized, their locomotion is directed along this axis. Whatever the mode of bilateral locomotion (flying, swimming, legged locomotion,...), the head of these animals precedes the rest of their body. The ESOs placed on the head sense the part of the environment ahead and the motor system is specialized to produce this forward movement. A very wide range of species including fishes, worms, insects, birds and mammals follow this model for locomotion. Interestingly, in engineering, such a model of locomotion directed along a main axis with specialized thrust and control has guided the conception of many vehicles. Wheeled vehicles are certainly the most representative ones among them. Thanks to the rolling-without-slipping constraint, which prevents instantaneous lateral movement, the control is greatly simplified. It boils down to two control gears, one for steering the wheels and the other one for controlling the acceleration. One can imagine how complex would be the control to stay the course and avoid drifting if the wheels were spherical instead of circular. The same phenomenon applies to boats equipped with a centerboard, to planes, etc. In general, all of these systems are differentially flat, and the cascade structure of their dynamics can be controlled from a small number of variables [Sira-Ramirez 2004]. It is thus possible to easily control the movement of a truck pulling several trailers by controlling only the leading vehicle. As for the head, the steering center of such vehicle is placed ahead to enable the

pilot to perceive the part of space towards which the motion is directed.

7.5.2 One Head for supervising manipulation

Though many animals possess their mouth as only gripper (worms, fishes, snakes, etc.), and others are equipped with several end-effectors (paws, claws, hands, tentacles) as in mammals, birds or cephalopods, in either case they only have one head. In the second group, the existence of additional effectors enables manipulation behaviors. Each end-effector could be equipped with exteroceptive sensors, although this would lead to a redundant state observation, but having a unique head makes it possible to decouple exteroceptive perception from other motor tasks. Indeed, in these animals, the head is an easily steerable multi-sensory perception platform that can use exteroceptive feedback to coordinate manipulation while providing an independent anchoring with the environment.

7.6 Conclusion

Even though the head is a key structure in animals able to perform voluntary spatial actions (see Fig. 7.2) and despite the numerous computational arguments presented in this paper, today few robots are supplied with a head that actually plays a functional role in their navigation. The main reason is that robotics is still a very young science and few works really attempt to integrate multisensory perception and motor control in a robust way that would emphasize the need for such a centralizing structure. In humanoid robots for instance, the presence of the head is mostly motivated by the sake of anthropomorphism. But the root-body that is usually taken into account for modeling their external state is the waist. The reason for this choice is that most walking pattern generators are based on the dynamical link between the CoM located near the waist in standing position and the center of pressure on the ground. As a consequence, the pose and the velocity of the root-frame are usually not reconstructed from exteroceptive data but rely on proprioceptive measurements along the leg, plus inertial data provided by an IMU located in the trunk. Clearly, in such a scheme, the control and the observation problems appear not to be optimally connected, contrary to what could be obtained by using a head as a pivot body between exteroceptive measurement and internal motor control. In many other robots, as illustrated in Fig. 7.4, the root-frame used for modeling the external state is usually located along the main axis of the robot basis, in order to simplify the expression of the robot dynamics, but without real concerns of exteroceptive perception. So far, no theory exists to specify where exteroceptive sensors should be placed on a robot in order to optimize the execution of navigation tasks. If today's robots do not appear to suffer from the lack of a head, it is reasonable to assume that this structure will appear necessary as soon as tasks require deeper multisensory and sensorimotor integration. Finally, the structural role played by the head in sensory data acquisition and processing could be involved in the emergence of higher cognitive capacities related to the

representation of space, the construction of motor plans and the ability to learn and generalize.

We thank André Nel and Romain Garrouste (Sorbonne Université, ISYEB, France) for courteously providing pictures of Fig. 7.2.

Conclusion and perspectives

All along this thesis, we have conducted a reflection on how to explain and describe human locomotion and how to estimate the state of the body during displacements. Following the recalls of Part I on basics methods in biomechanics and robotics, the contribution of the thesis were presented in Parts II and III.

Part II was dedicated to present new methods for describing and explaining human locomotion. In Chap. 3, a new mechanical descriptor of human locomotion was introduced, based on the computation of the central axis of the external contact wrench. It was shown that studying the distance between this axis and the global center of mass reveals information about the dynamic state of the body, and in particular, that it depends on the angular momentum expressed at the center of mass and on the net external force applied to the body. In Chap. 4, a general framework was proposed for identifying dynamic task functions that appear to be preferentially controlled by the CNS in humans, based on the task function approach and on an extension of the UCM approach. The proposed method can be used as a tool for understanding how the CNS organizes the motor control of the body, especially in terms of tasks hierarchy. This theoretical contribution was illustrated by the study of parkour movements for which task functions were formulated in terms of whole-body linear and angular momenta derivatives.

Part III was devoted to the work carried out on centroidal state estimation in robotics and biomechanics and on its comparison with state observation in animals. In Chap. 5, we presented a method to simultaneously estimate the CoM position and the variation of angular momentum expressed at the CoM by complementary filtering of kinematic and kinetic data. The proposed framework was validated in simulation, where it was shown to reduce the norm of the error between the estimation of the CoM position and its real value, when compared to kinematic estimation alone. Its application to human walking data was also presented for illustration purposes. In Chap. 6, another approach for estimating the centroidal state of systems in contact was presented. This time, the estimation process included a global time preview that could model how locally changing the estimated state would impact the estimated trajectory, in order to perform full-information estimation. To this end, the differential dynamic programming algorithm was applied to this estimation problem, leading to proper initial conditions recovery and to accurate estimation of the CoM position, angular and linear momenta and their first time derivative. Finally, in Chap. 7, we presented a multidisciplinary work about the role of the head for state estimation and perception in animals. We have highlighted that the head is a key anatomical structure in animals able to perform voluntary spatial actions, from the first known appearance of such behaviors at the Ediacaran-Cambrian boundary, to all extant bilaterians. Then, we developed a set of arguments from automatic control and signal processing to demonstrate that the head, integrating the exteroceptive sensory organs, plays a crucial role in both

perception and state observation.

Perspectives in human motion analysis

The work that was realized during this thesis opens up interesting research directions in the field of human motion analysis. First, the experimental work that was carried out with the mechanical descriptor of human locomotion should be further investigated for multiple locomotion scenari, as well as for impaired locomotion in patients suffering from amputations, brain damages following strokes, etc. A preliminary study has begun on this topic, using the mechanical descriptor for locomotion analysis in lower-limb amputees wearing prosthetic devices. Secondly, the proposed UCM extension should be now applied to different and less constrained tasks, specifically designed to highlight that the strong ITC effects observed in this study were not artifacts coming from the dimension of the configuration space (the variances were normalized to cancel this potential drawback). For instance, the precision jump could be adapted in such a way that the geometry of the target could be relaxed (from a point to a line or to a surface). Finally, among the interesting outcomes of our work on centroidal estimation, we believe that the developed methods could be applied for benchmarking anthropometric tables rather than only comparing them to one another, or that they could help designing personalized body segment inertial parameters estimation by providing feedback on the accuracy of the centroidal state values.

Perspectives in centroidal state estimation

One of our motivations for working on centroidal state estimation was the lack of centroidal state feedback in real-life experiments with humanoid robots. Consequently, one of the natural developments of our work on centroidal state estimation would be to use it for the design of an efficient stabilizer for humanoid robots. Such an extension would require a real-time implementation as well as the development of balancing control strategies based on the centroidal state of the robot. Another improvement would be to incorporate the data from the IMUs of the robots to our estimation methods, which was not done yet because they are not part of the usual biomechanical measurement equipment, but would be really relevant in robotics. As it was suggested in Sec. 6.6, our estimation methods would be strengthened by merging them, i.e., importing the information brought by the central axis of contact wrench and the spectral complementary filtering presented in Chap. 5, into the DDP formulation of Chap. 6.

Perspectives in animal state observation

The prospective problem that was formulated in this last chapter of the thesis seems fundamental and highly relevant to us, as it connects all the questionings that we

encountered while working on defining, describing and understanding locomotion. Therefore, we hope to have the opportunity to continue this work and to explore it further. Among the questions that sparked our deepest interest is the link between centroidal state estimation and head-centered exteroceptive state estimation. Mathematically speaking, these two approaches are equivalent, except to one transformation involving masses and geometric body data [Carpentier 2016b]. In practice, we want to investigate if this transformation is performed by animals, in other words, do they have some feedback on their centroidal state? Then, it would be relevant to model whether decoupling the dynamics of the centroid from the dynamics of the sensors is an efficient way of disambiguating acceleration signals for instance. We already raised some elements of answer, among which are the accuracy of the external state estimation and the mechanical decoupling of the sensors support for filtering. A lot of work remains to be done to fully understand why this biological solution is so widespread and what are the fundamental sensory and computational concepts that can be drawn from it.

Appendix A

Calculation details of the UCM extension applied to kinematic and dynamic task functions

Partial derivatives of $\dot{\mathbf{e}}$ with respect to $\mathbf{q}$ and $\dot{\mathbf{q}}$

$$B(\mathbf{q}, \bar{\dot{\mathbf{q}}}) = \frac{\partial J(\mathbf{q})\bar{\dot{\mathbf{q}}}}{\partial \mathbf{q}}.$$

Let us write $J(\mathbf{q})\bar{\dot{\mathbf{q}}}$ component-wise:

$$(J(\mathbf{q})\bar{\dot{\mathbf{q}}})_i = \sum_{k=0}^{n} (J(\mathbf{q}))_{ik} \bar{\dot{q}}_k.$$

This leads to the component-wise expression of B:

$$B_{ij} = \frac{\partial (J(\mathbf{q})\bar{\dot{\mathbf{q}}})_i}{\partial q_j} = \sum_{k=0}^{n} \frac{\partial (J(\mathbf{q}))_{ik}}{\partial q_j} \bar{\dot{q}}_k.$$

Note that configuration $\mathbf{q}$ contains rotational joints which are elements of the special orthogonal group $SO(3)$ and have to be time differentiated accordingly.

Partial derivatives of $\ddot{\mathbf{e}}$ with respect to $\mathbf{q}$, $\dot{\mathbf{q}}$ and $\ddot{\mathbf{q}}$

Calculation of D

$$D(\bar{\mathbf{q}}, \dot{\mathbf{q}}, \bar{\ddot{\mathbf{q}}}) = \frac{\partial (\dot{J}(\bar{\mathbf{q}}, \dot{\mathbf{q}})\dot{\mathbf{q}})}{\partial \dot{\mathbf{q}}}.$$

Let us write $\dot{J}(\bar{\mathbf{q}}, \dot{\mathbf{q}})\dot{\mathbf{q}}$ component-wise:

$$(\dot{J}(\bar{\mathbf{q}}, \dot{\mathbf{q}})\dot{\mathbf{q}})_i = \sum_{k=0}^{n} (\dot{J}(\bar{\mathbf{q}}, \dot{\mathbf{q}}))_{ik} \dot{q}_k.$$

This leads to the component-wise expression of D:

$$D_{ij} = \frac{\partial(\dot{J}(\bar{\mathbf{q}}, \dot{\mathbf{q}})\dot{\mathbf{q}})_i}{\partial \dot{\mathbf{q}}_j},$$
$$D_{i,j} = \sum_{k=0}^{n} \frac{\partial((\dot{J}(\bar{\mathbf{q}}, \dot{\mathbf{q}}))_{ik}\dot{q}_k)}{\partial \dot{\mathbf{q}}_j},$$
$$D_{i,j} = \sum_{k=0}^{n} \frac{\partial(\dot{J}(\bar{\mathbf{q}}, \dot{\mathbf{q}}))_{ik}}{\partial \dot{\mathbf{q}}_j}\dot{q}_k + \delta_{jk}(\dot{J}(\bar{\mathbf{q}}, \dot{\mathbf{q}}))_{ik},$$

with δ the Kronecker delta.

Calculation of E

$$E(\mathbf{q}, \bar{\dot{\mathbf{q}}}, \bar{\ddot{\mathbf{q}}}) = \frac{\partial(\dot{J}(\mathbf{q}, \bar{\dot{\mathbf{q}}})\bar{\dot{\mathbf{q}}})}{\partial \mathbf{q}} + \frac{\partial(J(\mathbf{q})\bar{\ddot{\mathbf{q}}})}{\partial \mathbf{q}}.$$

Let us write $\dot{J}(\mathbf{q}, \bar{\dot{\mathbf{q}}})\bar{\dot{\mathbf{q}}}$ component-wise:

$$(\dot{J}(\mathbf{q}, \bar{\dot{\mathbf{q}}})\bar{\dot{\mathbf{q}}})_i = \sum_{k=0}^{n} (\dot{J}(\mathbf{q}, \bar{\dot{\mathbf{q}}}))_{ik}\bar{\dot{q}}_k.$$

Let us write $J(\mathbf{q})\bar{\ddot{\mathbf{q}}}$ component-wise:

$$(J(\mathbf{q})\bar{\ddot{\mathbf{q}}})_i = \sum_{k=0}^{n} (J(\mathbf{q}))_{ik}\bar{\ddot{q}}_k.$$

This leads to the component-wise expression of E:

$$E_{ij} = \frac{\partial(\dot{J}(\mathbf{q}, \bar{\dot{\mathbf{q}}})\bar{\dot{\mathbf{q}}})_i}{\partial q_j} + \frac{\partial(J(\mathbf{q})\bar{\ddot{\mathbf{q}}})_i}{\partial q_j},$$
$$E_{ij} = \sum_{k=0}^{n} \frac{\partial(\dot{J}(\mathbf{q}, \bar{\dot{\mathbf{q}}}))_{ik}}{\partial q_j}\bar{\dot{q}}_k + \sum_{k=0}^{n} \frac{\partial(J(\mathbf{q}))_{ik}}{\partial q_j}\bar{\ddot{q}}_k.$$

Appendix B

Application of the UCM extension to the derivative of the centroidal momenta task functions

The similarity between Eqs. (4.7) and (4.16) provides a direct case of application of our extension of the UCM theory. To this end, we compute the partial derivatives of $\dot{\boldsymbol{h}}_G(\boldsymbol{q}, \dot{\boldsymbol{q}}, \ddot{\boldsymbol{q}})$ around the mean performance of one participant ($\bar{\boldsymbol{q}}$, $\bar{\dot{\boldsymbol{q}}}$, $\bar{\ddot{\boldsymbol{q}}}$):

$$\left.\frac{\partial \dot{\boldsymbol{h}}_G}{\partial \ddot{\boldsymbol{q}}}\right|_{\substack{\boldsymbol{q}=\bar{\boldsymbol{q}} \\ \dot{\boldsymbol{q}}=\bar{\dot{\boldsymbol{q}}}}} = A_G(\dot{\boldsymbol{q}}), \tag{B.1a}$$

$$\left.\frac{\partial \dot{\boldsymbol{h}}_G}{\partial \dot{\boldsymbol{q}}}\right|_{\substack{\boldsymbol{q}=\bar{\boldsymbol{q}} \\ \ddot{\boldsymbol{q}}=\bar{\ddot{\boldsymbol{q}}}}} = \frac{\partial(\dot{A}_G(\bar{\boldsymbol{q}}, \dot{\boldsymbol{q}})\dot{\boldsymbol{q}})}{\partial \dot{\boldsymbol{q}}}, \tag{B.1b}$$

$$\left.\frac{\partial \dot{\boldsymbol{h}}_G}{\partial \boldsymbol{q}}\right|_{\substack{\dot{\boldsymbol{q}}=\bar{\dot{\boldsymbol{q}}} \\ \ddot{\boldsymbol{q}}=\bar{\ddot{\boldsymbol{q}}}}} = \frac{\partial(\dot{A}_G(\boldsymbol{q}, \bar{\dot{\boldsymbol{q}}})\bar{\dot{\boldsymbol{q}}})}{\partial \boldsymbol{q}} + \frac{\partial(A_G(\boldsymbol{q})\bar{\ddot{\boldsymbol{q}}})}{\partial \boldsymbol{q}}. \tag{B.1c}$$

Then the presented framework is applied to the first order Taylor expansion of $\dot{\boldsymbol{h}}_G$.

Bibliography

[Ashby 2002] Blake M. Ashby and Jean H. Heegaard. *Role of arm motion in the standing long jump.* Journal of Biomechanics, vol. 35, no. 12, pages 1631–1637, 2002. (Cited in pages 69 and 74.)

[Ashby 2006] Blake M. Ashby and Scott L. Delp. *Optimal control simulations reveal mechanisms by which arm movement improves standing long jump performance.* Journal of Biomechanics, vol. 39, no. 9, pages 1726–1734, 2006. (Cited in pages 69 and 74.)

[Azéma 2012] Marc Azéma and Florent Rivère. *Animation in Palaeolithic art: a pre-echo of cinema.* Antiquity, vol. 86, no. 332, pages 316–324, 2012. (Cited in pages vii and 4.)

[**Bailly** 2018a] **François Bailly**, Justin Carpentier, Philippe Souères and Bruno Watier. *A mechanical descriptor of human locomotion and an application to multi-contact walking in humanoids.* In 7th IEEE International Conference on Biomedical Robotics and Biomechatronics (BioRob). IEEE, 2018. (Cited in page 41.)

[**Bailly** 2018b] **François Bailly**, Vincent Bels, Bruno Watier and Philippe Souères. *Should robots have a head ?- A rationale based on behavior, automatic control and signal processing-.* In 7th International Conference on Biomimetic and Biohybrid Systems (Living Machines), 2018. (Cited in page 116.)

[**Bailly** 2018c] **François Bailly**, Justin Carpentier, Mehdi Benallegue, Philippe Souères and Bruno Watier. *Recursive estimation of the center of mass position and angular momentum variation of the human body.* Under review in Computer Methods in Biomechanics and Biomedical Engineering, 2018. (Cited in page 85.)

[Bajcsy 1988] Ruzena Bajcsy. *Active perception.* Proceedings of the IEEE, vol. 76, no. 8, pages 966–1005, 1988. (Cited in page 126.)

[Baker 2006] Richard Baker. *Gait analysis methods in rehabilitation.* Journal of neuroengineering and rehabilitation, vol. 3, no. 1, page 4, 2006. (Cited in page 86.)

[Barbeito 1979] Raphael Barbeito and Hiroshi Ono. *Four methods of locating the egocenter: A comparison of their predictive validities and reliabilities.* Behavior Research Methods & Instrumentation, vol. 11, no. 1, pages 31–36, 1979. (Cited in page 124.)

[Bateson 2013] Patrick Bateson and Kevin N Laland. *Tinbergen's four questions: an appreciation and an update.* Trends in ecology & evolution, vol. 28, no. 12, pages 712–718, 2013. (Cited in page 119.)

[Bernstein 1967] N Bernstein. The co-ordination and regulation of movements. Pergamon Press, Oxford [etc.], 1967. (Cited in page 58.)

[Boyer 2008] Frederic Boyer, Mathieu Porez, Alban Leroyer and Michel Visonneau. *Fast dynamics of an eel-like robot—comparisons with Navier–Stokes simulations.* IEEE Transactions on Robotics, vol. 24, no. 6, pages 1274–1288, 2008. (Cited in page 117.)

[Bruijn 2008] Sjoerd M Bruijn, Onno G Meijer, Jaap H Van Dieen, Idsart Kingma and Claudine JC Lamoth. *Coordination of leg swing, thorax rotations, and pelvis rotations during gait: the organisation of total body angular momentum.* Gait & posture, vol. 27, no. 3, pages 455–462, 2008. (Cited in page 86.)

[Budd 2017] Graham E Budd and Sören Jensen. *The origin of the animals and a 'Savannah'hypothesis for early bilaterian evolution.* Biological Reviews, vol. 92, no. 1, pages 446–473, 2017. (Cited in pages 119 and 120.)

[Cappozzo 1996] Aurelio Cappozzo, Fabio Catani, Alberto Leardini, MG Benedetti and Ugo Della Croce. *Position and orientation in space of bones during movement: experimental artefacts.* Clinical biomechanics, vol. 11, no. 2, pages 90–100, 1996. (Cited in page 86.)

[Caron 1997] Olivier Caron, Bernard Faure and Yvon Brenière. *Estimating the centre of gravity of the body on the basis of the centre of pressure in standing posture.* Journal of biomechanics, vol. 30, no. 11, pages 1169–1171, 1997. (Cited in page 86.)

[Caron 2017] Stéphane Caron, Quang-Cuong Pham and Yoshihiko Nakamura. *Zmp support areas for multicontact mobility under frictional constraints.* IEEE Transactions on Robotics, vol. 33, no. 1, pages 67–80, 2017. (Cited in page 42.)

[Carpentier 2016a] Justin Carpentier, Mehdi Benallegue, Nicolas Mansard and Jean-Paul Laumond. *Center-of-mass estimation for a polyarticulated system in contact—A spectral approach.* IEEE Transactions on Robotics, vol. 32, no. 4, pages 810–822, 2016. (Cited in pages 86, 90, 98, and 110.)

[Carpentier 2016b] Justin Carpentier, Steve Tonneau, Maximilien Naveau, Olivier Stasse and Nicolas Mansard. *A versatile and efficient pattern generator for generalized legged locomotion.* In International Conference on Robotics and Automation (ICRA), pages 3555–3561. IEEE, 2016. (Cited in pages 42, 43, 52, 81, 93, 102, and 133.)

[Carpentier 2017a] Justin Carpentier, Rohan Budhiraja and Nicolas Mansard. *Learning feasibility constraints for multi-contact locomotion of legged robots.* In Robotics: Science and System (RSS), 2017. (Cited in page 52.)

[Carpentier 2017b] Justin Carpentier and Nicolas Mansard. *Multi-contact Locomotion of Legged Robots.* Submitted to IEEE Transactions on Robotics (TRO), 2017. (Cited in pages 52 and 53.)

[Carpentier 2017c] Justin Carpentier, Florian Valenza, Nicolas Mansard*et al.* *Pinocchio: fast forward and inverse dynamics for poly-articulated systems.* https://stack-of-tasks.github.io/pinocchio, 2015–2017. (Cited in page 93.)

[Chaumette 2006] François Chaumette and S. Hutchinson. *Visual servo control, Part I: Basic approaches.* IEEE Robotics and Automation Magazine, vol. 13, no. 4, pages 82–90, 2006. (Cited in page 63.)

[Cheng 2008] Kuangyou B. Cheng, Chih Hung Wang, Hui Chuan Chen, Chin Dai Wu and Hung Ta Chiu. *The mechanisms that enable arm motion to enhance vertical jump performance-A simulation study.* Journal of Biomechanics, vol. 41, no. 9, pages 1847–1854, 2008. (Cited in page 69.)

[Cheze 1995] L Cheze, BJ Fregly and J Dimnet. *A solidification procedure to facilitate kinematic analyses based on video system data.* Journal of biomechanics, vol. 28, no. 7, pages 879–884, 1995. (Cited in page 23.)

[Clark 2013] James J Clark and Alan L Yuille. Data fusion for sensory information processing systems, volume 105. Springer Science & Business Media, 2013. (Cited in page 124.)

[Collins 1993] J. J. Collins and C. J. De Luca. *Open-loop and closed-loop control of posture: a random-walk analysis of center-of-pressure trajectories.* Experimental brain research, 1993. (Cited in page 42.)

[Damavandi 2009] Mohsen Damavandi, Nader Farahpour and Paul Allard. *Determination of body segment masses and centers of mass using a force plate method in individuals of different morphology.* Medical engineering & physics, vol. 31, no. 9, pages 1187–1194, 2009. (Cited in page 23.)

[Danna-dos Santos 2007] Alessander Danna-dos Santos, Kajetan Slomka, Vladimir M. Zatsiorsky and Mark L. Latash. *Muscle modes and synergies during voluntary body sway.* Experimental Brain Research, vol. 179, no. 4, pages 533–550, jun 2007. (Cited in page 60.)

[Dapena 1978] Jesús Dapena. *A method to determine the angular momentum of a human body about three orthogonal axes passing through its center of gravity.* Journal of Biomechanics, vol. 11, no. 5, pages 251–256, 1978. (Cited in page 86.)

[De Leva 1996] Paolo De Leva. *Adjustments to Zatsiorsky-Seluyanov's segment inertia parameters.* Journal of biomechanics, vol. 29, no. 9, pages 1223–1230, 1996. (Cited in page 86.)

[De Rosario 2012] Helios De Rosario, Alvaro Page, Antonio Besa, Vicente Mata and Efraim Conejero. *Kinematic description of soft tissue artifacts: quantifying rigid versus deformation components and their relation with bone motion.* Medical & biological engineering & computing, vol. 50, no. 11, pages 1173–1181, 2012. (Cited in page 86.)

[Delp 2007] S. L. Delp, F. C. Anderson, A. S. Arnold, P. Loan, A. Habib, C. T. John, E. Guendelman and D. G. Thelen. *OpenSim: Open-Source Software to Create and Analyze Dynamic Simulations of Movement.* IEEE Transactions on Biomedical Engineering, vol. 54, no. 11, pages 1940–1950, 2007. (Cited in pages 19, 22, and 68.)

[Dimentberg 1968] F. M. Dimentberg. *The screw calculus and its applications in mechanics.* Technical Report, DTIC Document, 1968. (Cited in pages 44 and 89.)

[Domkin 2005] Dmitry Domkin, Jozsef Laczko, Mats Djupsjöbacka, Slobodan Jaric and Mark L. Latash. *Joint angle variability in 3D bimanual pointing: uncontrolled manifold analysis.* Experimental Brain Research, vol. 163, no. 1, pages 44–57, may 2005. (Cited in page 60.)

[Dumas 2007] Raphael Dumas, Laurence Cheze and J-P Verriest. *Adjustments to McConville et al. and Young et al. body segment inertial parameters.* Journal of biomechanics, vol. 40, no. 3, pages 543–553, 2007. (Cited in pages vii, 16, 18, 19, 47, and 96.)

[Ehrig 2006] Rainald M Ehrig, William R Taylor, Georg N Duda and Markus O Heller. *A survey of formal methods for determining the centre of rotation of ball joints.* Journal of biomechanics, vol. 39, no. 15, pages 2798–2809, 2006. (Cited in page 23.)

[Ernst 2002] Marc O Ernst and Martin S Banks. *Humans integrate visual and haptic information in a statistically optimal fashion.* Nature, vol. 415, no. 6870, page 429, 2002. (Cited in page 124.)

[Erwin 2011] Douglas H Erwin, Marc Laflamme, Sarah M Tweedt, Erik A Sperling, Davide Pisani and Kevin J Peterson. *The Cambrian conundrum: early divergence and later ecological success in the early history of animals.* science, vol. 334, no. 6059, pages 1091–1097, 2011. (Cited in pages 119 and 120.)

[Fan 2006] Jing Fan, Jiping He and Stephen I. Helms Tillery. *Control of hand orientation and arm movement during reach and grasp.* Experimental Brain Research, vol. 171, no. 3, pages 283–296, may 2006. (Cited in page 60.)

[Farley 1998] Claire T Farley and Daniel P Ferris. *Biomechanics of Walking and Running: Center of Mass Movements to Muscle Action.* Exercise and sport sciences reviews, vol. 26, no. 1, pages 253–286, 1998. (Cited in page 86.)

[Fernie 1982] G. R. Fernie, C. I. Gryfe, P. J. Holliday and A. Llewellyn. *The relationship of postural sway in standing to the incindence of falls in geriatric subjects.* Age and Ageing, 1982. (Cited in page 42.)

[Gelfand 1998] I M Gelfand and M L Latash. *On the problem of adequate language in motor control.* Motor control, vol. 2, no. 4, pages 306–13, 1998. (Cited in page 58.)

[Gera 2010] G Gera, S Freitas, M Latash, K Monahan, G Schoner and J Scholz. *Motor Abundance Contributes to Resolving Multiple Kinematic Task Constraints.* Motor Control, vol. 14, no. 1, pages 83–115, 2010. (Cited in pages 58 and 59.)

[Gittoes 2012] Marianne Jr Gittoes and Gareth Irwin. *Biomechanical approaches to understanding the potentially injurious demands of gymnastic-style impact landings.* Sports Medicine, Arthroscopy, Rehabilitation, Therapy & Technology, vol. 4, no. 1, page 4, 2012. (Cited in page 75.)

[Goswami 2004] A Goswami and V Kallem. *Rate of change of angular momentum and balance maintenance of biped robots.* In IEEE-RAS Int. Conf. on Robotics and Automation (ICRA), 2004., volume 4, pages 3785–3790, 2004. (Cited in page 50.)

[Hansen 2014] Clint Hansen, Gentiane Venture, Nasser Rezzoug, Philippe Gorce and Brice Isableu. *An individual and dynamic Body Segment Inertial Parameter validation method using ground reaction forces.* Journal of biomechanics, vol. 47, no. 7, pages 1577–1581, 2014. (Cited in page 23.)

[Hara 2006] Mikiko Hara, Akira Shibayama, Daisuke Takeshita and Senshi Fukashiro. *The effect of arm swing on lower extremities in vertical jumping.* Journal of Biomechanics, vol. 39, no. 13, pages 2503–2511, 2006. (Cited in page 69.)

[Harada 2003] K. Harada, S. Kajita, K. Kaneko and H. Hirukawa. *ZMP analysis for arm/leg coordination.* In IEEE/RSJ Int. Conf. on Intelligent Robots and Systems (IROS), Oct 2003. (Cited in page 42.)

[Herr 2008a] H. Herr and M. Popovic. *Angular momentum in human walking.* Journal of experimental biology, 2008. (Cited in page 50.)

[Herr 2008b] Hugh Herr and Marko Popovic. *Angular momentum in human walking.* Journal of Experimental Biology, vol. 211, no. 4, pages 467–481, 2008. (Cited in page 86.)

[Hickox 2016] Lauren J. Hickox, Blake M. Ashby and Gordon J. Alderink. *Exploration of the validity of the two-dimensional sagittal plane assumption in modeling the standing long jump.* Journal of Biomechanics, vol. 49, no. 7, pages 1085–1093, 2016. (Cited in page 67.)

[Higgins 1975] Walter T Higgins. *A comparison of complementary and Kalman filtering.* IEEE Transactions on Aerospace and Electronic Systems, pages 321–325, 1975. (Cited in page 90.)

[Hillis 2002] James M Hillis, Marc O Ernst, Martin S Banks and Michael S Landy. *Combining sensory information: mandatory fusion within, but not between, senses.* Science, vol. 298, no. 5598, pages 1627–1630, 2002. (Cited in page 124.)

[Hirose 2001] R Hirose and T. Takenaka. *Development of the Humanoid Robot ASIMO.* Technical Review, no. 1, pages 1–6, 2001. (Cited in page 28.)

[Hirukawa 2006] H. Hirukawa, H. Shizuko, K. Harada, S. Kajita, K. Kaneko, F. Kanehiro, K. Fujiwara and M. Morisawa. *A Universal Stability Criterion of the Foot Contact of Legged Robots - Adios ZMP.* In IEEE-RAS Int. Conf. on Robotics and Automation (ICRA), 2006. (Cited in pages 42 and 52.)

[Hsu 2007] W.-L. Hsu, J. P. Scholz, G. Schoner, J. J. Jeka and T. Kiemel. *Control and Estimation of Posture During Quiet Stance Depends on Multijoint Coordination.* Journal of Neurophysiology, vol. 97, no. 4, pages 3024–3035, jan 2007. (Cited in page 60.)

[Ijspeert 2007] Auke Jan Ijspeert, Alessandro Crespi, Dimitri Ryczko and Jean-Marie Cabelguen. *From swimming to walking with a salamander robot driven by a spinal cord model.* science, vol. 315, no. 5817, pages 1416–1420, 2007. (Cited in page 117.)

[Kajita 2014] S. Kajita, H. Hirukawa, K. Harada and K. Yokoi. Introduction to humanoid robotics. Springer Tracts in Advanced Robotics. Springer Berlin Heidelberg, 2014. (Cited in pages 42, 43, and 50.)

[Khatib 1987] O. Khatib. *A unified approach for motion and force control of robot manipulators: The operational space formulation.* IEEE Journal on Robotics and Automation, vol. 3, no. 1, pages 43–53, 1987. (Cited in page 60.)

[Kobilarov 2015] M. Kobilarov, Duy-Nguyen Ta and F. Dellaert. *Differential dynamic programming for optimal estimation.* In 2015 IEEE International Conference on Robotics and Automation (ICRA), pages 863–869, May 2015. (Cited in pages 102 and 108.)

[Kristianslund 2012] Eirik Kristianslund, Tron Krosshaug and Antonie J. Van den Bogert. *Effect of low pass filtering on joint moments from inverse dynamics: Implications for injury prevention.* Journal of Biomechanics, vol. 45, no. 4, pages 666–671, 2012. (Cited in page 68.)

[Lafond 2004] D Lafond, M Duarte and F Prince. *Comparison of three methods to estimate the center of mass during balance assessment.* Journal of biomechanics, vol. 37, no. 9, pages 1421–1426, 2004. (Cited in page 86.)

[Lamont 2007] E. V. Lamont and E. P. Zehr. *Earth-referenced handrail contact facilitates interlimb cutaneous reflexes during locomotion.* Journal of neurophysiology, 2007. (Cited in page 47.)

[Latash 2001] Mark Latash, John Scholz, Frederic Danion and Gregor Schöner. *Structure of motor variability in marginally redundant multifinger force production tasks.* Experimental Brain Research, vol. 141, no. 2, pages 153–165, nov 2001. (Cited in page 60.)

[Latash 2008] Mark L. Latash, Stacey Gorniak and Vladimir M. Zatsiorsky. *Hierarchies of Synergies in Human Movements.* Kinesiology, vol. 40, no. 1, pages 29–38, 2008. (Cited in page 59.)

[Laumond 2017] Jean-Paul Laumond, Mehdi Benallegue, Justin Carpentier and Alain Berthoz. *The yoyo-man.* The International Journal of Robotics Research, vol. 36, no. 13-14, pages 1508–1520, 2017. (Cited in page 126.)

[Legreneur 2012] Pierre Legreneur, Michel Laurin and Vincent Bels. *Predator–prey interactions paradigm: a new tool for artificial intelligence.* Adaptive Behavior, vol. 20, no. 1, pages 3–9, 2012. (Cited in page 119.)

[Leineweber 2003] Daniel Leineweber, Irene Bauer, Hans Georg Bock and Johannes P Schlöder. *An efficient multiple shooting based reduced SQP strategy for large-scale dynamic process optimization. Part 1: theoretical aspects.* Computers & Chemical Engineering, 2003. (Cited in page 53.)

[Levin 1996] Oron Levin and Joseph Mizrahi. *An iterative model for estimation of the trajectory of center of gravity from bilateral reactive force measurements in standing sway.* Gait & Posture, vol. 4, no. 2, pages 89–99, 1996. (Cited in pages 86 and 98.)

[Lorenz 2013] Konrad Lorenz. The foundations of ethology. Springer Science & Business Media, 2013. (Cited in page 119.)

[Lu 1999] T.-W. Lu and J.J. O'Connor. *Bone position estimation from skin marker co-ordinates using global optimisation with joint constraints.* Journal of Biomechanics, vol. 32, no. 2, pages 129 – 134, 1999. (Cited in page 68.)

[Maldonado 2015] G. Maldonado, H. Bitard, B. Watier and P. Souères. *Evidence of dynamic postural control performance in parkour landing.* Computer Methods in Biomechanics and Biomedical Engineering, vol. 18, no. 1, pages 1994–1995, 2015. (Cited in page 70.)

[Maldonado 2017] Galo Maldonado, **François Bailly**, Philippe Souères and Bruno Watier. *Angular momentum regulation strategies for highly dynamic landing in Parkour.* Computer methods in biomechanics and biomedical engineering, vol. 20, no. sup1, pages 123–124, 2017. (Cited in pages 70, 75, and 98.)

[Maldonado 2018a] Galo Maldonado, **François Bailly** Bailly, Philippe Souères and Bruno Watier. *On the coordination of highly dynamic human movements: an extension of the Uncontrolled Manifold approach applied to precision jump in parkour.* Scientific reports, vol. 8, no. 1, page 12219, 2018. (Cited in pages viii, ix, 61, 66, 67, 71, and 72.)

[Maldonado 2018b] Galo Maldonado, **François Bailly**, Philippe Souères and Bruno Watier. *An interdisciplinary method based on performance variables to generate and analyze dynamic human motions.* In 8th World Congress of Biomechanics, Dublin, Ireland, 2018. (Not cited.)

[Maldonado 2018c] Galo Maldonado, **François Bailly**, Philippe Souères and Bruno Watier. *Identifying priority tasks during sport motions.* In 8th World Congress of Biomechanics, Dublin, Ireland, 2018. (Not cited.)

[Mansard 2009] Nicolas Mansard, Olivier Stasse, Paul Evrard and Abderrahmane Kheddar. *A versatile generalized inverted kinematics implementation for collaborative working humanoid robots: the Stack of Tasks.* In ICAR'09: International Conference on Advanced Robotics, pages 1–6, Munich, Germany, June 2009. (Cited in page 63.)

[Manzanares 2000] Miguel Manzanares, Hiroshi Wada, Nobue Itasaki, Paul A Trainor, Robb Krumlauf and Peter WH Holland. *Conservation and elaboration of Hox gene regulation during evolution of the vertebrate head.* Nature, vol. 408, no. 6814, page 854, 2000. (Cited in page 117.)

[McConville 1976] John T McConville and Charles E Clauser. *Anthropometric assessment of the mass distribution characteristics of the living human body.* In Proceedings of the Human Factors Society Annual Meeting, volume 20, pages 379–383. Sage Publications Sage CA: Los Angeles, CA, 1976. (Cited in page 18.)

[McConville 1980] John T McConville, Charles E Clauser, Thomas D Churchill, Jaime Cuzzi and Ints Kaleps. *Anthropometric relationships of body and body segment moments of inertia.* Technical Report, ANTHROPOLOGY RESEARCH PROJECT INC YELLOW SPRINGS OH, 1980. (Cited in pages vii, xi, 16, and 17.)

[McGurk 1976] Harry McGurk and John MacDonald. *Hearing lips and seeing voices.* Nature, vol. 264, no. 5588, page 746, 1976. (Cited in page 124.)

[Menon 2004] Carlo Menon, Michael Murphy and Metin Sitti. *Gecko inspired surface climbing robots.* In IEEE International Conference on Robotics and Biomimetics, pages 431–436. IEEE, 2004. (Cited in page 117.)

[Minetti 2011] Alberto E Minetti, Caterina Cisotti and Omar S Mian. *The mathematical description of the body centre of mass 3D path in human and*

animal locomotion. Journal of biomechanics, vol. 44, no. 8, pages 1471–1477, 2011. (Cited in page 98.)

[Monnet 2007] Tony Monnet, Eric Desailly, Mickaël Begon, Claude Vallée and Patrick Lacouture. *Comparison of the SCoRE and HA methods for locating in vivo the glenohumeral joint centre.* Journal of biomechanics, vol. 40, no. 15, pages 3487–3492, 2007. (Cited in page 23.)

[Monnet 2012] Tony Monnet, Arsène Thouzé, Matt TG Pain and Mickaël Begon. *Assessment of reproducibility of thigh marker ranking during walking and landing tasks.* Medical engineering & physics, vol. 34, no. 8, pages 1200–1208, 2012. (Cited in page 23.)

[Morasso 1999] Pietro G Morasso, Gino Spada and Roberto Capra. *Computing the COM from the COP in postural sway movements.* Human Movement Science, vol. 18, no. 6, pages 759–767, 1999. (Cited in pages 86 and 98.)

[Nakamura 1991] Yoshihiko. Nakamura and Yoshihiko. Advanced robotics : redundancy and optimization. Addison-Wesley Pub. Co, 1991. (Cited in page 32.)

[Naveau 2017] Maximilien Naveau, Manuel Kudruss, Olivier Stasse, Christian Kirches, Katja Mombaur and Philippe Souères. *A reactive walking pattern generator based on nonlinear model predictive control.* IEEE Robotics and Automation Letters, vol. 2, no. 1, pages 10–17, 2017. (Cited in page 117.)

[Neelon 2004] Michael F Neelon, Douglas S Brungart and Brian D Simpson. *The isoazimuthal perception of sounds across distance: A preliminary investigation into the location of the audio egocenter.* Journal of Neuroscience, vol. 24, no. 35, pages 7640–7647, 2004. (Cited in page 124.)

[Nisky 2014] Ilana Nisky, Michael H. Hsieh and Allison M. Okamura. *Uncontrolled Manifold Analysis of Arm Joint Angle Variability During Robotic Teleoperation and Freehand Movement of Surgeons and Novices.* IEEE Transactions on Biomedical Engineering, vol. 61, no. 12, pages 2869–2881, 2014. (Cited in page 62.)

[Orin 2013] David E. Orin, Ambarish Goswami and Sung-Hee Lee. *Centroidal dynamics of a humanoid robot.* Autonomous Robots, vol. 35, no. 2-3, pages 161–176, 2013. (Cited in pages 4, 52, 65, 81, 98, and 102.)

[Park 2017] Hae-Won Park, Patrick M Wensing and Sangbae Kim. *High-speed bounding with the MIT Cheetah 2: Control design and experiments.* The International Journal of Robotics Research, vol. 36, no. 2, pages 167–192, 2017. (Cited in page 28.)

[Pecoits 2012] Ernesto Pecoits, Kurt O Konhauser, Natalie R Aubet, Larry M Heaman, Gerardo Veroslavsky, Richard A Stern and Murray K Gingras.

Bilaterian burrows and grazing behavior at> 585 million years ago. Science, vol. 336, no. 6089, pages 1693–1696, 2012. (Cited in page 120.)

[Peters 2010] A. Peters, B. Galna, M. Sangeux, M. Morris and R. Baker. *Quantification of soft tissue artifact in lower limb human motion analysis: a systematic review.* Gait & posture, 2010. (Cited in pages 16 and 23.)

[Pettorossi 2014] Vito Enrico Pettorossi and Marco Schieppati. *Neck proprioception shapes body orientation and perception of motion.* Frontiers in human neuroscience, vol. 8, page 895, 2014. (Cited in page 126.)

[Poincaré 1905] Henri Poincaré. *Space and Geometry.* In Science and hypothesis, chapter 4. Science Press, 1905. (Cited in page 115.)

[Popovic 2004] M. Popovic, A. Hofmann and H. Herr. *Angular momentum regulation during human walking: biomechanics and control.* In IEEE-RAS Int. Conf. on Robotics and Automation (ICRA), 2004. (Cited in page 50.)

[Pozzo 1990] Th Pozzo, A Berthoz and L Lefort. *Head stabilization during various locomotor tasks in humans.* Experimental brain research, vol. 82, no. 1, pages 97–106, 1990. (Cited in page 126.)

[Prieto 1996] T. E. Prieto, J. B. Myklebust, R. G. Hoffmann, E. G. Lovett and B. M. Myklebust. *Measures of postural steadiness: differences between healthy young and elderly adults.* IEEE Transactions on biomedical engineering, 1996. (Cited in page 42.)

[Rao 2006] Guillaume Rao, David Amarantini, Eric Berton and Daniel Favier. *Influence of body segments' parameters estimation models on inverse dynamics solutions during gait.* Journal of biomechanics, vol. 39, no. 8, pages 1531–1536, 2006. (Cited in page 23.)

[Reid 2011] S. M. Reid, A. C. Novak, B. Brouwer and P. A. Costigan. *Relationship between stair ambulation with and without a handrail and centre of pressure velocities during stair ascent and descent.* Gait & posture, 2011. (Cited in page 47.)

[Reisman 2002] Darcy S. Reisman, John P. Scholz and Gregor Schöner. *Coordination underlying the control of whole body momentum during sit-to-stand.* Gait and Posture, vol. 15, no. 1, pages 45–55, 2002. (Cited in pages 60 and 61.)

[Robert 2009] Thomas Robert, Bradford C Bennett, Shawn D Russell, Christopher A Zirker and Mark F Abel. *Angular momentum synergies during walking.* Experimental brain research, vol. 197, no. 2, pages 185–197, 2009. (Cited in pages 50 and 61.)

[Ruffier 2003] Franck Ruffier, Stéphane Viollet, S Amic and N Franceschini. *Bio-inspired optical flow circuits for the visual guidance of micro air vehicles.* In Proceedings of the International Symposium on Circuits and Systems, volume 3. IEEE, 2003. (Cited in page 117.)

[Saab 2011] L. Saab, N. Mansard, F. Keith, J. Y. Fourquet and P. Soueres. *Generation of dynamic motion for anthropomorphic systems under prioritized equality and inequality constraints.* In 2011 IEEE International Conference on Robotics and Automation, pages 1091–1096, 2011. (Cited in pages 34 and 63.)

[Saab 2013a] Layale Saab, Oscar E Ramos, François Keith, Nicolas Mansard, Philippe Soueres and Jean-Yves Fourquet. *Dynamic whole-body motion generation under rigid contacts and other unilateral constraints.* IEEE Transactions on Robotics, vol. 29, no. 2, pages 346–362, 2013. (Cited in page 31.)

[Saab 2013b] Layale Saab, Oscar E Ramos, François Keith, Nicolas Mansard, Philippe Soueres and Jean-Yves Fourquet. *Dynamic whole-body motion generation under rigid contacts and other unilateral constraints.* Transactions on Robotics (TRO), 2013. (Cited in page 52.)

[Samson 1991] Claude Samson, Bernard Espiau and Michel Le Borgne. Robot control: the task function approach. Oxford University Press, 1991. (Cited in page 32.)

[Sardain 2004] P. Sardain and G. Bessonnet. *Forces Acting on a Biped Robot. Center of Pressure-zero Moment Point.* Trans. Sys. Man Cyber. Part A, 2004. (Cited in page 42.)

[Schleidt 1974] Wolfgang M Schleidt. *How "fixed" is the fixed action pattern?* Ethology, vol. 36, no. 1-5, pages 184–211, 1974. (Cited in page 119.)

[Scholz 1999] John P. Scholz and Gregor Schöner. *The uncontrolled manifold concept: Identifying control variables for a functional task.* Experimental Brain Research, vol. 126, no. 3, pages 289–306, 1999. (Cited in pages 59, 61, and 62.)

[Scholz 2001] John Scholz, Darcy Reisman and Gregor Schöner. *Effects of varying task constraints on solutions to joint coordination in a sit-to-stand task.* Experimental Brain Research, vol. 141, no. 4, pages 485–500, dec 2001. (Cited in page 60.)

[Seth 2010] Ajay Seth, Michael Sherman, Peter Eastman and Scott Delp. *Minimal formulation of joint motion for biomechanisms.* Nonlinear Dynamics, vol. 62, no. 1, pages 291–303, Oct 2010. (Cited in page 68.)

[Shannon 1949] Claude Elwood Shannon. *Communication in the presence of noise.* Proceedings of the IRE, vol. 37, no. 1, pages 10–21, 1949. (Cited in page 125.)

[Shimba 1984a] T. Shimba. *An estimation of center of gravity from force platform data.* Journal of biomechanics, 1984. (Cited in page 44.)

[Shimba 1984b] Takeshi Shimba. *An estimation of center of gravity from force platform data.* Journal of Biomechanics, vol. 17, no. 1, pages 5359–5760, 1984. (Cited in page 86.)

[Sira-Ramirez 2004] Hebertt Sira-Ramirez and Sunil K Agrawal. Differentially flat systems. Crc Press, 2004. (Cited in page 126.)

[Standing 2015] Regan J Standing and Peter S Maulder. *A Comparison of the Habitual Landing Strategies from Differing Drop Heights of Parkour Practitioners (Traceurs) and Recreationally Trained Individuals.* Journal of Sports Science and Medicine, vol. 14, no. 4, pages 723–731, 2015. (Cited in pages 66, 70, and 75.)

[Sukemiya 2008] Haru Sukemiya, Sachio Nakamizo and Hiroshi Ono. *Location of the auditory egocentre in the blind and normally sighted.* Perception, vol. 37, no. 10, pages 1587–1595, 2008. (Cited in page 124.)

[Tassa 2014] Yuval Tassa, Nicolas Mansard and Emo Todorov. *Control-limited differential dynamic programming.* In Robotics and Automation (ICRA), 2014 IEEE International Conference on, pages 1168–1175. IEEE, 2014. (Cited in page 101.)

[Tinbergen 1963] Niko Tinbergen. *On aims and methods of ethology.* Ethology, vol. 20, no. 4, pages 410–433, 1963. (Cited in page 119.)

[Todorov 2005] Emanuel Todorov, Weiwei Li and Xiuchuan Pan. *From task parameters to motor synergies: A hierarchical framework for approximately-optimal control of redundant manipulators.* Journal of robotic systems, vol. 22, no. 11, pages 691–710, nov 2005. (Cited in pages 58 and 59.)

[Tseng 2006] Ya-weng Tseng, John P Scholz and Martin Valere. *Effects of movement frequency and joint kinetics on the joint coordination underlying bimanual circle drawing.* Journal of motor behavior, vol. 38, no. 5, pages 383–404, sep 2006. (Cited in page 60.)

[Wakai 2005] Masaki Wakai and Nicholas P. Linthorne. *Optimum take-off angle in the standing long jump.* Human Movement Science, vol. 24, no. 1, pages 81–96, 2005. (Cited in page 74.)

[Weber 1836] Wilhelm Weber and Eduard F Weber. Mechanik der menschlichen gehwerkzeuge: eine anatomisch-physiologische untersuchung, volume 1. Dietrich, 1836. (Cited in page 20.)

[Whittle 2007] Michael Whittle. *Gait analysis an introduction.* Oxford Orthopaedic Engineering Center, ELSEVIER, 2007. (Cited in pages vii and 15.)

[Wieber 2006] P-B Wieber. *Holonomy and nonholonomy in the dynamics of articulated motion.* In Fast motions in biomechanics and robotics, pages 411–425. Springer, 2006. (Cited in page 42.)

[Wieber 2008] Pierre-Brice Wieber. *Viability and predictive control for safe locomotion.* In IEEE/RSJ Int. Conf. on Intelligent Robots and Systems (IROS), 2008. (Cited in page 53.)

[Wilson 1995] VJ Wilson, R Boyle, K Fukushima, PK Rose, Y Shinoda, Y Sugiuchi and Y Uchino. *The vestibulocollic reflex.* Journal of vestibular research: equilibrium & orientation, vol. 5, no. 3, pages 147–170, 1995. (Cited in page 126.)

[Winter 2009] David A Winter. Biomechanics and motor control of human movement, Fourth Edition. John Wiley & Sons, Inc, 2009. (Cited in pages 19 and 68.)

[Wu 2002a] G Wu, S. Siegler, P. Allard, C. Kirtley, A. Leardini, D. Rosenbaum, M. Whittle, D. D. D'Lima, L. Cristofolini, H. Witte*et al.* *ISB recommendation on definitions of joint coordinate system of various joints for the reporting of human joint motion—part I: ankle, hip, and spine.* Journal of biomechanics, 2002. (Cited in page 16.)

[Wu 2002b] Ge Wu, Sorin Siegler, Paul Allard, Chris Kirtley, Alberto Leardini, Dieter Rosenbaum, Mike Whittle, Darryl D D'Lima, Luca Cristofolini, Hartmut Witte, Oskar Schmid and Ian Stokes. *ISB recommendation on definitions of joint coordinate system of various joints for the reporting of human joint motion—Part I: ankle, hip, and spine.* Journal of Biomechanics, vol. 35, no. 4, pages 543–548, 2002. (Cited in page 96.)

[Wu 2005a] Ge Wu, Frans C.T. van der Helm, H.E.J. (DirkJan) Veeger, Mohsen Makhsous, Peter Van Roy, Carolyn Anglin, Jochem Nagels, Andrew R. Karduna, Kevin McQuade, Xuguang Wang, Frederick W. Werner and Bryan Buchholz. *ISB recommendation on definitions of joint coordinate systems of various joints for the reporting of human joint motion—Part II: shoulder, elbow, wrist and hand.* Journal of Biomechanics, vol. 38, no. 5, pages 981–992, 2005. (Cited in page 96.)

[Wu 2005b] Ge Wu, Frans CT Van der Helm, HEJ DirkJan Veeger, Mohsen Makhsous, Peter Van Roy, Carolyn Anglin, Jochem Nagels, Andrew R Karduna, Kevin McQuade, Xuguang Wang*et al.* *ISB recommendation on definitions of joint coordinate systems of various joints for the reporting of human joint motion—Part II: shoulder, elbow, wrist and hand.* Journal of biomechanics, no. 5, pages 981–992, 2005. (Cited in pages 16 and 47.)

[Yeadon 2010] M.R. Yeadon, M.A. King, S.E. Forrester, G.E. Caldwell and M.T.G. Pain. *The need for muscle co-contraction prior to a landing.* Journal of Biomechanics, vol. 43, no. 2, pages 364–369, 2010. (Cited in page 75.)

[Yen 2009] Jasper T Yen, Arick G Auyang and Young-Hui Chang. *Joint-level kinetic redundancy is exploited to control limb-level forces during human hopping.* Experimental brain research, vol. 196, no. 3, pages 439–451, 2009. (Cited in pages 50 and 60.)

[Young 1983] Joseph W Young, Richard F Chandler, Clyde C Snow, Kathleen M Robinette, Gregory F Zehner and Maureen S Lofberg. *Anthropometric and mass distribution characteristics of the adult female.* Technical Report, 1983. (Cited in pages vii, 16, and 18.)

[Yun 2011] S Yun and A Goswami. *Momentum-based reactive stepping controller on level and non-level ground for humanoid robot push recovery.* In IEEE/RSJ Int. Conf. on Intelligent Robots and Systems (IROS), 2011., pages 3943–3950, 2011. (Cited in page 50.)

[Zhang 2004] Qilong Zhang and Robert Pless. *Extrinsic calibration of a camera and laser range finder (improves camera calibration).* In IEEE/RSJ International Conference on Intelligent Robots and Systems, volume 3, pages 2301–2306. IEEE, 2004. (Cited in page 125.)